

Quantum Optics and Photonics

Academic and Research Staff

Prof. Shaoul Ezekiel, Dr. Selim M. Shahriar, Dr. V. S. Sudarshanam, Dr. Alexey Turukhin, Dr. Parminder Bhatia, Dr. Venkatesh Gopal, Dr. DeQui Qing, Dr. R. Tripathi.

Visiting Scientist and Research Affiliates

Prof. Jeffrey Shapiro, Prof. Seth Lloyd, Prof. Cardinal Warde, Prof. Marc Cronin-Golomb, Dr. Philip Hemmer, Dr. John Donoghue, John Kierstead, Dr. P. Pradhan.

Graduate Students

Ying Tan, Jacob Morzinski, Moninder Jheeta, Ward Weathers

Undergraduate Students

Shome Basu, Edward Flagg, Kathryn Washburn

Website: <http://qop.mit.edu/>

1. Single-Zone Atom Interferometer : Experimental Observation

In a typical atomic interferometer, the atomic wavepacket is split first by what can be considered effectively as an atomic beamsplitter. The split components are then redirected towards each other by atomic mirrors. Finally, the converging components are recombined by another atomic beam splitter. Here, we demonstrate a novel atomic interferometer where the atomic split is split and recombined in a continuous manner. Specifically, in this interferometer, the atom simply passes through a *single-zone* optical beam, consisting of a pair of bichromatic counter-propagating beams that cause optically off-resonant Raman excitations. During the passage, the atomic wave packets in two distinct internal states couple to each other *continuously*. The two internal states trace out a complicated trajectory, guided by the optical beams, with the amplitude and spread of each wavepacket varying continuously. Yet, at the end of the single-zone excitation, there is an interference with fringe amplitudes that can reach a visibility close to unity. One can consider this experiment as a limiting version of $\pi/2$ - π - $\pi/2$ Raman atom interferometer, proposed originally by Borde, and demonstrated by Chu et al. Specifically, the distances between the first $\pi/2$ Raman pulse and the π Raman pulse and between the π Raman pulse and the second $\pi/2$ Raman pulse are zero. This configuration is considerably simpler than the Borde-Chu interferometer (BCI), eliminating the need for precise alignment of the multiple zones. In situations of practical interest, the BCI and the continuous interferometer (CI) can achieve comparable performance (e.g., rotational sensitivity). As such, the relative simplicity of the CI may make it an attractive candidate for measuring rotation. Furthermore, it opens up the possibility of realizing trajectories with multiplier loops in a manner that is able to measure other effects while the rotational sensitivity vanishes.

Basic Theory

We will consider a Λ system. See Figure 1. The Hamiltonian for this system is

$$H = \hbar \omega_e |e\rangle\langle e| + \hbar \omega_b |b\rangle\langle b| + \hbar \omega_a |a\rangle\langle a| - \mathbf{d} \cdot \mathbf{E}$$

where \mathbf{d} is the dipole moment of the atom and \mathbf{E} is the laser field,

$$\mathbf{d} = \mathbf{d}_{ea} + \mathbf{d}_{eb},$$

$$\mathbf{E} = \mathbf{E}_a \cos(\omega_1 t + \phi_1) + \mathbf{E}_b \cos(\omega_2 t + \phi_2).$$

In matrix form, this can be expressed as:

$$H = \hbar \begin{bmatrix} \omega_e & -\Omega_a \cos(\omega_1 t + \phi_1) & -\Omega_b \cos(\omega_2 t + \phi_2) \\ -\Omega_a^* \cos(\omega_1 t + \phi_1) & \omega_a & 0 \\ -\Omega_b^* \cos(\omega_2 t + \phi_2) & 0 & \omega_b \end{bmatrix}$$

where

$$\Omega_a = \langle e | \mathbf{d}_{ea} \cdot \mathbf{E}_a | a \rangle / \hbar$$

$$\Omega_b = \langle e | \mathbf{d}_{eb} \cdot \mathbf{E}_b | b \rangle / \hbar.$$

For off-resonant Raman interaction, if far-detuned, which is the case in our experiment, the excited states are almost not involved so the three-level system can be simplified to a two-level system. After rotating wave approximation, changing the basis to the slow-varying basis, after rotating wave transformation and shift the energy zero point, we get

$$H_R = \frac{\hbar}{2} \begin{bmatrix} 2\delta & -\Omega_a & -\Omega_b \\ -\Omega_a^* & \Delta & 0 \\ -\Omega_b^* & 0 & -\Delta \end{bmatrix}$$

In matrix form,

$$|\Psi\rangle = \begin{bmatrix} C_e(t) \\ C_a(t) \\ C_b(t) \end{bmatrix},$$

$$i\hbar \frac{\partial}{\partial t} |\Psi\rangle = H_R |\Psi\rangle,$$

$$\begin{bmatrix} \dot{C}_e(t) \\ \dot{C}_a(t) \\ \dot{C}_b(t) \end{bmatrix} = -i \begin{bmatrix} 2\delta & -\Omega_a & -\Omega_b \\ -\Omega_a^* & \Delta & 0 \\ -\Omega_b^* & 0 & -\Delta \end{bmatrix} \begin{bmatrix} C_e(t) \\ C_a(t) \\ C_b(t) \end{bmatrix}.$$

We get

$$\begin{cases} \dot{C}_e(t) = -i2\delta C_e(t) + i\Omega_a C_a(t) + i\Omega_b C_b(t) \\ \dot{C}_a(t) = i\Omega_a^* C_e(t) - i\Delta C_a(t) \\ \dot{C}_b(t) = i\Omega_b^* C_e(t) + i\Delta C_b(t) \end{cases}$$

Since it's far-detuned, we could adiabatically eliminate the excited state that is the excited-state population is very small, so that we can ignore the change of the ground states population due to the excited state decays,

$$\dot{C}_e(t) = 0,$$

so

$$C_e(t) = \frac{\Omega_a C_a(t) + \Omega_b C_b(t)}{2\delta}$$

Substitute this into the above equation (1), we get

$$\begin{cases} \dot{C}_a(t) = i\left(\frac{|\Omega_a^*|^2}{4\delta} - \frac{\Delta}{2}\right)C_a(t) + i\frac{\Omega_a^* \Omega_b}{4\delta} C_b(t) \\ \dot{C}_b(t) = i\frac{\Omega_a \Omega_b^*}{4\delta} C_a(t) + i\left(\frac{|\Omega_b^*|^2}{4\delta} + \frac{\Delta}{2}\right)C_b(t) \end{cases}$$

$$\begin{bmatrix} \dot{C}_a(t) \\ \dot{C}_b(t) \end{bmatrix} = -i \begin{bmatrix} \frac{\Delta}{2} - \frac{|\Omega_a^*|^2}{4\delta} & -\frac{\Omega_a^* \Omega_b}{4\delta} \\ -\frac{\Omega_a \Omega_b^*}{4\delta} & -\frac{\Delta}{2} - \frac{|\Omega_b^*|^2}{4\delta} \end{bmatrix} \begin{bmatrix} C_a(t) \\ C_b(t) \end{bmatrix}$$

$$i \begin{bmatrix} \dot{C}_a(t) \\ \dot{C}_b(t) \end{bmatrix} = H_R' \begin{bmatrix} C_a(t) \\ C_b(t) \end{bmatrix}$$

This is an effective two-level system where

$$H_R' = \begin{bmatrix} \frac{\Delta}{2} - \frac{|\Omega_a^*|^2}{4\delta} & -\frac{\Omega_a^* \Omega_b}{4\delta} \\ -\frac{\Omega_a \Omega_b^*}{4\delta} & -\frac{\Delta}{2} - \frac{|\Omega_b^*|^2}{4\delta} \end{bmatrix}$$

and

$$\Omega_R = \frac{\Omega_a^* \Omega_b}{2\delta}$$

is the effective Rabi frequency for this two-level system. Numerical simulations show the 2π one zone Raman atom interferometer is equivalent to the $\pi/2$ - π - $\pi/2$ three zone Raman atom interferometer if we choose the condition that the Raman pulse width of the phase scanned part is $r = 1/4$ of the total Raman width in one zone case and the time between Raman pulses set to zero in three zone case. Further numerical simulations show that one zone Raman atom interferometer is very forgiving. If the ratio r is not $1/4$ and the total Raman pulse width is not 2π , the frequency of the state b population flopping is still the same as that of the phase scan. However, the population flopping amplitude would be smaller and also there could be a π phase shift relative to the case when $r = 1/4$ and pulse width equals to 2π . Simulations also show that the

state b population flopping amplitude as a function of r is sinusoidal. With longitudinal velocity averaging, $r=0.5$ always gives the maximum state b population flopping amplitude. The value of this amplitude is related to the total intensity of the Raman beam. Figure 2 shows one of these velocity averaging results. According to the simulation, AC stark shift doesn't play a role so long as the total Raman pulse width is the same.

The state b population amplitude changes as a function of the phase shift of one part of one of the Raman beam is atomic interference. This is a very simple atom interferometer. Using just one set of Raman beams to get atomic interference greatly simplify the Raman beam alignment effort.

Experimental setup and experimental results

Our experimental setup is shown schematically in Figure. 3. In a vacuum system, Rubidium atoms are emitted from an oven and form a thermal beam. Two nozzles are used to collimate the atomic beam. The diameter of each nozzle is about 330 μm and the distance between them is about 112 mm. The interaction region is magnetically shielded by μ metal. Inside this shielded region, there is a Helmholtz coil structure to provide us with magnetic bias field which is along the direction of the Raman beams.

In this experiment, we don't need to do magnetic sublevel optical pumping. We only need four different laser beams for optical beam, detection beam and two Raman beams.

The lasers we use in our experiment are Coherent 899 Ti:sapphire ring lasers pumped by Coherent Innova 400 Argon lasers. The Ti:sapphire laser gives us about 1.8 Watt in single mode operation with the tunability of 20 GHz when pumped by 12 Watt Argon ion laser power. In this experiment, we use Rubidium 85 transitions. The Ti:sapphire laser is locked to Rubidium 85 transition $5P_{3/2}$ ($F=3$) to $5S_{1/2}$ ($F=3$) through a saturation absorption of a Rubidium vapor cell. Part of the laser beam at this frequency is used for optical pumping which would pump Rb atoms to their initial state $5P_{3/2}$ ($F=2$) from $5P_{3/2}$ ($F=3$). Part of the laser beam would go through an acousto-optic modulator (AOM) (Isomet, model 1206C) with center frequency 110 MHz, upshift 120 MHz, which will tune the deflected beam to transition $5P_{3/2}$ ($F=3$) to $5S_{1/2}$ ($F=4$). As this transition is a cyclic transition, we use it as the optical detection beam. By irradiating the atoms with this detection beam, we collect the fluorescence on a photomultiplier tube. The rest of the laser beam will split to two parts by a 50% beam splitter. One part will go through a 1.5 GHz AOM (Brimrose model GPF-1500-300-.795), upshift and another will go through a 1.5 GHz AOM (Brimrose model GPF-1500-300-.795), downshift. Those two 1.5 GHz AOMs are controlled by the same microwave generator (Wavetek 1-4 GHz Micro Sweep model 962). Since the hyperfine splitting of Rubidium 85 ground states is about 3 GHz, both the deflected beams after 1.5 GHz AOM are red detuned by 1.5 GHz, from transitions $5P_{3/2}$ ($F=2$) to $5S_{1/2}$ ($F=3$) and $5P_{3/2}$ ($F=3$) to $5S_{1/2}$ ($F=3$), respectively. See Figure 4 for all the frequency involved.

To scan the phase of one part of one of the Raman beams, we use a galvo glass. The glass plate we had originally was too thick so we use a microscopic object instead. This microscopic object is about 1mm thick. It is attached to the side of the original glass plate by a piece of double side tape. The galvo is mounted on a magnetic base and is driven by a function generator (BK Precision 5 MHz function generator) directly. This is a loading effect.

In our experiment, we scan the laser over transitions $5P_{3/2}$ ($F=3$) to $5S_{1/2}$, first we block all the beams except the detection beam to align and check to make sure that we have a good atomic beam. Then we let through and align the optical pumping beam. Since we detect the atom population is state $5P_{3/2}$ ($F=3$) and optical pumping beam move atoms away from this state, we should see that the fluorescence signal decrease and minimized as the alignment of the optical pumping beam is perfecting when gradually decrease the intensity of this beam. After this we can lock the laser to $5P_{3/2}$ ($F=3$) to $5S_{1/2}$ ($F=3$) and let through the counter-propagating Raman beams.

To detect Raman signal, we scan the difference detuning of the Raman beams by scanning the frequency of the microwave generator. When we get a good counter-propagating Raman signal, we can insert the galvo glass plate in one of the Raman beams. We slow down the Raman difference detuning scan and try to adjust the offset of the difference detuning scan and decrease this scan range to let the Raman signal sits at the peak position. At the same time we scan the galvo glass and carefully adjust the width of the Raman beam that the galvo glass cut through till we see the atomic interference. The galvo glass tilt angle is between 10° and 20° . When galvo glass is completely in the Raman beam or when it's completely out of the Raman beam, we don't observe any atomic interference, as what we expected. When we change the tilt angle of the galvo glass or when we change the scan amplitude, in both cases the phaseshifts covered by one scan change. And we can see that the number of the atomic interference fringes also changes, accordingly. We can use a Mach-Zehnder optical interferometer to calibrate the phase shift caused by the galvo glass scanner by insert this galvo glass plate in one leg of the optical interferometer and scan it. Figure 5 shows the results of the atomic interference fringes and the optical interference fringes. Figure 11 is a blowup plot of Figure 10. The number of fringes per scan, in both the atomic case and the optical case, depends on the optical path length difference induced by the galvo glass plate, which in turn is a function of the galvo glass title angle.

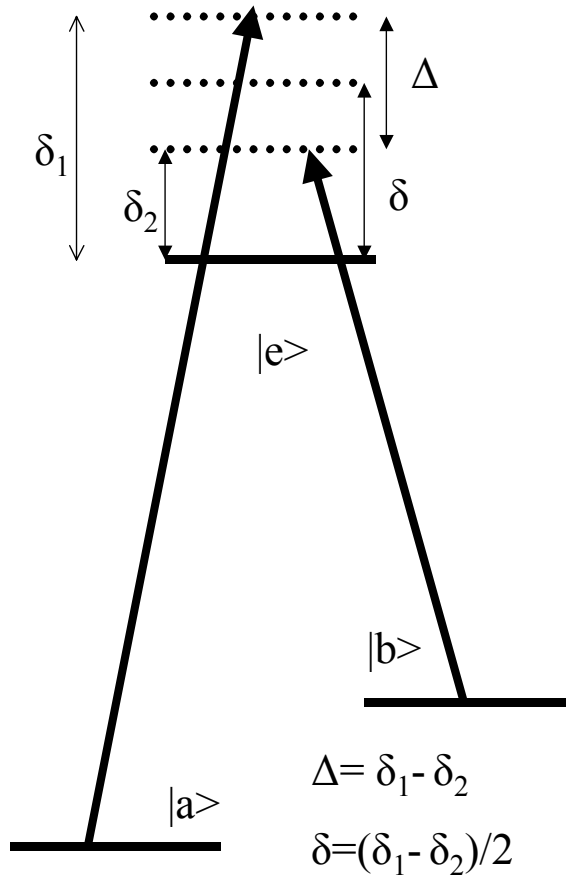


Figure 1. Three level system δ is the common detuning and Δ is the difference detuning.

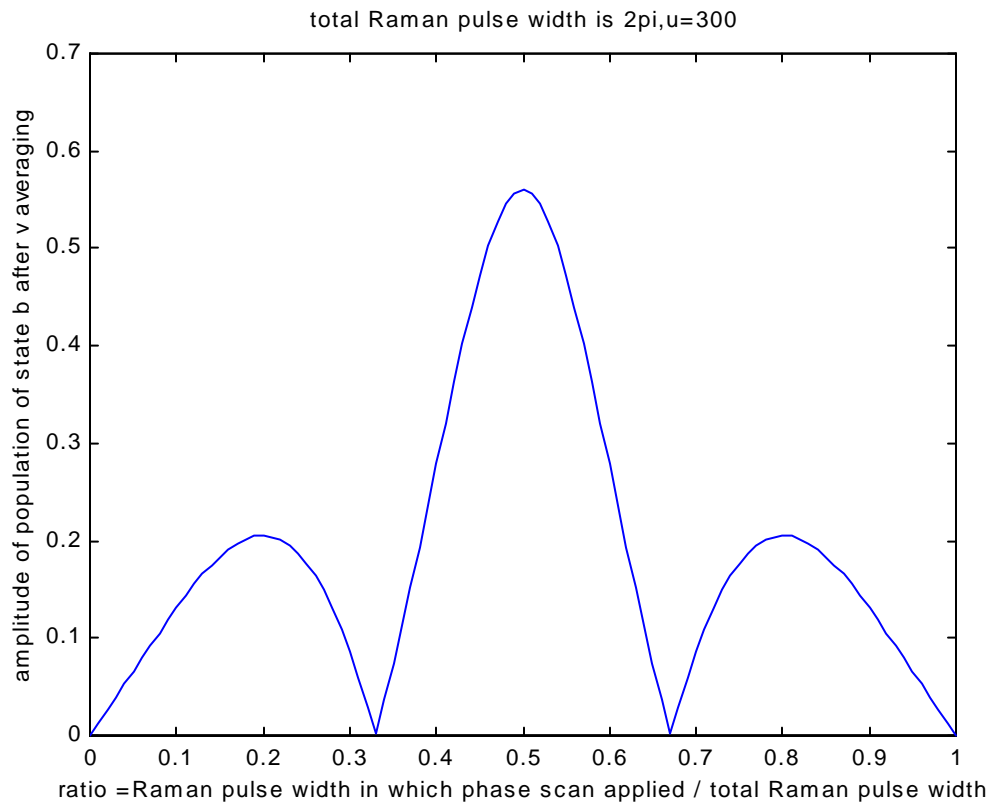


Figure 2. Numerical simulation result of the state b population flopping amplitude as a function of r is sinusoidal, with longitudinal velocity averaging.

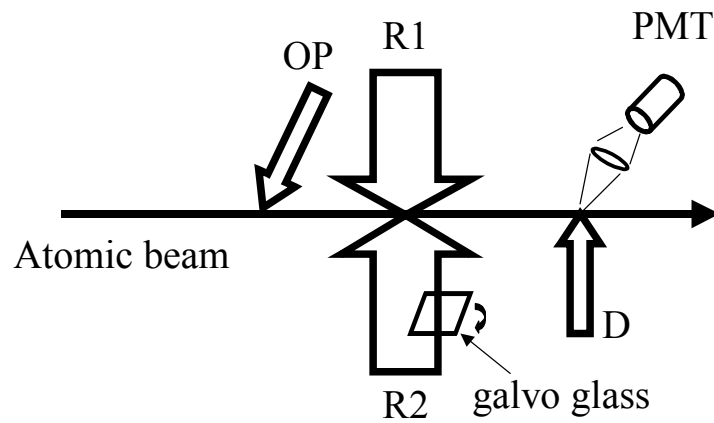


Figure 3 Experimental setup. OP:optical pumping beam, R1:Raman beam 1 connecting level $F=2$ to $F'=3$, R2:Raman beam 2 connecting level $F=3$ to $F'=3$, D: detection beam, PMT: photomultiplier tube.

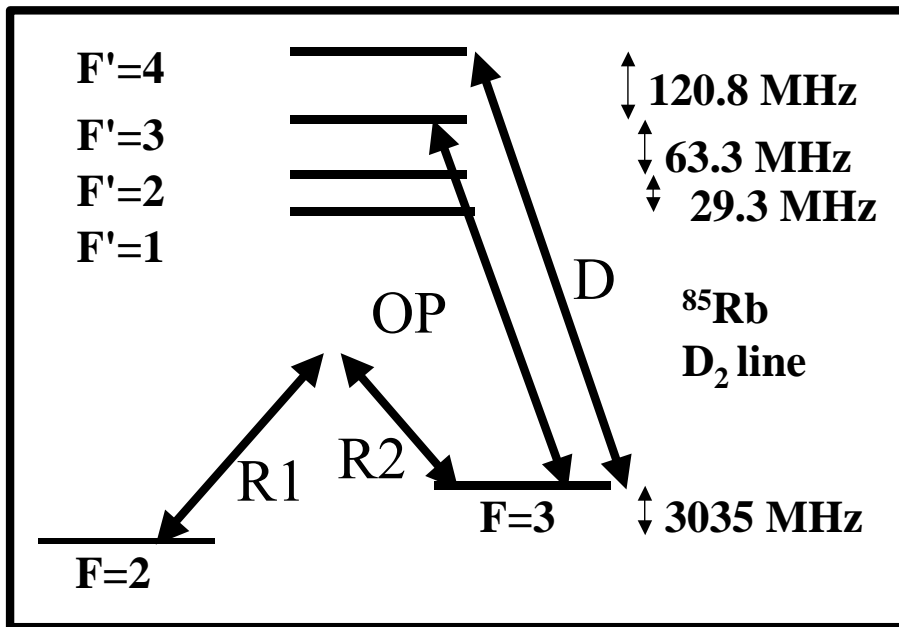


Figure 4 Overall frequency scheme. R1: Raman beam 1, R2: Raman beam 2, D:Detection beam, OP: Optical pumping beam. ^{85}Rb

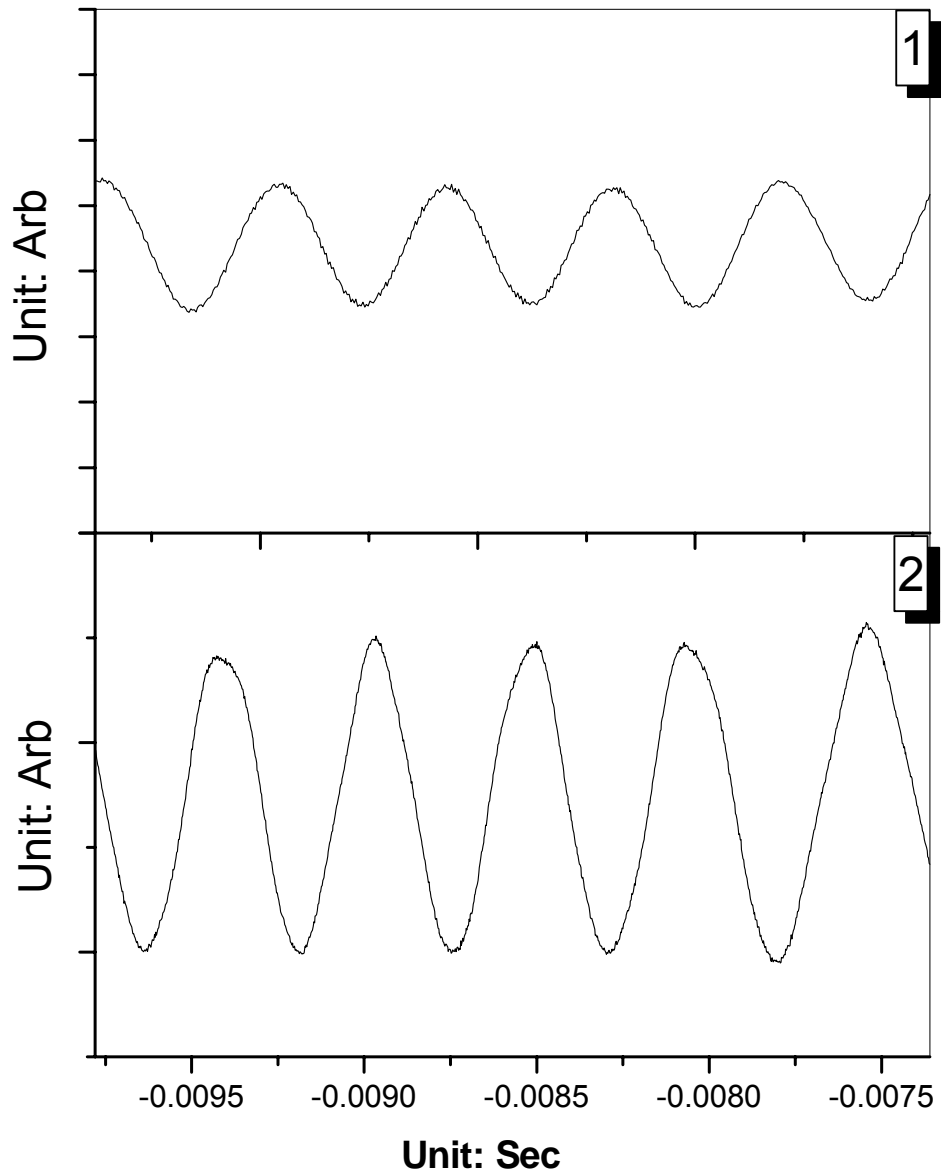


Figure 5 Results of the atomic interference fringes and the optical interference fringes.(1): atomic interference (2): optical interference

2. Single-Zone Atom Interferometer: Wavepacket-Based Theoretical Studies

In an atomic interferometer, the phase shift due to rotation is proportional to the area enclosed by the split components of the atom. In most situations, the atomic wavepacket is split first by what can be considered effectively as an atomic beamsplitter. The split components are then redirected towards each other by atomic mirrors. Finally, the converging components are recombined by another atomic beam splitter. Under these conditions, it is simple to define the area of the interferometer by considering the center of mass motion of the split components. However, this model is invalid for an atomic interferometer demonstrated recently by Shahriar et al. Briefly, in this interferometer, the atom simply passes through a *single-zone* optical beam, consisting of a pair of bichromatic counter-propagating beams. During the passage, the atomic wave packets in two distinct internal states couple to each other *continuously*. The two internal states trace out a complicated trajectory, guided by the optical beams, with the amplitude and spread of each wavepacket varying continuously. Yet, at the end of the single-zone excitation, there is an interference with fringe amplitudes that can reach a visibility close to unity. For such a situation, it is not clear how one would define the area of the interferometer, and therefore, what the rotation sensitivity of such an interferometer would be.

Here, we analyze this interferometer in order to determine its rotation sensitivity, and thereby determine its effective area. In many ways, the continuous interferometer (CI) can be thought of as a limiting version of the three-zone interferometer proposed originally by Borde, and demonstrated by Chu et al. In our analysis, we compare the behavior of the CI with the Borde-Chu Interferometer (BCI). We also identify a quality factor that can be used to compare the performance of these interferometers. Under conditions of practical interest, we show that the rotation sensitivity of the CI can be comparable to that of the BCI. The relative simplicity of the CI (e.g., the task of precise angular alignment of the three zones is eliminated for the CI) then makes it a better candidate for practical atom interferometry for rotation sensing. Furthermore, the CI may be used to realize novel configuration where the wavepackets may trace out multiple loops in a manner such that the rotational sensitivity would vanish, thus making it more versatile for other measurements.

In our comparative analysis, we find it more convenient to generalize the BCI by making the position and duration of the phase-scanner a variable. As such, we end up comparing two types of atomic interferometers to the BCI. The first, which is the generalized version of the BCI, is where instead of a phase scan being applied in only the final $\pi/2$ pulse, the phase scan is applied from some point onwards in the middle π pulse. We find that the magnitude of the rotational phase shift varies according to where the phase is applied from. This phase shift is calculated analytically and compared to the phase shift obtained in the original BCI. The second is the CI, where the atom propagates through only one laser beam with a gaussian field profile. The atom is modeled as a wavepacket with a gaussian distribution in the momentum representation, and its evolution in the laser field is calculated numerically. From this the phase shift with rotation is obtained and compared once again to the phase shift in the BCI.

In the setup for the Borde-Chu Interferometer (BCI), the phase shift due to rotation of the interferometer results from the deviation in position of the lasers. This can be seen as follows. When the BCI is stationary, the laser fields do not have any phase difference relative to each other. Once the BCI begins rotating with some angular velocity Ω around an arbitrary axis, each of the lasers will move a distance relative to the axis of rotation in proportion to Ω . This deviation in position results in a phase shift of the laser fields $\Delta\phi = 2k\Delta y$, where k is the wave number of the lasers and Δy is the change in position. The total phase shift due to the lasers in the BCI is $\delta\phi = \phi_1 - 2\phi_2 + \phi_3$, where the ϕ_i correspond to the phase of the i^{th} laser field.

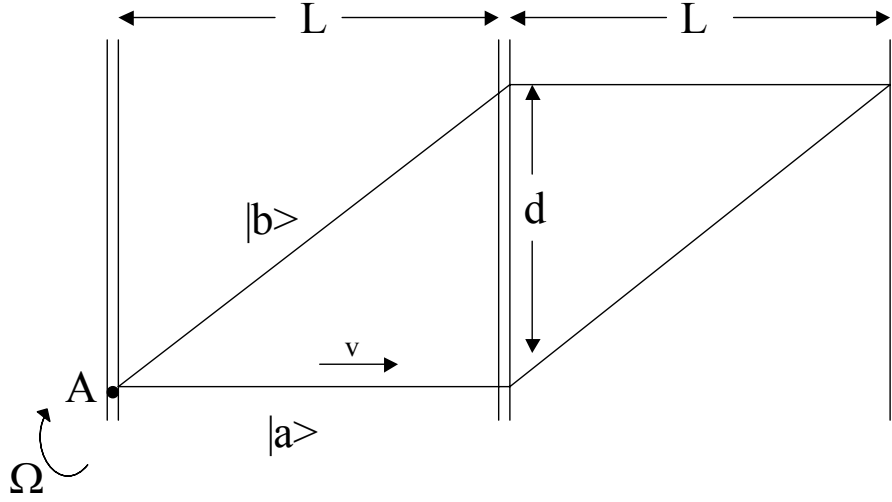


Figure 1: Schematic illustration of the effect of rotation on an atom interferometer.

The rotational phase $\delta\phi$ (see figure 1) is calculated by taking into account the phase shift of each laser resulting from its respective change in position, by the time the atom reaches that laser. If we choose the interferometer to rotate around point A, then $\Delta y_1 = 0$, $\Delta y_2 = L\Omega T$, $\Delta y_3 = 4L\Omega T$, where T is the time the atom takes to go between lasers. Thus $\phi_1 = 0$, $\phi_2 = 2kL\Omega T$, and $\phi_3 = 8kL\Omega T$, and $\delta\phi = 4kL\Omega T$. Since $v_y = \frac{2\hbar k}{m}$, $d = v_y T$, and the area of the interferometer is $A = Ld$, we get

$$\delta\phi = \frac{4\pi\Omega Am}{h} \quad (1)$$

This expression for the rotational phase remains the same regardless of the position of the axis of rotation, as can be explicitly shown. We are also neglecting second order contributions to the rotational phase, which come from the difference in path lengths between the upper and lower arms while rotating.

The fringes of the interferometer are given by the formula for the atom to be in its upper state after going through all three pulses,

$$P = \frac{1}{2}(1 - \cos(\phi)) \quad (2)$$

These fringes are seen by applying a phase ϕ_L to one of the laser fields, say the third one, so that the total phase is $\phi = \phi_L$, and then scanning the phase. When the BCI rotates, the induced rotational phase is added to ϕ_L , which results in a horizontal shift of the original fringes. A measurement of this fringe shift can be used to determine the angular velocity from equation (1).

Let us now consider a system where instead of doing a phase scan by applying a phase only to the third beam (the last $\pi/2$ pulse), we apply a phase partway through the middle π pulse which is of length τ .

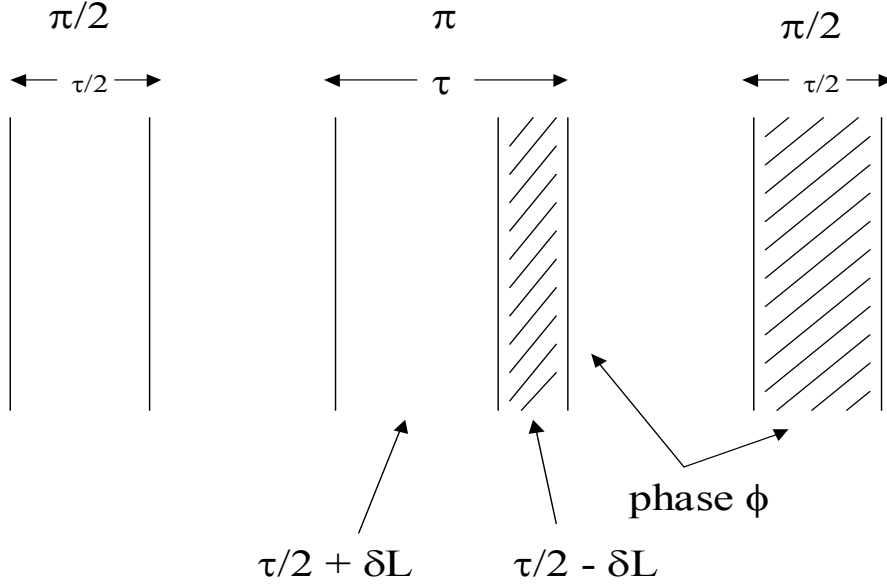


Figure 2: Schematic illustration of the BCI interferometer configuration.

The point from where the phase is applied is denoted by δL (see figure 2). The center of the middle pulse corresponds to $\delta L = 0$, and the phase ϕ is applied at all points in the beam to the left of δL . Thus the middle π pulse is effectively split into two beams, the first one of length $\tau/2 + \delta L$ where there is no phase applied, and the second of length $\tau/2 - \delta L$ where the phase ϕ is applied. We derived equations for the probability amplitude $c_b = \langle b | \Psi \rangle$ of finding the atom in state $|b\rangle$ after passing through all beams. The calculation is done as for the basic BCI, except that now we model the middle π pulse as two separate beams of variable length. We assume that both parts of the middle beam undergo the same phase shift as calculated before, $\phi_c = 2kL\Omega T$. Since the phase shift of the final beam is $\phi_4 = 8kL\Omega T$, we have $\delta\phi = 2\phi_c - \phi_4 = -4kL\Omega T$. The Rabi frequency of the atom is Ω_0 , so $\Omega_0\tau = \pi$. If we write $\tau_2 = \tau/2 - \delta L$, then

$$c_b = \frac{i}{2} \left[\sin\left(\frac{\Omega_0\tau_2}{2}\right) \cos\left(\frac{\Omega_0\tau_2}{2}\right) (\exp(-i\phi_4) - 1)(1 - \exp(-i\phi)) + \right. \\ \left. \cos^2\left(\frac{\Omega_0\tau_2}{2}\right) \exp(-i\phi_2) (\exp(i(\delta\phi - \phi)) - 1) + \sin^2\left(\frac{\Omega_0\tau_2}{2}\right) (\exp(i\delta\phi) - \exp(-i\phi)) \right]$$

In the limit that $\tau_2 = 0$ or $\tau_2 = \tau$, and if the rotation velocity is 0, this equation reduces to equation (2) for the fringes. If the rotation velocity is nonzero, then we obtain the phase shift in equation (1) by using

$P = |c_b|^2$. In order to make a comparison between the rotation sensitivity of the original BCI and this new configuration where the phase is applied at some point in the middle π pulse, we define the effective area A_{eff} as the proportionality constant between the calculated phase shift and Ω ,

$$\delta\phi = \frac{4\pi m\Omega A_{\text{eff}}}{h}.$$

This effective area may or may not be related to the true area of the interferometer. To find the phase shift upon rotation for a system where the phase is applied at some δL , first we take the absolute square of the proper equation above to get P. We then take the derivative of P to find the minimum, and compare how far the minimum shifts as a function of rotation. Since this equation is derived in the limit of small rotation velocities, i.e. small phase shifts for the laser beams, we can Taylor expand all the exponentials to first order, $\exp(i\phi) \approx 1 + i\phi$. After some algebra we obtain the following equation for the phase shift,

$$\delta\phi = \arctan\left(\frac{4kL\Omega T}{2\sin^2\left(\frac{\Omega_0\tau_2}{2}\right) - 1}\right).$$

If we substitute $\tau_2 = \tau/2 - \delta L$ into this expression, we get

$$\delta\phi = \arctan\left(\frac{4kL\Omega T}{\sin(\Omega_0\delta L)}\right)$$

Again we see that in the limit that $\delta L = \pm \tau/2$, the phase shift approaches the previously calculated value of $\delta\phi$. As $\delta L \rightarrow 0$, the phase shift and thus the effective area becomes very large compared to the asymptotic value, eventually approaching the value $\pi/2$. The phase shift at $\delta L = 0$ is second order in the small quantity of the rotation speed Ω , and thus effectively 0.

It is helpful now to define a minimum measurable rotation rate for an interferometer, Ω_{mm} . By rearranging, we see that Ω_{mm} depends on the minimum measurable phase shift $\delta\phi_{mm}$,

$$\Omega_{mm} = \frac{h}{4\pi m} \frac{\delta\phi_{mm}}{A}.$$

The rotational phase shift is determined from the horizontal shift of the phase scan. The minimum measurable phase shift has to be at least as great as the period of the noise on the phase scan. Therefore, if the amplitude of the phase scan is S and the amplitude of the noise is N, $\delta\phi_{mm}$ is given by

$$\delta\phi_{mm} = \frac{\pi}{S/N}.$$

Assuming Poisson distributed noise, the signal to noise ratio cannot be greater than \sqrt{S} . Hence the minimum measurable phase shift is π/\sqrt{S} , and the minimum measurable rotation rate,

$$\Omega_{mm} = \frac{h}{4m} \frac{1}{A\sqrt{S}}.$$

The amplitude of the phase scan for the original BCI is 1. Therefore the minimum measurable rotation rate for a BCI where the phase is applied only in the last $\pi/2$ pulse is

$$\Omega_{mm(BCI)} = \frac{h}{4m} \frac{1}{A_0},$$

where A_0 is the “true area” for the BCI.

Define the quality factor Q as the ratio between the minimum measurable rotation rates of the BCI with phase applied in the last pulse and with the phase applied in the middle pulse (BCI)',

$$Q = \frac{\Omega_{mm(BCI)}}{\Omega_{mm(BCI)'}} = \frac{1/A_0}{1/A_{eff} \sqrt{S}}.$$

If we define the ratio η between the areas as $\eta = A_{eff}/A_0$, Q becomes

$$Q = |\eta| \sqrt{S}.$$

Thus if $Q > 1$, the minimum measurable rotation rate of the new BCI system is smaller than that of the original BCI. This provides us with a framework for comparison of different kinds of interferometer systems, with respect to their rotation sensitivity. We can now directly compare the BCI system with phase applied in the middle pulse with the original BCI by plotting the quality factor Q vs. δL . For this we need the signal strength as a function of δL which is easily calculated,

$$S = \cos^2(\Omega_0 \tau_2)$$

$$\sqrt{S} = \cos(\Omega_0 \tau_2) = \sin(\Omega_0 \delta L)$$

The phase shift of the ordinary BCI is the asymptotic value as $\delta L \rightarrow \pm \tau/2$, so let us call that phase shift $\delta\phi_0$. Then we can rewrite the equation for $\delta\phi$ as

$$\delta\phi = \arctan\left(\frac{\delta\phi_0}{\sin(\Omega_0 \delta L)}\right)$$

In order to calculate η we need the expression for A_{eff} , which is

$$A_{eff} = \frac{h}{4\pi\Omega m} \arctan\left(\frac{\delta\phi_0}{\sin(\Omega_0 \delta L)}\right)$$

By definition $\delta\phi_0 = 4\pi\Omega m A_0 / h$, so

$$\eta = \frac{1}{\delta\phi_0} \arctan\left(\frac{\delta\phi_0}{\sin(\Omega_0 \delta L)}\right)$$

The quality factor is

$$Q = \frac{\sin(\Omega_0 \delta L)}{\delta \phi_0} \arctan\left(\frac{\delta \phi_0}{\sin(\Omega_0 \delta L)}\right)$$

In order to calculate these quantities, it is necessary to consider the wavepacket description of the particles. We are modeling the system as a three level atom in the lambda configuration (figure), with levels $|a\rangle$, $|b\rangle$ and $|e\rangle$, which moves in the x direction through two counter propagating laser beams. The laser beams travel in the z direction and have gaussian electric field profiles varying in the x direction (figure). In the electric dipole approximation, which is valid for our system since the wavelength of the light is much greater than the separation between the electron and the nucleus, we can write the interaction Hamiltonian as $\mathbf{r} \cdot \mathbf{E}$, where \mathbf{r} is the position of the electron and \mathbf{E} is the electric field of the laser. The states of the three level atom are driven by the laser fields. The fields cause transitions between the states $|a\rangle$ and $|e\rangle$ and the states $|e\rangle$ and $|b\rangle$. We also model the atom as a wavepacket in the z direction. In other words, we quantize the position and momentum degrees freedom of the atom in the z direction. Thus the Hamiltonian for the system can be written in the following way,

$$H = \frac{p_z^2}{2m} + H_{\text{int}} + \mathbf{r} \cdot \mathbf{E}_1 + \mathbf{r} \cdot \mathbf{E}_2$$

where \mathbf{E}_1 and \mathbf{E}_2 are the electric field vectors of the two counter propagating lasers. The lasers are taken to be classical electromagnetic fields. We can expand the wavefunction of the atom and the Hamiltonian in the basis for the non-interacting Hamiltonian, which is simply the tensor product of the position and internal eigenstates, $|z\rangle \otimes |i\rangle = |z, i\rangle$. This is a complete set of basis states for our system. In addition, our formulation is simplified considerably if we work in the momentum representation, so we will make this switch and expand the state vector and all operators in terms of the basis $|p, i\rangle$. Since it is understood that all momentums and positions refer to the z direction, we will drop the z subscript on all momentums from hereon. The position operator of the electron in the atom can be expanded in terms of this basis by inserting the identity operator twice, in the form

$$\hat{I} = \int dp \sum_i |p, i\rangle \langle p, i|$$

We also make the assumption that matrix elements of the form $\langle i | \mathbf{r} | i \rangle = 0$. Thus in terms of the dipole matrix elements $\mathbf{d}_{ij} = \langle i | \mathbf{r} | j \rangle$, we can write the position operator as,

$$\begin{aligned} \mathbf{r} &= \int dp \int dp' \sum_{i,j} |p, i\rangle \langle p, i| \mathbf{r} |p', j\rangle \langle p', j| \\ &= \int dp (\mathbf{d}_{ae} |p, a\rangle \langle p, e| + \mathbf{d}_{ea} |p, e\rangle \langle p, a| + \mathbf{d}_{be} |p, b\rangle \langle p, e| + \mathbf{d}_{eb} |p, e\rangle \langle p, b|) \end{aligned}$$

Define the atomic raising and lowering operators as

$$\sigma_{ij} = |p, i\rangle \langle p, j|.$$

In terms of these operators, the position operator is,

$$\mathbf{r} = \int dp (\mathbf{d}_{ae} \sigma_{ae} + \mathbf{d}_{ea} \sigma_{ea} + \mathbf{d}_{be} \sigma_{be} + \mathbf{d}_{eb} \sigma_{eb}).$$

Since the electric field is being modeled classically, we can express each laser field as,

$$\mathbf{E}(z, t) = \mathbf{E} \cos(\omega t - k\hat{z}) = \frac{\mathbf{E}}{2} (\exp(i(\omega t - k\hat{z})) + \exp(-i(\omega t - k\hat{z}))),$$

where \hat{z} is the operator associated with the external position of the atom. The first laser interacts only with that part of the electron position operator which causes transitions $|a\rangle \leftrightarrow |e\rangle$, and the second laser interacts with the part which causes transitions $|b\rangle \leftrightarrow |e\rangle$. We also assume that the dipole matrix elements are real to simplify the expressions,

$$\mathbf{d}_{ae} = \mathbf{d}_{ea} = \mathbf{d}_{ae}^*. \text{ Thus } \mathbf{r} \cdot \mathbf{E}_1 \text{ is,}$$

$$\mathbf{r} \cdot \mathbf{E}_1 = \int dp \frac{\mathbf{d}_{ae} \cdot \mathbf{E}_1}{2} [\sigma_{ae} \exp(i(\omega_1 t - k_1 \hat{z})) + \sigma_{ae} \exp(-i(\omega_1 t - k_1 \hat{z})) + \sigma_{ea} \exp(i(\omega_1 t - k_1 \hat{z})) + \sigma_{ea} \exp(-i(\omega_1 t - k_1 \hat{z}))]$$

Now we make the standard rotating wave approximation which neglects the terms in this expression which do not conserve energy. Also, let $\Omega_1 = \frac{\mathbf{d}_{ae} \cdot \mathbf{E}_1}{\hbar}$, so that finally

$$\mathbf{r} \cdot \mathbf{E}_1 = \int dp \frac{\hbar \Omega_1}{2} [\sigma_{ae} \exp(i(\omega_1 t - k_1 \hat{z})) + \sigma_{ea} \exp(-i(\omega_1 t - k_1 \hat{z}))]$$

There is a similar expression for the $\mathbf{r} \cdot \mathbf{E}_2$ part of the interaction. It is also possible to rewrite the $\exp(ik\hat{z})$ part of the interaction in terms of the $|p, i\rangle$ eigenstates. By inserting the identity expression repeatedly, we get,

$$\begin{aligned} \exp(ik\hat{z}) &= \sum_{i,j} \int dp \int dp' |p, i\rangle \langle p, i| e^{ikz} |p', j\rangle \langle p', j| \\ &= \sum_{i,j} \int dp \int dp' \int dz \int dz' |p, i\rangle \langle p, i| z, i\rangle \langle z, i| e^{ikz} |z', j\rangle \langle z', j| p', j\rangle \langle p', j| \\ &= \sum_{i,j} \int dp \int dp' \int dz \int dz' |p, i\rangle e^{\frac{-ipz}{\hbar}} e^{ikz'} e^{\frac{ip'z'}{\hbar}} \delta_{ij} \delta(z - z') \langle p', j| \\ &= \sum_i \int dp \int dp' |p, i\rangle \langle p', j| \delta\left(k - \frac{p}{\hbar} + \frac{p'}{\hbar}\right) \\ &= \sum_i \int dp |p, i\rangle \langle p - \hbar k, i| \end{aligned}$$

and also $\exp(-ik\hat{z}) = \sum_i \int dp |p, i\rangle \langle p + \hbar k, i|$. The expansion of the non-interacting part of the Hamiltonian in terms of this basis is,

$$H_0 = \int dp \sum_i \left(\frac{p^2}{2m} + \hbar \omega_i \right) \sigma_{ii},$$

where $\hbar\omega_i$ is the energy of the i th level. Combining all these expressions, we finally get the full Hamiltonian in the $|p, i\rangle$ basis,

$$H = \int dp \left[\sum_i \left(\frac{p^2}{2m} + \hbar\omega_i \right) \sigma_{ii} + \frac{\hbar\Omega_1}{2} \left(|p, a\rangle\langle p + \hbar k_1, e| e^{i\omega_1 t} + |p + \hbar k_1, e\rangle\langle p, a| e^{-i\omega_1 t} \right) \right. \\ \left. + \frac{\hbar\Omega_2}{2} \left(|p, b\rangle\langle p + \hbar k_2, e| e^{i\omega_2 t} + |p + \hbar k_2, e\rangle\langle p, b| e^{-i\omega_2 t} \right) \right]$$

For a given value of the momentum p , it is clear that this Hamiltonian creates transitions only between the following manifold of states, $|p, a\rangle \leftrightarrow |p + \hbar k_1, e\rangle \leftrightarrow |p + \hbar k_1 - \hbar k_2, b\rangle$. Therefore it is convenient to shift the value of momentum in the Hamiltonian by making the substitutions $p = q_1 + \hbar k_1$ or $p = q_2 + \hbar k_1 - \hbar k_2$ as appropriate. As an example,

$$\int dp \left(\frac{p^2}{2m} + \hbar\omega_e \right) |p, e\rangle\langle p, e| = \int dq_1 \left(\frac{(q_1 + \hbar k_1)^2}{2m} + \hbar\omega_e \right) |q_1 + \hbar k_1, e\rangle\langle q_1 + \hbar k_1, e| \\ \int dp \left(\frac{p^2}{2m} + \hbar\omega_b \right) |p, b\rangle\langle p, b| = \\ \int dq_2 \left(\frac{(q_2 + \hbar k_1 - \hbar k_2)^2}{2m} + \hbar\omega_b \right) |q_1 + \hbar k_1 - \hbar k_2, b\rangle\langle q_1 + \hbar k_1 - \hbar k_2, b| \\ \int dp |p, b\rangle\langle p + \hbar k_2, e| = \int dq_2 |q_2 + \hbar k_1 - \hbar k_2, b\rangle\langle q_2 + \hbar k_1, e|$$

Thus if we define the states,

$$|1\rangle = |p, a\rangle \\ |2\rangle = |p + \hbar k_1, e\rangle \\ |3\rangle = |p + \hbar k_1 - \hbar k_2, b\rangle$$

we can rewrite the Hamiltonian as,

$$H = \int dp \left[\sum_i E_i \sigma_{ii} + \frac{\hbar\Omega_1}{2} \left(|1\rangle\langle 2| e^{i\omega_1 t} + |2\rangle\langle 1| e^{-i\omega_1 t} \right) + \frac{\hbar\Omega_2}{2} \left(|3\rangle\langle 2| e^{i\omega_2 t} + |2\rangle\langle 3| e^{-i\omega_2 t} \right) \right]$$

where the E_i are the energies of the newly defined states. By redefining the states in this way, it is clear that the momentum is simply a parameter labeling which manifold of states we are in, and not a true dynamical variable. Once the atom has some momentum p , the Hamiltonian cannot move the atom to a manifold of states with some other momentum. The only transitions that can occur are between the states $|1\rangle$, $|2\rangle$ and $|3\rangle$, for the given momentum. Thus to study the dynamics of the atom, it is sufficient to consider only one manifold with some momentum p . Once solved, we can integrate over all p to get the motion of the full wavepacket. Since the laser beams are counter propagating at the same frequency, we have $k_1 = -k_2 = k$, and the states become,

$$\begin{aligned}|1\rangle &= |p, a\rangle \\ |2\rangle &= |p + \hbar k, e\rangle \\ |3\rangle &= |p + 2\hbar k, b\rangle\end{aligned}$$

The state of the atom is expanded in the $|p, i\rangle$ basis as

$$\begin{aligned}|\Psi(t)\rangle &= \int dp \sum_i \psi_i(p, t) |p, i\rangle \\ &= \int dp (\alpha(p, t) |p, a\rangle + \beta(p + 2\hbar k, t) |p + 2\hbar k, b\rangle + \xi(p + \hbar k, t) |p + \hbar k, e\rangle)\end{aligned}$$

The state of the atom evolves according to the Schrodinger equation,

$$i\hbar \frac{d|\Psi\rangle}{dt} = H\Psi.$$

If we make a unitary transformation U on the state $|\Psi\rangle$ to some interaction picture state vector $|\tilde{\Psi}\rangle = U|\Psi\rangle$, then the Hamiltonian in this interaction picture is,

$$\tilde{H} = UHU^{-1} + i\hbar \frac{dU}{dt}.$$

Let $U = \int dp \sum_j e^{i\theta_j t} |j\rangle$, where the $|j\rangle$ are the redefined states and the θ_j are parameters we will choose to simplify the interaction picture Hamiltonian. Written in matrix form, the Hamiltonian for some momentum p is,

$$H(p) = \begin{bmatrix} E_1 & 0 & \frac{\hbar\Omega_1}{2} e^{i\omega_1 t} \\ 0 & E_3 & \frac{\hbar\Omega_2}{2} e^{i\omega_2 t} \\ \frac{\hbar\Omega_1}{2} e^{-i\omega_1 t} & \frac{\hbar\Omega_2}{2} e^{-i\omega_2 t} & E_2 \end{bmatrix}$$

where the rows and columns are arranged with the states in $|1\rangle, |3\rangle, |2\rangle$ order. In the interaction picture with the parameters θ_j , the Hamiltonian is,

$$\tilde{H}(p) = \begin{bmatrix} E_1 - \hbar\theta_1 & 0 & \frac{\hbar\Omega_1}{2} e^{i(\omega_1 + \theta_1 - \theta_2)t} \\ 0 & E_3 - \hbar\theta_3 & \frac{\hbar\Omega_2}{2} e^{i(\omega_2 + \theta_3 - \theta_2)t} \\ \frac{\hbar\Omega_1}{2} e^{-i(\omega_1 + \theta_1 - \theta_2)t} & \frac{\hbar\Omega_2}{2} e^{-i(\omega_2 + \theta_3 - \theta_2)t} & E_2 - \hbar\theta_2 \end{bmatrix}$$

First to get rid of the time dependence, set $\omega_1 + \theta_1 - \theta_2 = 0$, and $\omega_2 + \theta_3 - \theta_2 = 0$. Define the detunings

$$\begin{aligned}\hbar\Delta_1 &= E_1 + \hbar\omega_1 - E_2 \\ \hbar\Delta_2 &= E_3 + \hbar\omega_2 - E_2 \\ \hbar\Delta &= \hbar(\Delta_1 - \Delta_2) \\ \hbar\delta &= \frac{\hbar(\Delta_1 + \Delta_2)}{2}\end{aligned}$$

A consistent choice of the θ parameters which also improves the form of the Hamiltonian considerably is,

$$\begin{aligned}\hbar\theta_1 &= \frac{E_1 + E_3 - \hbar\omega_1 + \hbar\omega_2}{2} \\ \hbar\theta_2 &= \frac{E_1 + E_3 + \hbar\omega_1 + \hbar\omega_2}{2} \\ \hbar\theta_3 &= \frac{E_1 + E_3 + \hbar\omega_1 - \hbar\omega_2}{2}\end{aligned}$$

With this choice, the Hamiltonian becomes,

$$\tilde{H}(p) = \hbar \begin{bmatrix} \frac{\Delta}{2} & 0 & \frac{\Omega_1}{2} \\ 0 & -\frac{\Delta}{2} & \frac{\Omega_2}{2} \\ \frac{\Omega_1}{2} & \frac{\Omega_2}{2} & -\delta \end{bmatrix}$$

The equations of motion for these three states at a given momentum are:

$$\begin{aligned}i\hbar\dot{\tilde{\alpha}}(p,t) &= \frac{\hbar\Delta}{2}\tilde{\alpha}(p,t) + \frac{\hbar\Omega_1}{2}\tilde{\xi}(p+\hbar k,t) \\ i\hbar\dot{\tilde{\beta}}(p+2\hbar k,t) &= -\frac{\hbar\Delta}{2}\tilde{\beta}(p+2\hbar k,t) + \frac{\hbar\Omega_2}{2}\tilde{\xi}(p+\hbar k,t) \\ i\hbar\dot{\tilde{\xi}}(p+\hbar k,t) &= -\hbar\delta\tilde{\xi}(p+\hbar k,t) + \frac{\hbar\Omega_1}{2}\tilde{\alpha}(p,t) + \frac{\hbar\Omega_2}{2}\tilde{\beta}(p+2\hbar k,t)\end{aligned}$$

Since the laser beams are far detuned from resonance, we can make the adiabatic approximation, which can be verified afterwards for consistency. This approximation is that the intermediate $|2\rangle$ state occupation is negligible and that we can set $\dot{\tilde{\xi}} \approx 0$. Thus with this approximation, we can reduce this three level system to a two level system by solving for $\tilde{\xi}$ in the third equation and substituting into the first two. We get,

$$\tilde{\xi} = -\frac{\Omega_1}{2\delta}\tilde{\alpha} - \frac{\Omega_2}{2\delta}\tilde{\beta}$$

and the effective two level Hamiltonian,

$$\tilde{H}_{eff}(p) = \hbar \begin{bmatrix} \frac{\Delta}{2} + \frac{\Omega_1^2}{4\delta} & \frac{\Omega_1\Omega_2}{4\delta} \\ \frac{\Omega_1\Omega_2}{4\delta} & -\frac{\Delta}{2} + \frac{\Omega_2^2}{4\delta} \end{bmatrix}.$$

In our system, we assume that the counter-propagating laser beams have the same strength, $\Omega_1 = \Omega_2$, so we define the effective Rabi frequency $\Omega_R = \frac{\Omega_1\Omega_2}{2\delta}$. Thus the effective Hamiltonian becomes,

$$\tilde{H}_{eff}(p) = \hbar \begin{bmatrix} \frac{\Delta}{2} + \frac{\Omega_R}{2} & \frac{\Omega_R}{2} \\ \frac{\Omega_R}{2} & -\frac{\Delta}{2} + \frac{\Omega_R}{2} \end{bmatrix}.$$

The expressions for the detunings are,

$$\Delta = \Delta_0 - \frac{2kp}{m} - \frac{2\hbar k^2}{m}$$

$$\delta = \delta_0 + \frac{\hbar k^2}{2m},$$

where $\Delta_0 = \omega_1 - \omega_2 + \omega_a - \omega_b$ and $\delta_0 = (\omega_1 + \omega_2 + \omega_a + \omega_b - 2\omega_b)/2$. This effective Hamiltonian can be solved by standard methods for $\tilde{\alpha}(p, t)$ and $\tilde{\beta}(p + 2\hbar k, t)$. Once we have the solutions for some Ω_R and at a given value of p , then we can write down the full expression for the state vector integrated over all p . Ignoring any global phase factors which do not depend on p , we get,

$$\begin{aligned} |\Psi(t)\rangle &= \int dp (\alpha(p, t)|p, a\rangle + \beta(p + 2\hbar k, t)|p + 2\hbar k, b\rangle) \\ &= \int dp (e^{-i\theta_a t} \tilde{\alpha}(p, t)|p, a\rangle + e^{-i\theta_b t} \tilde{\beta}(p + 2\hbar k, t)|p + 2\hbar k, b\rangle) \\ &= \int dp \exp\left(\frac{-i(p^2 + (p + 2\hbar k)^2)}{4m\hbar} t\right) (\tilde{\alpha}(p, t)|p, a\rangle + \tilde{\beta}(p + 2\hbar k, t)|p + 2\hbar k, b\rangle) \end{aligned}$$

In our analysis of the rotational sensitivity, we must apply this solution for the state vector for the case of a gaussian profile in the x direction. We simply discretize the gaussian profile and propagate stepwise along the discrete profile until we reach the time desired. From the normal rules of quantum mechanics, the position representation wavefunctions for the $|a\rangle$ and $|b\rangle$ states are,

$$\psi_a(x, t) = \int dp \alpha(p, t) \exp\left(\frac{-ipx}{\hbar}\right)$$

$$\psi_b(x,t) = \int dp \beta(p + 2\hbar k, t) \exp\left(\frac{-ipx}{\hbar}\right),$$

and the probabilities for the atom to be in either state are,

$$P(a) = \int dp |\alpha(p, t)|^2$$

$$P(b) = \int dp |\beta(p, t)|^2 .$$

The functions η , S , and Q calculated using this approach are plotted below (figures 3 and 4) for the parameters $\Omega_0 = 2\pi(7 \times 10^4)$, $L = 3 \times 10^{-3}$ m, and $k = 8.055 \times 10^6$ m⁻¹.

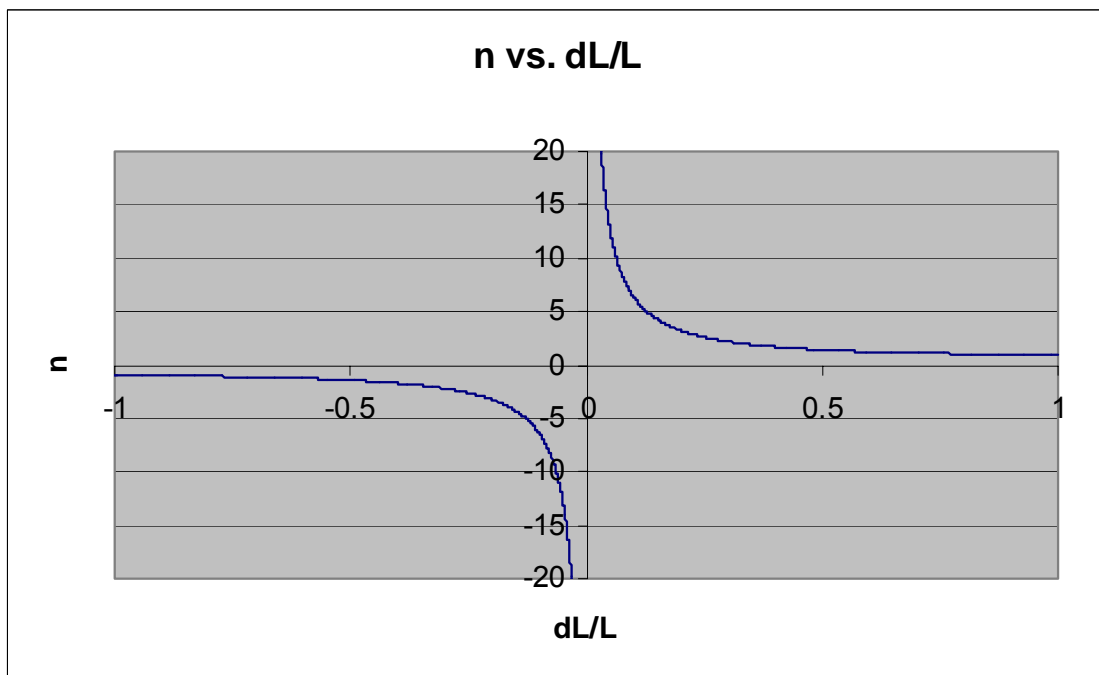


Figure 3: Numerically computed plot of η as a function of dL/L .

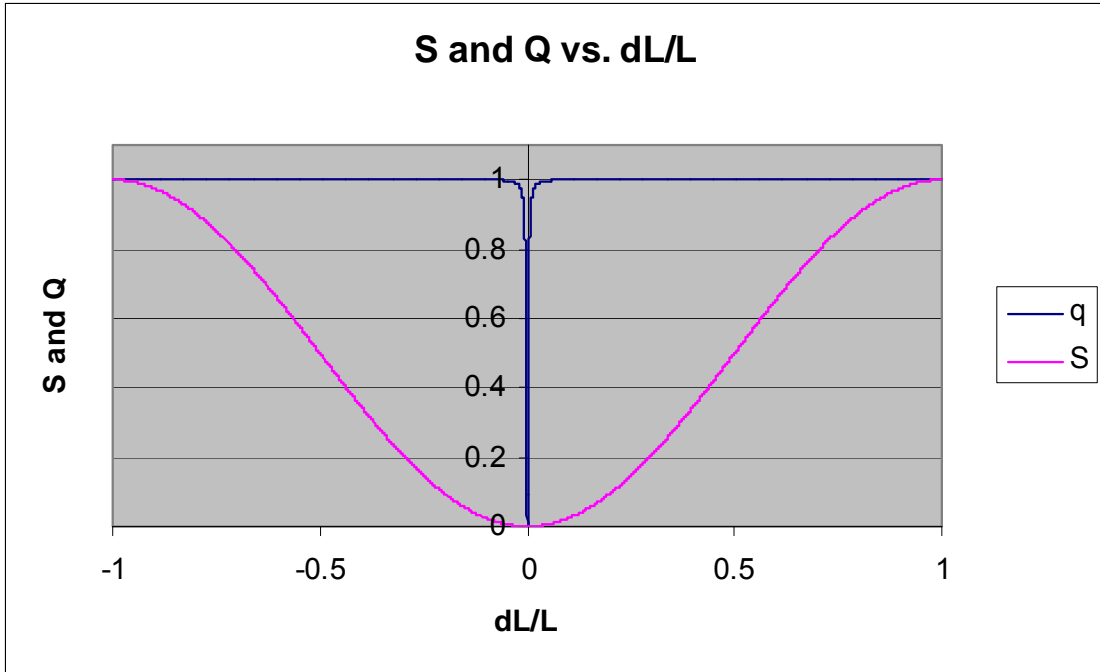


Figure 4: Numerically computed plot of S and Q as functions of dL/L .

Our setup differs (see figure 5) from the BCI in that the atom traverses a single laser beam with a gaussian electric field profile in the transverse direction.

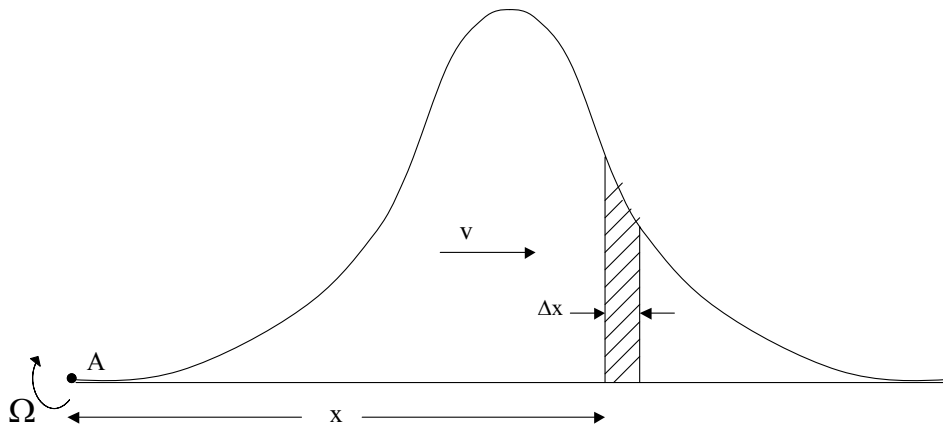


Figure 5: Schematic Illustration of the effect of rotation on the single zone atomic interferometer.

As the atom passes through the beam the wavepackets for the $|a\rangle$ and $|b\rangle$ states take different trajectories depending on the width of the beam and the effective Rabi frequency Ω_0 . In order to do a phase scan in this system, we apply a phase to this laser pulse starting from some position δL measured from the center of the pulse and extending in the direction of propagation of the atom. We see that this configuration is analogous to the BCI system analyzed previously where the phase is applied from the second laser beam. If this interferometer is made to rotate, there

will again be a rotational phase shift. We expect that there will be a variation of the effective area and signal strength with δL , and that it will be similar to the BCI. This phase shift is calculated in a manner similar to before, except that now the atom sees a continuously different phase as it travels in the x direction. We can imagine the laser profile being sliced up into infinitesimal intervals Δx in the transverse direction. Each one of these slices is rotating with angular velocity Ω , but will have a different deviation in the y direction depending on how far away it is from the axis of rotation. This will lead to the atom seeing a different phase shift at every point x in the laser profile. In our simulations, we placed the axis of rotation at the point A in the diagram.

The phase shift for this interferometer is also linear for infinitesimal rotations. Thus an effective area for this interferometer can be defined as before. We chose to simulate a system with the following parameters, $\Omega_0 = 2\pi (7 \times 10^4)$ and $L = 3 \times 10^{-3}$ m, such that $\Omega_0 T = 3.3$. The variations of the effective area and signal strength with $\delta L/L$ were determined numerically and are plotted below (see figures 6 and 7).

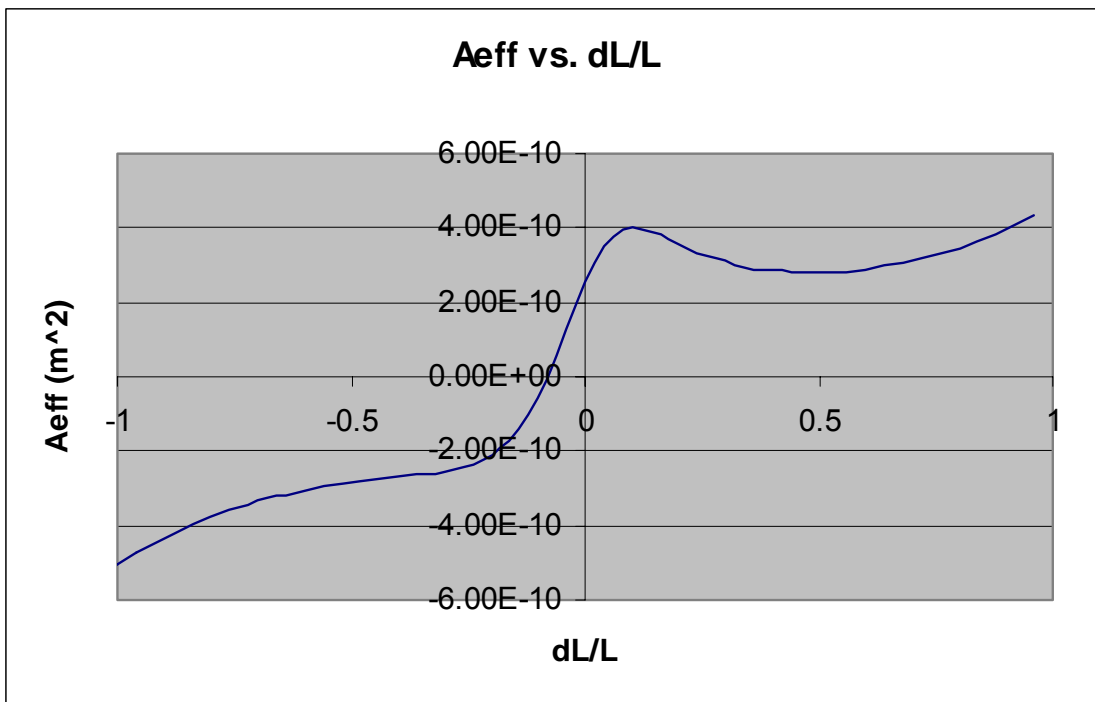


Figure 6: Numerically computed plot of A_{eff} as a function of dL/L

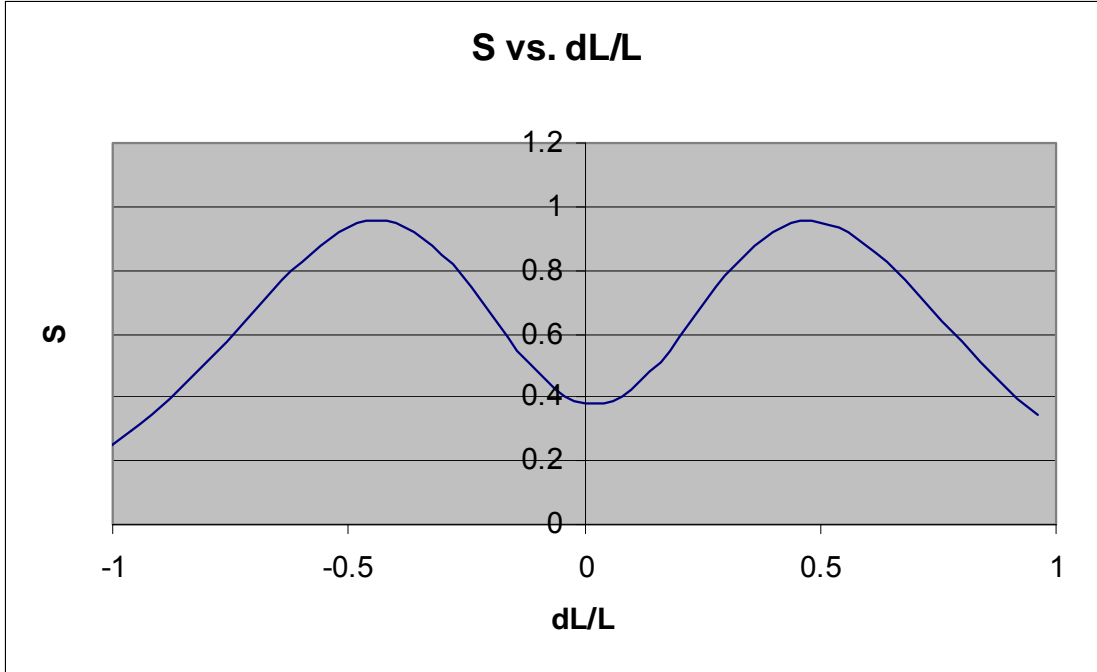


Figure 7: Numerically computed plot of A_{eff} as a function of dL/L

In order to compare this rotation sensitivity with that of a BCI, we now need to know the area of the BCI corresponding to our system. Since in our interferometer the interaction between the electric field and the atom is continuous, the choice of the area of this BCI is fairly arbitrary. Fortunately though, two options present themselves immediately and happen to give the same answer. One is to note that the greatest interaction in the gaussian laser profile occurs within one standard deviation of the peak of the profile. Thus it makes sense to define an equivalent BCI with a length between lasers of $L = 3 \times 10^{-3}$ m, which is the $1/e$ length of the gaussian profile. The second option is to take advantage of the similarity between the graphs of effective area vs. $\delta L/L$ and S vs. $\delta L/L$ for both interferometers. In both cases, S is symmetric around $\delta L = 0$, and reaches a maximum on both sides. In the case of our interferometer, the effective area temporarily levels off to some value as the signal approaches the maximum, before increasing or decreasing on either side. The same effect occurs in the BCI, where the effective area goes to it's asymptotic value as the signal strength approaches one. For our interferometer, the signal strength reaches a maximum of 0.955 at $\delta L/L = \pm 12$, and at $\delta L/L = \pm 12$, $A_{\text{eff}} = 2.8 \times 10^{-10}$ m². Therefore, we can draw the analogy that the “asymptotic value” that the effective area levels off to in the case of our interferometer corresponds to the BCI equivalent to our system. The area of a BCI is given by the following formula

$$A_0 = L^2 \frac{2\hbar k/m}{v_x},$$

and $L = 3 \times 10^{-3}$ m gives $A_0 = 2.7 \times 10^{-10}$ m². Hence it is sensible to compare our system with a BCI that has a length between lasers of 3×10^{-3} m. With this value of A_0 we can go through the same steps as for the BCI and work out the variation of the quality factor Q as a function of $\delta L/L$. $\eta = A_{\text{eff}}/A_0$, S and Q vs. $\delta L/L$ are plotted below (see figures 8, 9 and 10).

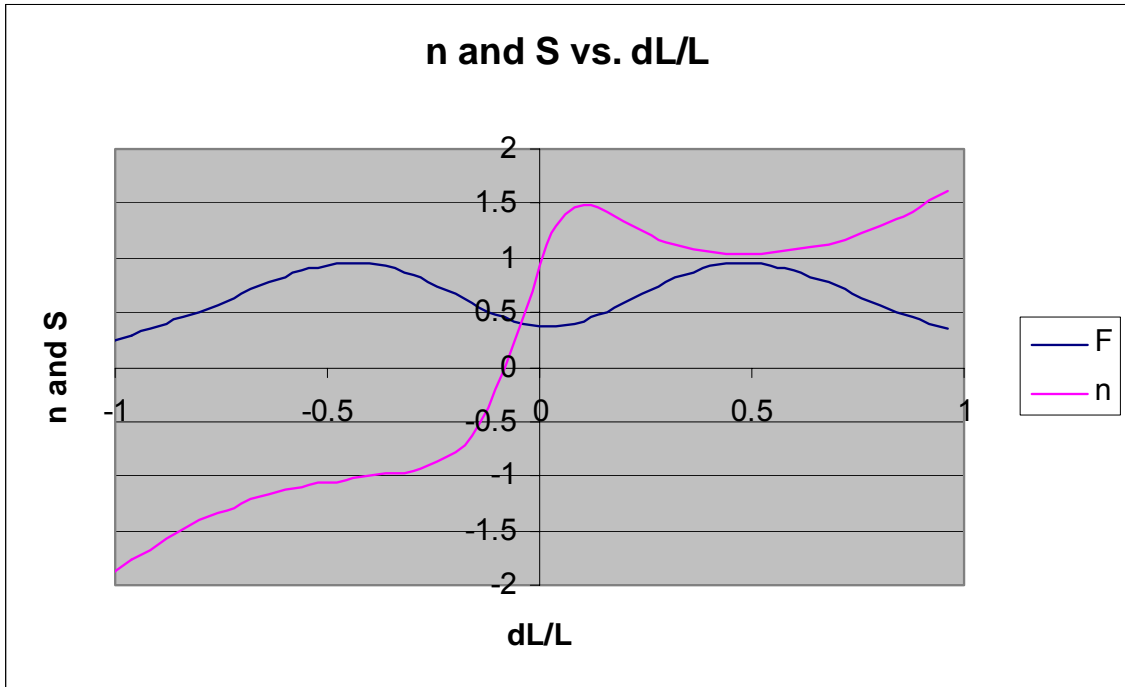


Figure 8: Numerically computed plot of η and S as functions of dL/L

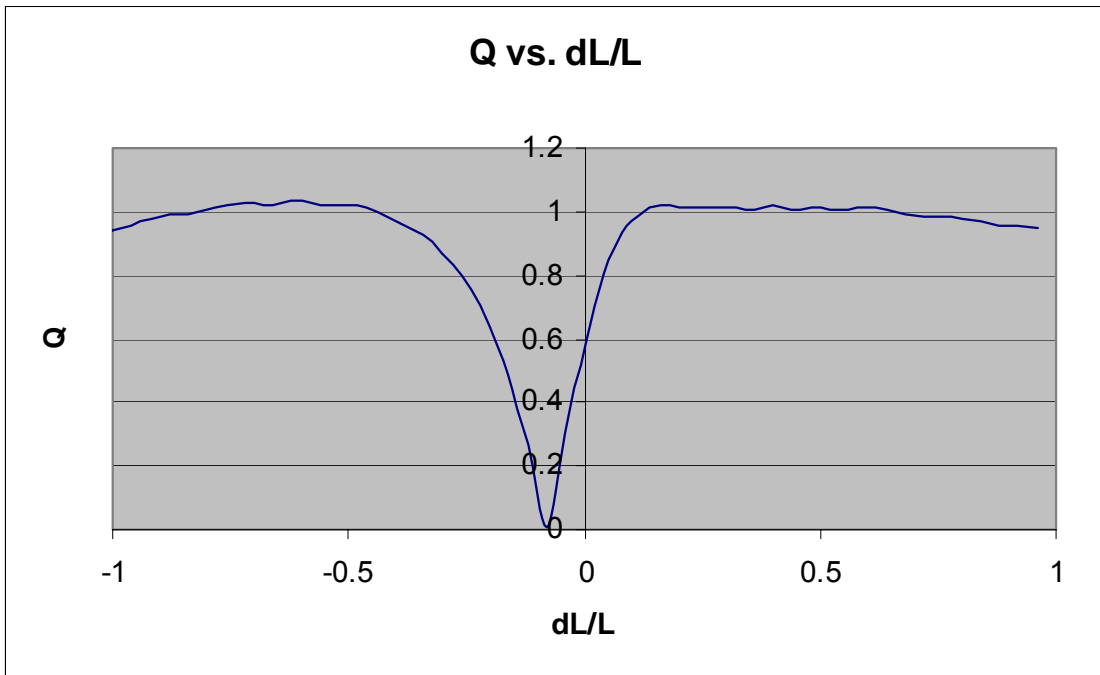


Figure 9: Numerically computed plot of Q as a function of dL/L

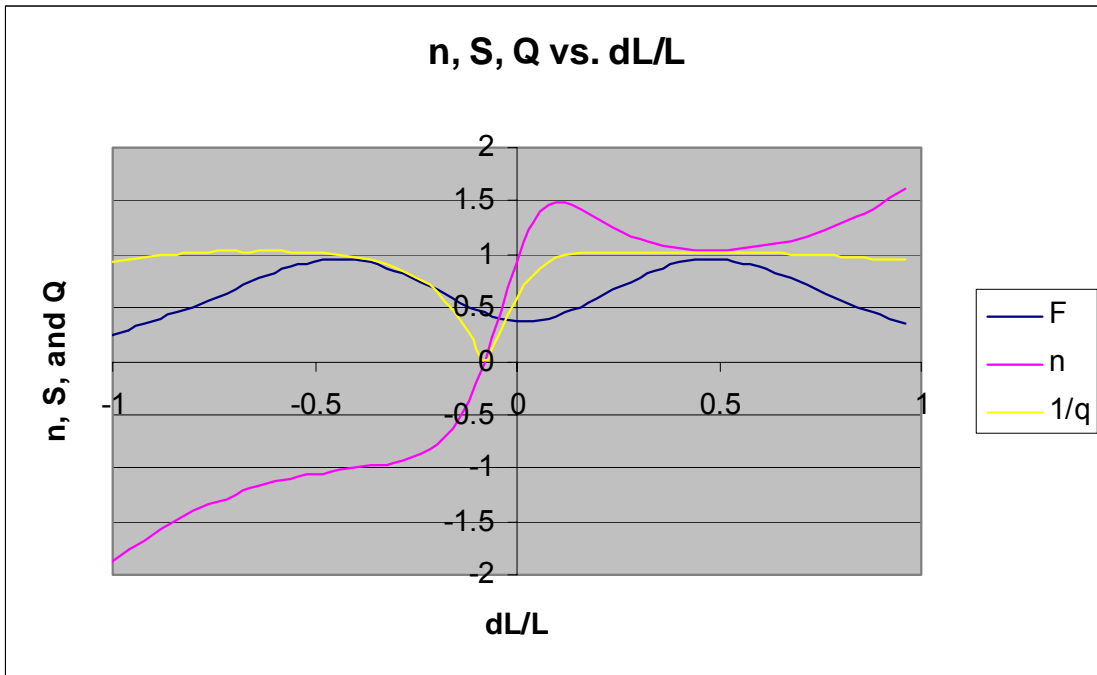


Figure 9: Combined view of numerically computed values of η , S and Q as functions of dL/L

The quality factor for our interferometer has a shape very similar to the BCI. However, the effective area varies smoothly through 0 in contrast to the BCI, which affects the variation of the quality factor as well. The signal amplitude also never reaches 0, as it does in the BCI. The quality factor is approximately one for $|\delta L/L| > 0.25$, which means that our interferometer provides the same rotation sensitivity as a BCI of the same size as our system.

An additional observation is that the above results for the rotational phase shifts and effective areas do not depend on whether the shift is measured at the minimum or maximum of the phase scan. This is true for the BCI and our interferometer as well. This is counterintuitive if one starts with the assumption that the “area of the interferometer” has something to do with the phase shift. The reason is because application of a phase in the gaussian profile of the laser beam perturbs the trajectories of the $|a\rangle$ and $|b\rangle$ wavepackets. Each different value of the phase applied results in a different trajectory for the wavepackets. Thus in a phase scan, we are actually comparing completely different trajectories, since the scan goes over some range of phases. Therefore, if the trajectories have anything to do at all with the rotational phase shift, then the shift we see on the phase scan should vary depending on phase. Following this logic, the phase scan in the neighborhood of $\phi = \pi$ (the minimum) should be shifted by a different value than near $\phi = 0$ (the maximum). This in fact, does not happen. In other words, completely different trajectories give the same effective area A_{eff} .

3. Observation of Optical Phase via Incoherent Detection of Fluorescence using the Bloch-Siegert Oscillation

It is well known that the amplitude of an atomic state is necessarily complex. Whenever a measurement is made, the square of the absolute value of the amplitude is the quantity we generally measure or observe. The timing signal from a clock (as represented, e.g., by the amplitude of the magnetic field of an rf oscillator locked to the clock transition), on the other hand, is *real*, composed of the sum of two complex components. In describing the atom-field interaction, one often side-steps this difference by making what is called the *rotating wave approximation* (RWA), under which only one of the two complex components is kept, and the fast rotating part is ignored. As a result, generally an atom interacting with a field enables one to measure only the intensity, and not the amplitude and the phase of the driving field. This is the reason why most detectors are so-called square-law detectors.

Of course, there are many ways to detect the phase of an oscillating field. For example, one can employ heterodyne detection, which is employed in experiments involving quadrature squeezing, etc.. In such an experiment, the weak squeezed field is *multiplied* by a strong field (of a local oscillator: LO). An atom (or a semiconductor quantum dot), acting still under the *square-law* limit, can detect this *multiplied* signal, which varies with the phase difference between the weak field and the LO.

Here, we show how a single atom by itself can detect the phase of a Rabi driving electromagnetic field by making use of the fact that the two complex parts of the clock field have exactly equal but opposite frequencies (one frequency is the negative of the other), and have exactly correlated phases. By using the so called counter-rotating complex field (which is normally ignored as discussed above) as the LO, we can now measure the amplitude and the phase of the driving field. We also propose a practical experimental scheme for making this measurement using rubidium thermal atomic beam in a strong driving magnetic field as described below.

We assume an ideal two-level system where a ground state $|0\rangle$ which is coupled to a higher energy state $|1\rangle$. We also assume that the 0-1 transitions are magnetic dipolar, with a transition frequency ω . For example, in the case of ^{87}Rb , $|0\rangle$ may correspond to $5^2P_{1/2}; |F=1, m_F=-1\rangle$ magnetic sublevel, and $|1\rangle$ may correspond to $5^2P_{1/2}; |F=2, m_F=0\rangle$ magnetic sublevel. Left and right circularly polarized magnetic fields, perpendicular to the quantization axis, are used to excite the 0-1 transitions⁶.

We assume that magnetic field to be of the form $B=B_0\text{Cos}(\omega t+\phi)$ where the value of the phase can be determined by the choice of a proper time origin. We now summarize briefly a two-level dynamics *without* RWA. Consider, for example, the excitation of the $|0\rangle \leftrightarrow |1\rangle$ transition. In the dipole approximation, the Hamiltonian can be written as:

$$\hat{H} = \begin{bmatrix} 0 & g(t) \\ g(t) & \varepsilon \end{bmatrix} \quad (1)$$

where $g(t) = -g_0[\exp(i\omega t+i\phi)+\text{c.c.}]/2$, and $\varepsilon=\omega$ corresponding to resonant excitation. The state vector is written as:

$$|\xi(t)\rangle = \begin{bmatrix} C_0(t) \\ C_1(t) \end{bmatrix} \quad (2)$$

We now perform a rotating wave transformation by operating on $|\xi(t)\rangle$ with the unitary operator \hat{Q} , given by:

$$\hat{Q} = \begin{bmatrix} 1 & 0 \\ 0 & \exp(i\omega t + i\phi) \end{bmatrix} \quad (3)$$

The Schrodinger equation then takes the form (setting $\hbar=1$):

$$\frac{\partial |\tilde{\xi}(t)\rangle}{\partial t} = -i\tilde{H}(t)|\tilde{\xi}(t)\rangle \quad (4)$$

where the effective Hamiltonian is given by:

$$\tilde{H} = \begin{bmatrix} 0 & \alpha(t) \\ \alpha^*(t) & 0 \end{bmatrix} \quad (5)$$

with $\alpha(t) = -g_0[\exp(-i2\omega t - i2\phi) + 1]/2$, and the rotating frame state vector is:

$$|\tilde{\xi}(t)\rangle \equiv \hat{Q}|\xi(t)\rangle = \begin{bmatrix} \tilde{C}_0(t) \\ \tilde{C}_1(t) \end{bmatrix} \quad (6)$$

Now, one may choose to make the rotating wave approximation (RWA), corresponding to dropping the fast oscillating term in $\alpha(t)$. This corresponds to ignoring effects (such as the Bloch-Siegert shift) of the order of (g_0/ω) , which can easily be observable in experiment if g_0 is large⁷⁻¹⁰. On the other hand, by choosing g_0 to be small enough, one can make the RWA for any value of ω . We explore both regimes here. As such, we find the general results without the RWA.

From Eqs.4 and 6, one gets two coupled differential equations:

$$\dot{\tilde{C}}_0(t) = -\frac{g_0}{2}[-\sin(\omega t + \alpha)\cos(\omega t + \alpha) - i\cos^2(\omega t + \alpha)]\tilde{C}_1(t) \quad (7a)$$

$$\dot{\tilde{C}}_1(t) = -\frac{g_0}{2}[+\sin(\omega t + \alpha)\cos(\omega t + \alpha) - i\cos^2(\omega t + \alpha)]\tilde{C}_0(t) \quad (7b)$$

We assume $|C_0(t)|^2 = 1$ is the initial condition, and proceed further to find an approximate analytical solution of the Eq.7. Given the periodic nature of the effective Hamiltonian, the general solution to Eq.7 can be written in the form of Bloch's periodic functions:

$$|\tilde{\xi}(t)\rangle = \sum_{n=-\infty}^{\infty} |\xi_n\rangle \beta^n \quad (8)$$

where $\beta = \exp(-i2\omega t - i2\phi)$, and

$$|\xi_n\rangle \equiv \begin{bmatrix} a_n \\ b_n \end{bmatrix} \quad (9)$$

Insertin Eq.8 in Eq.7, and equating coefficients with same frequencies, one gets, for all n:

$$\dot{a}_n = i2n\omega a_n + ig_o(b_n + b_{n-1})/2 \quad (10a)$$

$$\dot{b}_n = i2n\omega b_n + ig_o(a_n + a_{n+1})/2 \quad (10b)$$

In the absence of the RWA, the coupling to additional levels results from virtual multi-photon processes. Here, the coupling between a_o and b_o is the conventional one present when the RWA is made. The couplings to the nearest neighbors, $a_{\pm 1}$ and $b_{\pm 1}$ are detuned by an amount 2ω , and so on. To the lowest order in (g_o/ω) , we can ignore terms with $|n|>1$, thus yielding a truncated set of six equations.:

$$\dot{a}_o = ig_o(b_o + b_{-1})/2 \quad (11a)$$

$$\dot{b}_o = ig_o(a_o + a_1)/2 \quad (11b)$$

$$\dot{a}_1 = i2\omega a_1 + ig_o(b_1 + b_o)/2 \quad (11c)$$

$$\dot{b}_1 = i2\omega b_1 + ig_o a_1 / 2 \quad (11d)$$

$$\dot{a}_{-1} = -i2\omega a_{-1} + ig_o b_{-1} / 2 \quad (11e)$$

$$\dot{b}_{-1} = -i2\omega b_{-1} + ig_o(a_{-1} + a_o)/2 \quad (11f)$$

To solve these equations, one may employ the method of adiabatic elimination which is valid for first order in $\sigma \equiv (g_o/4\omega)$. Consider first the last two Eqs.11e and 11f. In order to simplify these two equations further, one needs to diagonalize the interaction between a_{-1} and b_{-1} . Define $\mu_- \equiv (a_{-1} - b_{-1})$ and $\mu_+ \equiv (a_{-1} + b_{-1})$, which now can be used to re-express these two equations in a symmetric form as:

$$\dot{\mu}_- = -i(2\omega + g_o/2)\mu_- - ig_o a_o / 2 \quad (12.a)$$

$$\dot{\mu}_+ = -i(2\omega - g_o/2)\mu_+ + ig_o a_o / 2 \quad (12.b)$$

Adiabatic following then yields (again, to lowest order in σ):

$$\mu_- \approx -\sigma a_o; \quad \mu_+ \approx \sigma a_o \quad (13)$$

which in turn yields:

$$a_{-1} \approx 0; \quad b_{-1} \approx \sigma a_o \quad (14)$$

In the same manner, we can solve equations 11c and 11d, yielding:

$$a_1 \approx -\sigma b_o; \quad b_1 \approx 0 \quad (15)$$

Note that the amplitudes of a_1 and b_1 are vanishing (each proportional to σ^2) to lowest order in σ , and thereby justifying our truncation of the infinite set of relations in Eq.9. Using Eq.14 and 15 in Eqs.11a and 11b, we get:

$$\dot{a}_o = ig_o b_o / 2 + i\Delta a_o / 2 \quad (16a)$$

$$\dot{b}_o = ig_o a_o / 2 - i\Delta b_o / 2 \quad (16b)$$

where $\Delta = g_o^2 / 4\omega$ is essentially the Bloch-Siegert shift. Eq.16 can be thought of as a two-level system excited by a field detuned by Δ . With the initial condition of all the population in $|0\rangle$ at $t=0$, the only non-vanishing (to lowest order in σ) terms in the solution of Eq.9 are:

$$\begin{aligned} a_o(t) &\approx \text{Cos}(g_o t / 2); & b_o(t) &\approx i \text{Sin}(g_o t / 2) \\ a_1(t) &\approx -i\sigma \text{Sin}(g_o t / 2); & b_{-1}(t) &\approx \sigma \text{Cos}(g_o t / 2) \end{aligned} \quad (17)$$

We have verified this solution via numerical integration of Eq.7 as shown later. Inserting this solution in Eq.7, and reversing the rotating wave transformation, we get the following expressions for the components of Eq.2 :

$$C_0(t) = \text{Cos}(g_o t / 2) - 2\sigma \Sigma \cdot \text{Sin}(g_o t / 2) \quad (18a)$$

$$C_1(t) = ie^{-i(\omega t + \phi)} [\text{Sin}(g_o t / 2) + 2\sigma \Sigma^* \cdot \text{Cos}(g_o t / 2)] \quad (18b)$$

where we have defined $\Sigma \equiv (i/2) \exp[-i(2\omega t + 2\phi)]$. To lowest order in σ , this solution is normalized at all times. Note that if one wants to carry this excitation on an ensemble of atoms using $\pi/2$ pulse and measure the population of the state $|1\rangle$ immediately (at $t=\tau$, $\pi/2$ excitation ends), the result would be a signal given by

$$|C_1(t = \tau, g = g_o, \phi)|^2 = \frac{1}{2} [1 + 2\sigma \text{Sin}(2\omega\tau + 2\phi)], \quad (19)$$

which contains information of the both, amplitude and phase, of the driving field. *This is our main result.*

A physical realization of this result can be appreciated best by considering an experimental arrangement of the type illustrated in Fig.1. Here rubidium thermal atoms are passing through the strong periodic magnetic field. The total passage-time of an atom through the magnetic field is τ which includes switching on and switching off time scale τ_{switch} . The states of the atoms are measured immediately after the atoms leave the magnetic field.

In Fig.2 (a) we have shown the evolution of the excited state population $|C_1(t)|^2$ with time, which is the Rabi oscillation, by plotting the analytical Eq.18(b). The finer oscillation part of the total Rabi oscillation $|C_1(t)|^2$, i.e. $-(g_o/4\omega) \text{Sin}(g_o t) \text{Sin}(2\omega t + 2\phi)$, which is first order in $g_o/4\omega$, is plotted in Fig.2(b). These analytical results agree very closely (within the order of $g_o/4\omega$) to the results which are obtained via direct numerical integration of Eq.7 and plotted in Fig.2 (a') and 2(b').

Further we numerically calculate the population variation of the excited state with the initial phase of the electromagnetic field, keeping all other parameters as fixed. In Fig.3 we plot $|C_1(t)|^2$ vs. ϕ , for $g_0=1$ and $g_0/\omega=.01$, switching time $\tau_{switch}=.01$ and the total passage time τ corresponding to a time such that $t g_0 = \pi/2 - .01$. This oscillation is expected to be measured in a real experiment as we have described.

A physical realization of the population $|C_1(t)|^2$ oscillation with the initial phase can be measured experimentally by using 2-level Rb atoms (or semiconductor quantum dots) in a driving magnetic field. The states of the Rb atoms to be considered as $|0\rangle$ and $|1\rangle$ have been already discussed. A schematic sketch has been shown in Fig.1. Initially Rb atoms (with Maxwell-Boltzman (MB) distribution) are fired from a thermal gun and are pass through the strong periodic magnetic field for a total time τ . Due to the real time evolution, the dynamical phase evolves, and then one may wonder that the atoms coming from the oven have a MB distribution of the velocity, therefore, the phase information may be randomized, or lost due to the random passage of the atoms through the magnetic field. But it can be shown easily that all atoms start with different velocities will not effect the value of $|C_1(\tau, g_0, \phi)|^2$, provided the atoms are measured immediately after they leave the magnetic field. This is an important point from the experimental aspect to perform this experiment with rubidium atoms.

In conclusions, we have shown that, when a Rabi oscillation in a two-level atomic system is driven by a strong periodic field, the amplitude modulation of the Rabi intensity has the information/finger-print of the initial phase of the driving field. Considering Rabi oscillation of a two level hot Rubidium atoms driven by a strong magnetic field, a real life experimental realization to measure the phase has been described. The interesting point to be noted here that, measuring the population only of the excited state, one can measure the phase. It is also clear that, in the presence of a strong driving field there is an extra oscillation/modulation of the order of $(g_0/4\omega)$ over the main Rabi flopping $\text{Sin}(g_0 t/2)$, and this oscillation forbids a spin to jump to an excited state with an unit probability, and for $\tau = m\pi/\omega$ matching has to be satisfied to flop with an unit probability.

This work was supported by AFOSR grant # F49620-98-1-0313, ARO grant # DAAG55-98-1-0375, and NRO grant # NRO-000-00-C-0158.

References:

1. R. Jozsa, D.S. Abrams, J.P. Dowling, and C.P. Williams, *Phys. Rev. Letts.* **85**, 2010(2000).
2. S.Lloyd, M.S. Shahriar, and P.R. Hemmer, *quant-ph/0003147*.
3. G.S. Levy et al., *Acta Astronaut.* **15**, 481(1987).
4. E.A. Burt, C.R. Ekstrom, and T.B. Swanson, *quant-ph/0007030*
5. National Research Council Staff, *The Global Positioning System: A Shared National Asset*, National Academy Press, Washington, D.C., 1995.
6. A. Corney, *Atomic and Laser Spectroscopy*, Oxford University Press, 1977.
7. L. Allen and J. Eberly, *Optical Resonance and Two Level Atoms*, Wiley, 1975.
8. F. Bloch and A.J.F. Siegert, *Phys. Rev.* **57**, 522(1940).
9. J. H. Shirley, *Phys. Rev.* **138**, 8979 (1965).
10. S. Stenholm, *J. Phys. B* **6**, (August, 1973).
11. J.E. Thomas et al., *Phys. Rev. Lett.* **48**, 867(1982).
12. P.R. Hemmer, M.S. Shahriar, V. Natoli, and S. Ezekiel, *J. of the Opt. Soc. of Am. B*, **6**, 1519(1989).
13. M.S. Shahriar and P.R. Hemmer, *Phys. Rev. Lett.* **65**, 1865(1990).
14. M.S. Shahriar et al., *Phys. Rev. A* **55**, 2272 (1997)

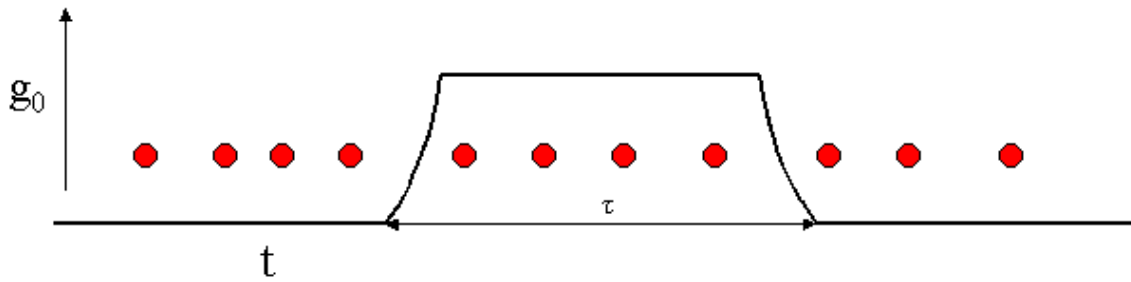


Fig.1 : Schematic picture of an experimental realization of the phase of the field. Thermal Rubidium atoms are passing through the magnetic field of saturation strength g_0 , switching time τ_{switch} , and for total passage time τ .

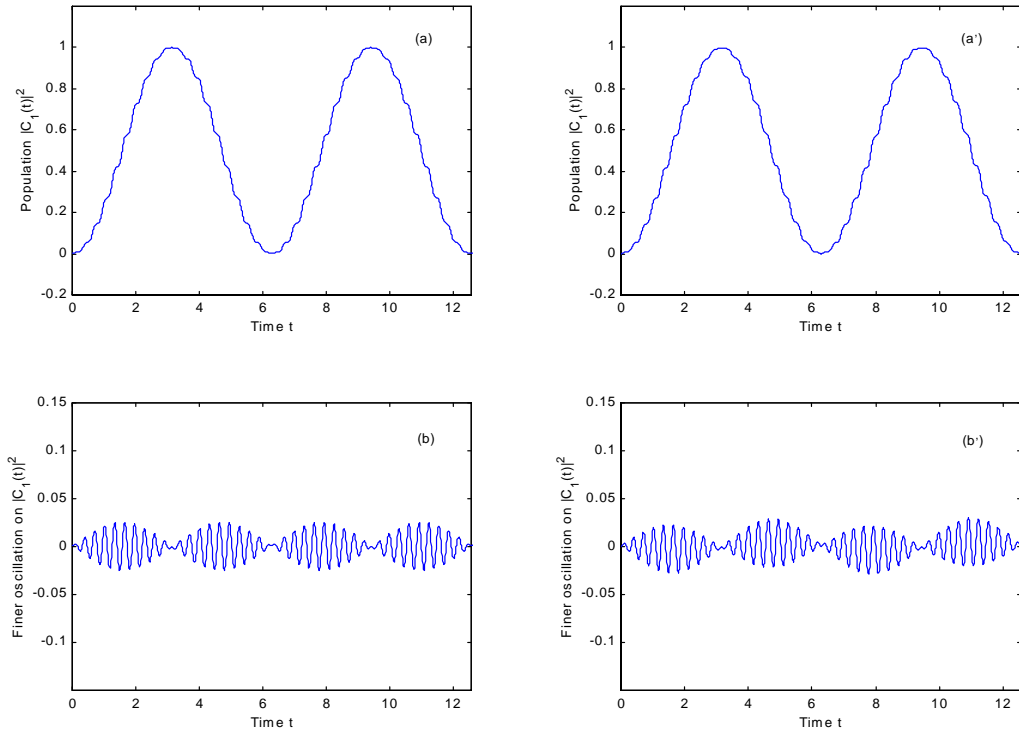


Figure 2 . (a) Analytical total excited state population $|C_1(t)|^2$ vs t plot, for $g_0=1$ and $g_0/\omega=.01$. (b) Plot of the finer oscillation part (order of $g_0/\omega=.1$) which is present within the $|C_1(t)|^2$, this oscillation one gets after subtracting the plain Rabi flopping term $\text{Sin}(g_0 t/2)$ from the total population $|C_1(t)|^2$. (a') and (b') plots are for the numerical integration of the Eq.7 and are similar to 2.(a) and (b) respectively.

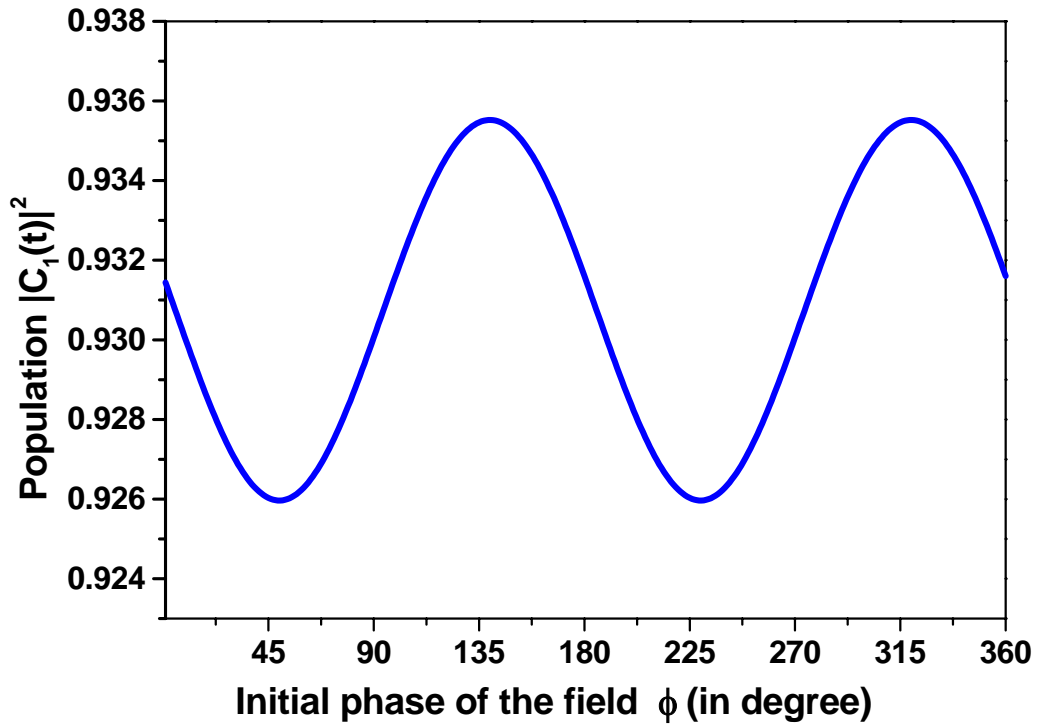


Figure 3. The numerically calculated intensity $|C_1(t)|^2$ versus initial phase ϕ plot for a fixed $t=\tau$, where τ is the time corresponding to $t g_0 = \pi/2 - .01$, $\tau_{switch} = .01$ and $g_0 = 1$. The oscillation is of the order of $g_0/4\omega$. We expect that this oscillation can be measured experimentally as describe in the main text, and hence the initial phase of the Rabi driving field can be measured.

4. Quantum Teleportation of an Atomic State: Theoretical Studies

We have proposed a scheme for creating and storing quantum entanglement over long distances. Optical cavities that store this long-distance entanglement in atoms could then function as nodes of a quantum network, in which quantum information is teleported from cavity to cavity. The teleportation is conducted unconditionally via measurements of all four Bell states, using a novel method of sequential elimination.

This work has been published in the *Physical Review Letters*. For details, see:

“Long Distance, Unconditional Teleportation of Atomic States via Complete Bell State Measurements,” S. Lloyd, M.S. Shahriar, J.H. Shapiro, and P.R. Hemmer, *Phys. Rev. Lett.* **87**, 167903 (2001).

5. Experimental Progress Towards Quantum Teleportation of an Atomic State

We have been pursuing the realization of quantum teleportation of the state of a massive particle: namely a single rubidium atom. Here we summarize the experimental progress made in this regard.

5.1 High-Finesse Cavity

1.a. Construction and Test of the Cavity

We have constructed a high finesse cavity using super-mirrors obtained from Research Electro-optics of Boulder, CO. Here are the parameters of the cavity: Mirror radius of curvature: 10 cm; Mirror reflectivity: 99.998%.

The housing for the cavity, along with a typical spectrum observed in this cavity, with a mirror separation of about 50 μm , is illustrated below in figure 1. The observed finesse is about 6×10^4 .

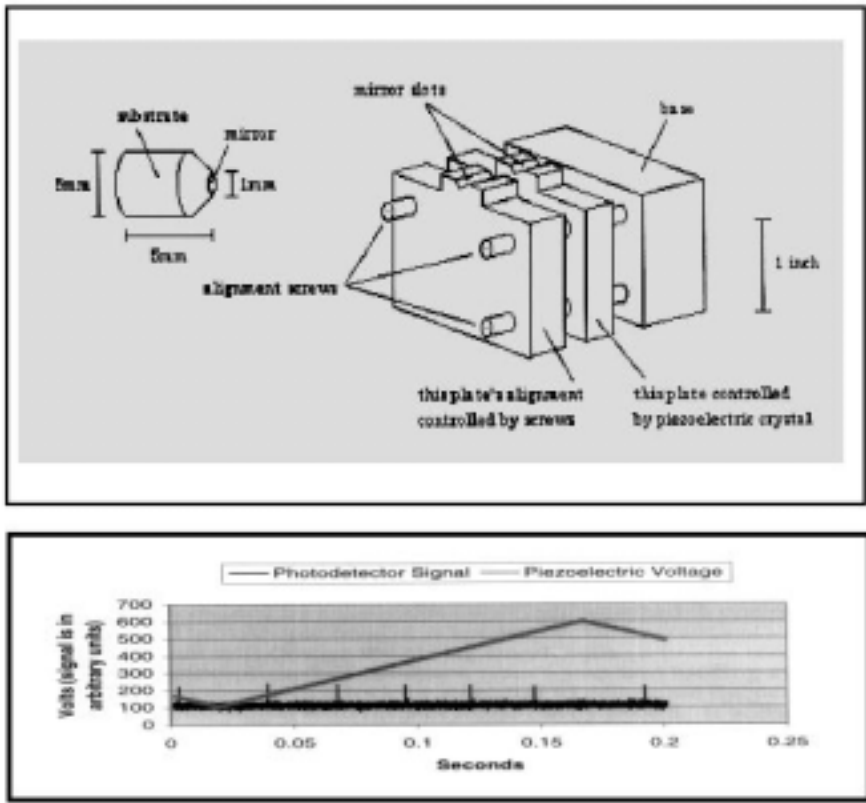


Figure 1: Top: Schematic illustration of the cavity mount. Bottom: A typical set of resonances observed in a cavity with a mirror separation of $50 \mu\text{m}$.

1.b. Cavity Stabilization via Electro-Optic Modulation

We used a high-voltage ($V_{\pi} \sim 300$ V) electro-optic modulator at 18 MHz to generate sidebands on the cavity resonances. Using the Pound-Drever-Hall technique where the error signal is generated from the signal reflected from the cavity, we stabilized the cavity to the Ti-Sapphire laser frequency. This result is preliminary; more detailed analysis on parameters such as servo bandwidth and residual frequency noise would be performed later when the cavity is mounted in a vibration isolated structure (in its functional configuration, the cavity would be mounted on an RTV rubber pad, which in turn would be situated on a heavy copper block). The laser frequency in turn was locked to an atomic transition in rubidium using a saturated absorption cell.

The over-all setup is illustrated below in figure 2.

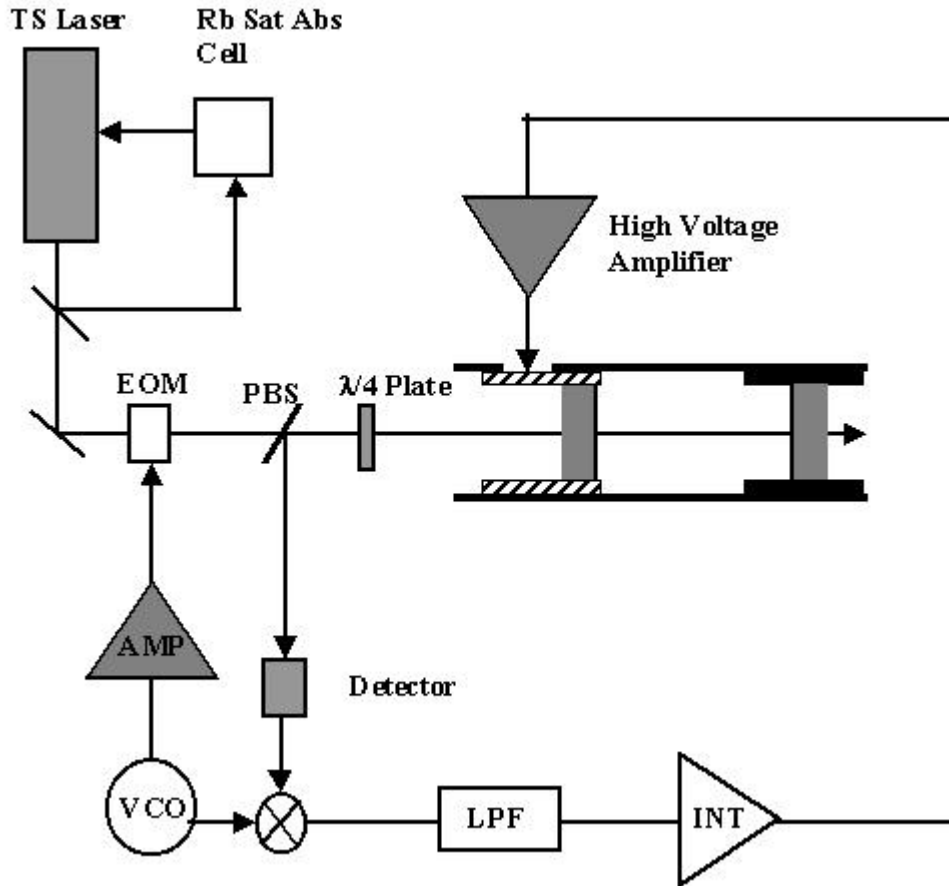


Figure 2: Schematic illustration of the over-all configuration for cavity stabilization.

4.2 Magneto-Optic Trap Designed For Quantum Memory

We have constructed a magneto-optic trap with extra ports and structures designed specifically for realizing quantum memory elements. The complete system consists of three inter-connected vacuum chambers, a scanning diode laser, and three Ti-Sapphire lasers pumped by two Argon lasers.

The whole process starts with solid rubidium, which is heated to produce an atomic vapor in the oven section. A pair of apertures are used to extract a collimated atomic beam, with a mean velocity of about 400 m/sec, which in turn is slowed down via chirped cooling, using a scanning diode laser. A novel electronic design was employed to ensure that the starting and stopping frequencies are fixed with respect to an atomic transition. A repump beam generated from one of the Ti-Sapphire lasers (TS-2) is used to prevent optical pumping during the cooling process. The atomic beam is about 1 cm above the center of the main trap chamber; the diode laser slows the atoms down to about 20 m/sec, which fall ballistically into the center of the chamber. Three pairs of orthogonal, counter-propagating laser beams generated from another Ti-Sapphire laser (TS-1) intersect at this center. A quadrupolar magnetic field gradient is also generated at the center, using a pair of water-cooled anti-Helmholtz coils. A repump beam from first Ti-Sapphire laser (TS-2) is also present again to prevent optical pumping. Using this geometry, we are able to trap routinely about 10^7 atoms in a volume of about 2 mm^3 .

We have added a third vacuum chamber above the main one in order to house the high-finesse cavity, the center of which will be colocated with the FORT (Far Off-Resonant Trap) beam. The FORT beam is currently generated from the third Ti-Sapphire laser (TS-3), tuned to 805 nm. The FORT has a power of about 500 mW, and is focused to a spot with a waist size of about $10 \mu\text{m}$. This is the biggest spot size that can be produced at the center of a cavity with a mirror separation of $50 \mu\text{m}$, which in turn is chosen to produce a vacuum Rabi frequency much stronger than the atomic decay rate. (In the future, we plan to consider a different combination where the mirror separation is increased to enhance the cavity photon life-time. At that point, we would be able to use a CO_2 laser for the FORT, which is expected to produce less residual heating).

Finally, a launching beam, derived from one of the Ti-Sapphire laser (TS-1) is positioned vertically, in order to launch the atomic fountain, as described in the next section.

All the laser beams are controlled by acousto-optic modulators, and are produced in the proper timing sequence generated from an arbitrary wave-form generator.

The main trap chamber as well the top chamber is maintained at a vacuum of about 1.3×10^{-11} Torr using a 200 liter/sec ion pump. This is the best level of vacuum one can produce without resorting to cryogenic means. Such a vacuum is expected to be good enough to ensure a background-collision-limited quantum memory lifetime of more than 2 minutes. (Of course, residual fluctuations of magnetic fields may limit the lifetime to a shorter duration). The top chamber can be isolated from the rest in order to place and align the cavity as necessary, without affecting the main chamber.

The over-all system is illustrated schemtically below in figure 3.

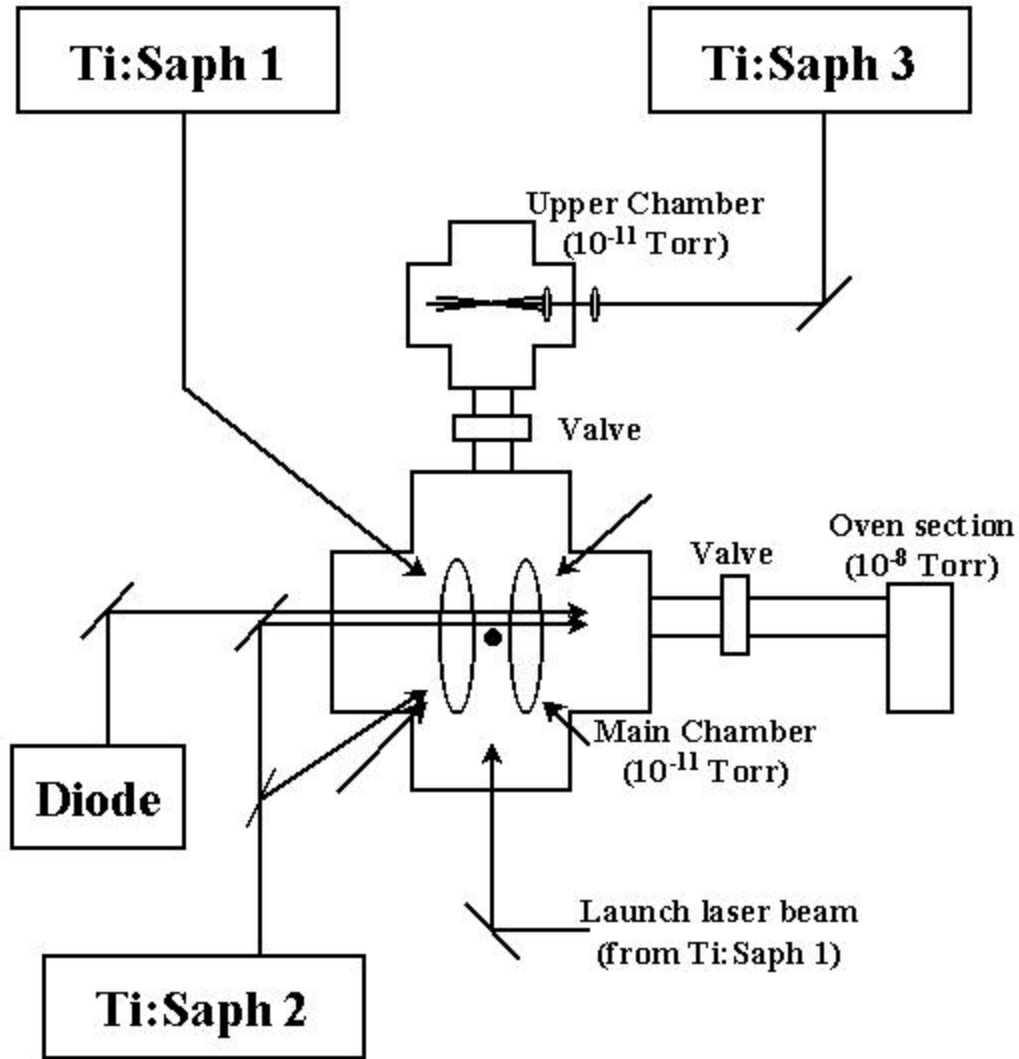


Figure 3: Schematic illustration of the three-part chamber implemented for realizing quantum memory.

4.3 Demonstration Of Atomic Fountain

Using the arrangement shown in figure 3, we have demonstrated an atomic fountain, where the atoms are launched vertically from the magneto-optic trap (MOT). Before we present his result, it is instructive to outline our scheme for loading the quantum memory using an atomic fountain, as outlined in figure 4 below.

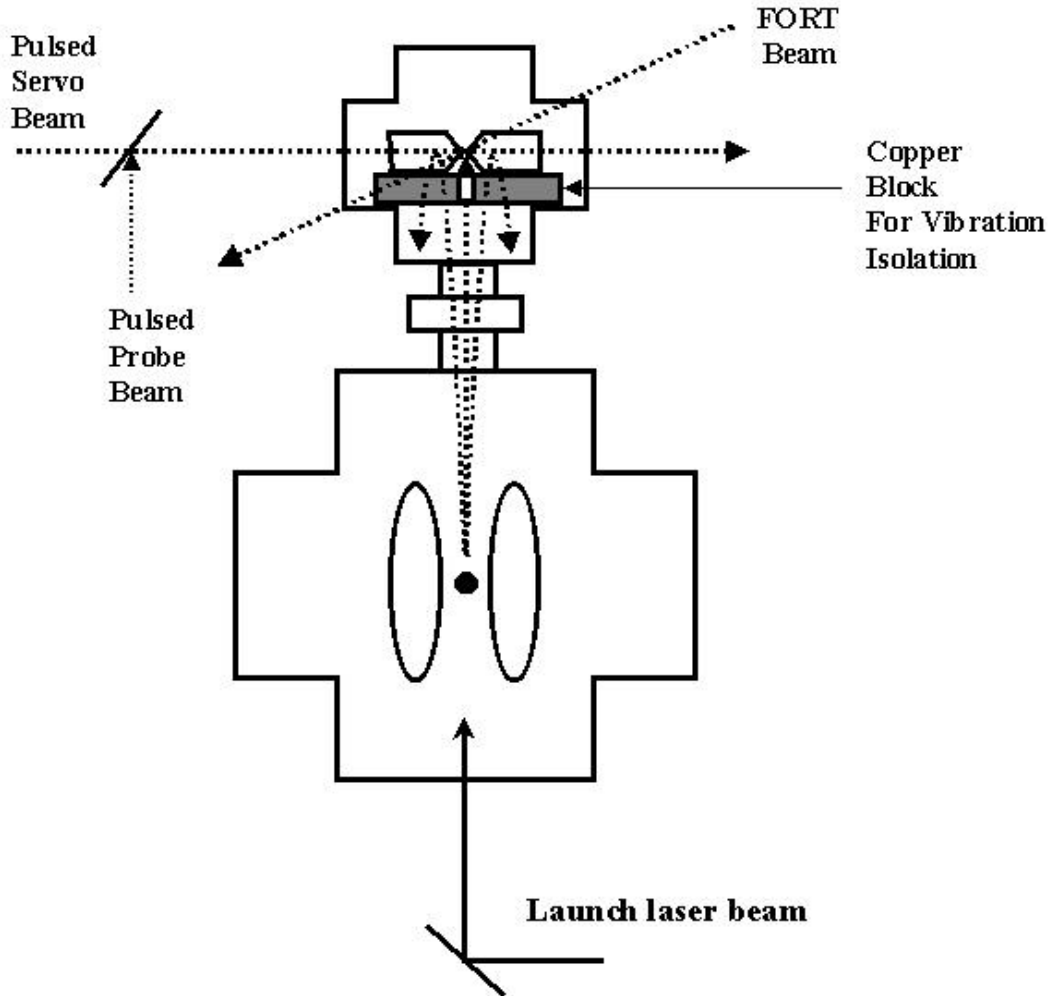


Figure 4: Schematic illustration of the planned geometry for loading the quantum memory using an atomic fountain.

Briefly, the launching velocity is chosen --- by adjusting the intensity of the launch beam --- to be such that the atoms would come to a stop at the center of the cavity. The FORT beam is turned on just at this instant; this is necessary because of the fact that the FORT potential is fully conservative. Initially, we expect to trap the maximum number of atoms possible (about 200) in the FORT, in order to facilitate detection and optimization. Afterwards, the initial number of atoms caught in the magneto-optic trap will be reduced (e.g., by reducing the intensity of the trapping beams in the central chamber) to one. The number of atoms in the FORT will be detected by monitoring variations in the transmission of a probe beam through the cavity. This technique has been demonstrated by Kimble's group to be sensitive enough to detect single atoms.

Our approach is to first demonstrate and optimize the catching of a few atoms with the FORT prior to installing the cavity in the chamber. This is potentially easier to do, by detecting the atoms via fluorescence.

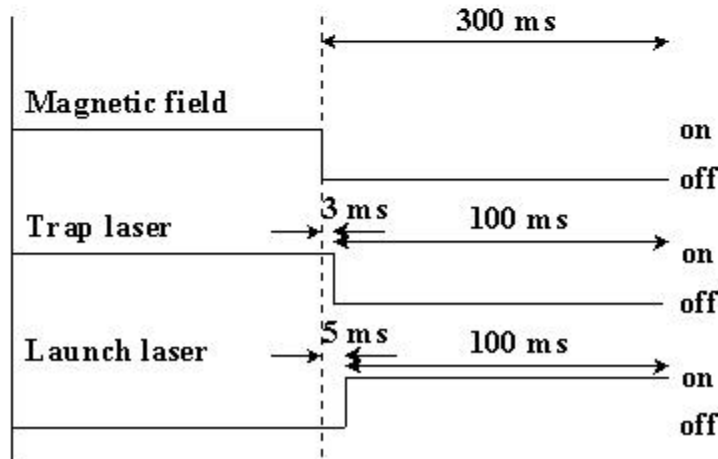
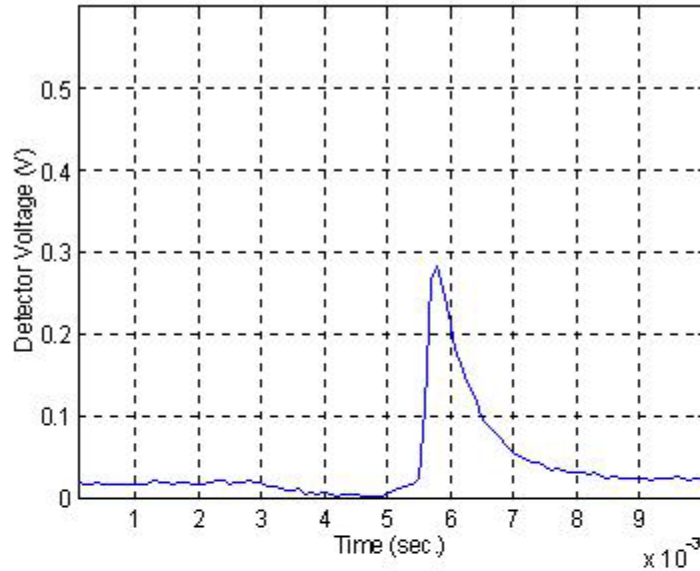


Figure 5. Time-of-flight fluorescence signal observed 1 cm above the MOT, as evidence of the atomic fountain.

The basic step in this process is to demonstrate the atomic fountain. To this end, we employed a simplified geometry, wherein a probe is placed only a cm above the MOT. A silicon photo-diode is used to observe the fluorescence time-of-flight signal. Figure 5 shows a typical signal observed using this geometry. The timing sequence for observing this signal is as follows. After the MOT has been loaded, the magnetic field is turned off. This time coincides with the origin of time in the time-of-flight (TOF) signal. The trap laser beams (for the MOT) are turned-off 3 msec later. After another 2 msec, the launching laser beam is turned on. As can be seen from the TOF signal, the peak of the observed fluorescence occurs 0.8 msec after the launch. This implies a launch velocity of about 12 m/sec. This is much faster than what is needed to ensure that the atoms come to a stop at the center of the top chamber, which is at a height of 30 cm above the MOT. Since the launch velocity can be reduced easily by lowering the intensity of the launch beam, this demonstrates our ability to produce the desired fountain.

4.4. Indirect And Direct Observation Of Trapping Atoms In The Fort

As shown in figure 4, our eventual objective is to trap the atoms using the FORT beam at the upper chamber. However, the number of atoms caught are supposed to be too small to detect easily, especially if the FORT parameters are not optimized. As such, we decided to tune up the FORT first by doing a simpler test, wherein the FORT is applied directly to the MOT, as shown in figure 6. The fluorescence produced by a resonant probe beam is collected by a large lens, onto a cooled PMT.

Indirect Observation of the FORT:

In order to detect the effect of the FORT beam, the experiment is run first with the FORT turned off. The MOT is turned off, and a sufficient period of time, T , is allowed to elapse to ensure that virtually no signal is detected. The experiment is now repeated with the FORT, and the fluorescence is detected again after the time T . Presence of a bigger signal now indicates that some atoms remained trapped in the FORT. Figure 7 shows a signal observed this way. This data is very preliminary, and further optimization of the FORT parameter (e.g., spot size, power, location, etc.) have to be optimized in order to increase the signal to noise ratio.

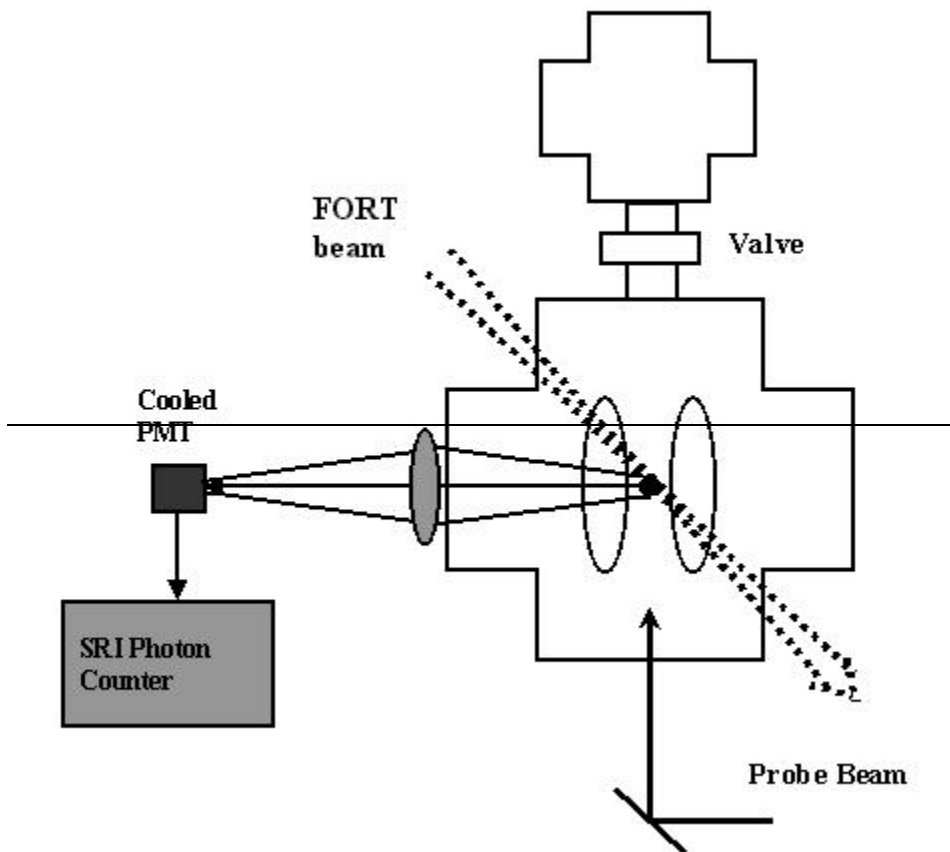


Figure 6: Schematic illustration of the simplified geometry for observing atoms trapped by the FORT beam

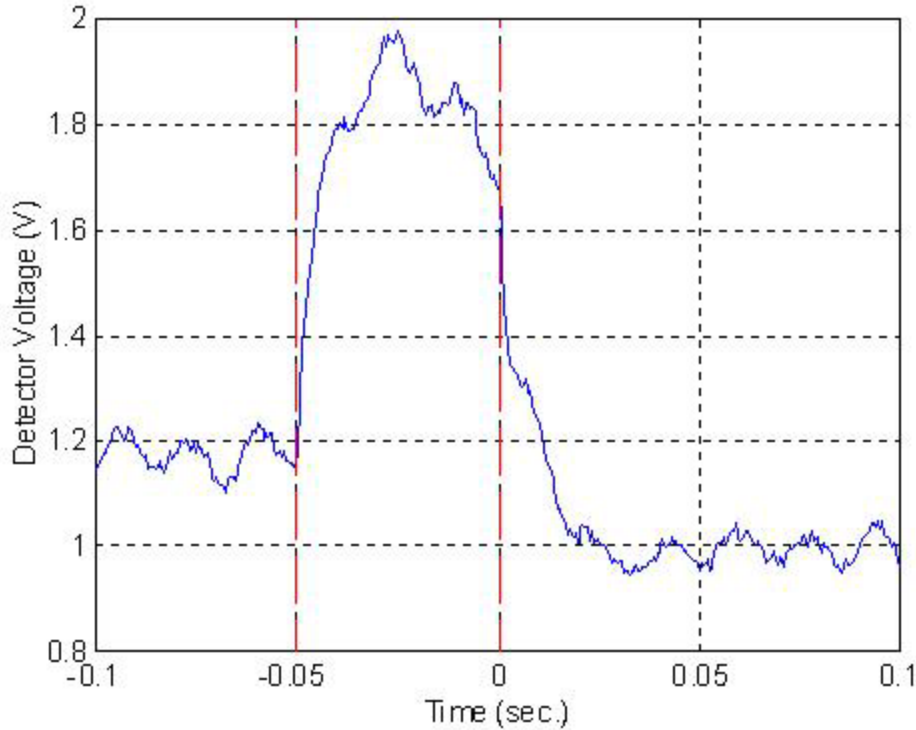


Figure 7: Preliminary evidence of atoms caught by a FORT co-located with the MOT. See text for details.

Direct Observation of the FORT:

The evidence of the FORT gathered using the method described above is indirect, and sometimes suffer from the limitation that the difference between the signal observed when the FORT is on and the one observed when the FORT is off becomes very small for some parameters. Furthermore, since the observed signal is integrated over the volume, it is difficult to align the FORT beam and optimize its size and shape.

In order to eliminate these constraints, we have augmented our observation apparatus by adding an image-intensifier camera we obtained from Roper Scientific. This enabled us to observe the atomic density distribution directly with a spatial and temporal resolution high enough to monitor the FORT directly.

Figure 8 shows the atoms confined by the FORT, seen as the horizontal line superimposed on the atoms caught by the MOT alone. Here, the frequency of the FORT laser is 782.1 nm, and the signal is captured 10 msecs after the MOT beams are turned off. The FORT beam is kept “on” during the formation of the MOT, as well as after the MOT beams are turned off. Figure 9 show the horizontal profile of the atomic density distribution, determined by integrating the signal of figure 8 in the vertical direction. The slightly broader pedestal (note the sudden change in slope at around 32 and 18 on the arbitrary-unit horizontal scale) is due to the fact that the atoms caught in the fort are spread over a horizontal extent longer than that of the atoms caught by the MOT alone (as evident from figure 8). Figure shows the vertical profile of the atomic density distribution, determined by integrating the signal of figure 8 in the horizontal direction. The anomalous peak corresponds to the higher density of atoms at the location of the FORT beam. On this graph, the vertical position is decreasing in height as we move from left to right.

The observation is repeated another 10 msec later (i.e., altogether 20 msec after the MOT is turned off). Figures 11, 12 and 13 show the corresponding two-dimensional density map, the integrated horizontal profile, and the integrated vertical profile. As can be seen, especially by comparing figure 10 to figure 13, the atoms caught in the FORT are staying unchanged in the vertical position, while the remaining atoms are falling under gravity.

While the method of observation is now clearly good enough for rapid optimization of the FORT parameters, the performance of our FORT itself was less than satisfactory, primarily because of the low power and lack of frequency stability of the Ti-Sapphire laser (a laser manufactured by LSDI, Inc., without any external cavity for frequency stabilization, and an available power of about 200 mW) used as the FORT beam. Much better performance is expected if we use one of our other two Ti-Sapphire lasers (Coherent 899, fully frequency stabilized, with an available power of 2 W). However, one of these Coherent lasers is being used for the MOT beams, while the other is being used for the repump beam (with a diode laser providing the chirp-slowing beam). Because of the lack of frequency stability of the LSDI laser, it is not readily possible to swap the role of this with either of the Coherent lasers. In order to circumvent this problem, we have installed two high-frequency, high-efficiency acousto-optic modulators in a serial configuration in order to generate both the MOT beams and the repump beams from the same Coherent laser. While the repump power generated this way is far less than what we were using before, we have found that we can still get the MOT to work, with only about a factor of two drop in the number of atoms caught. On the other hand, we now have the other Coherent laser freed up for use as the FORT beam.

The whole experiment had to be interrupted at this point due to the move of Dr. Shahriar to the Northwestern University. As soon as the apparatus is transported and re-assembled, we expect to optimize the FORT using the higher power laser, and move on to realizing the scheme shown in figure 4.

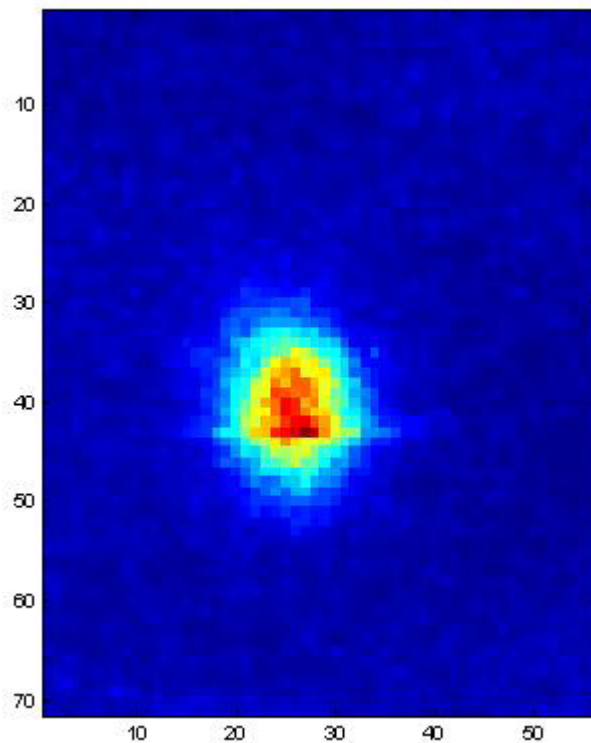


Figure 8: Direct observation of the atoms confined by the FORT, seen as the horizontal line superimposed on the atoms caught by the MOT alone. Here, the frequency of the FORT laser is 782.1 nm, and the signal is captured 10 msec after the MOT beams are turned off. The FORT

beam is kept “on” during the formation of the MOT, as well as after the MOT beams are turned off.

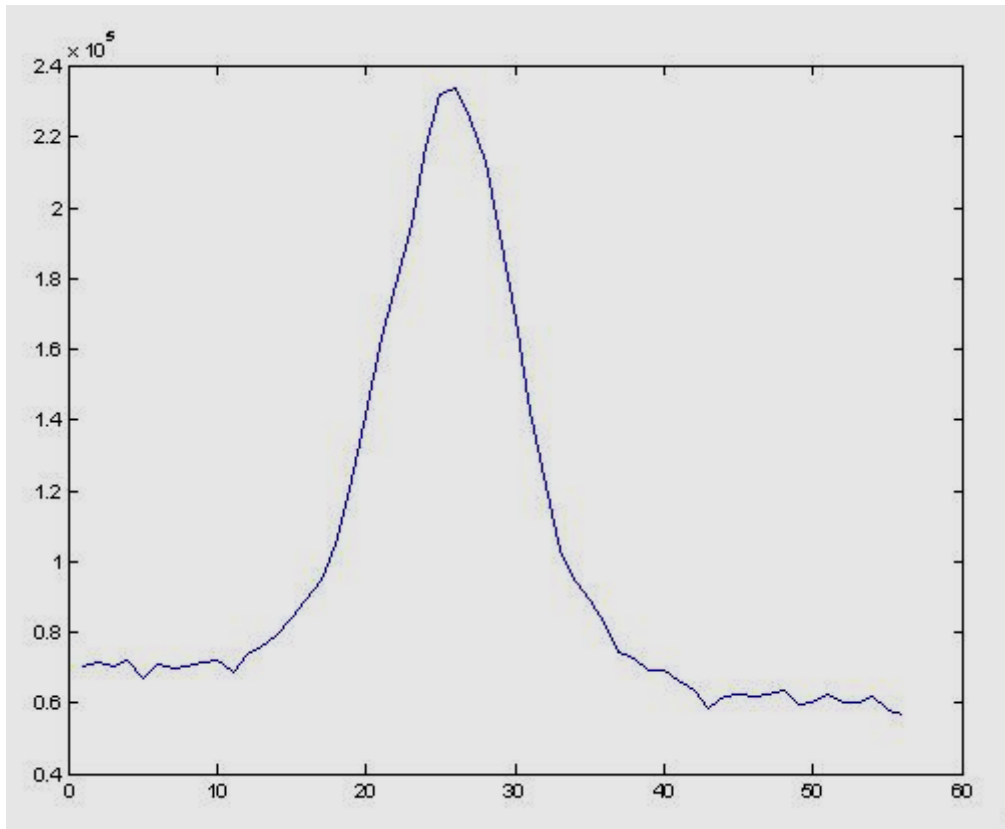


Figure 9: Horizontal profile of the atomic density distribution, determined by integrating the signal of figure 8 in the vertical direction. The slightly broader pedestal (note the sudden change in slope at around 32 and 18 on the arbitrary-unit horizontal scale) is due to the fact that the atoms caught in the fort are spread over a horizontal extent longer than that of the atoms caught by the MOT alone (as evident from figure 8).

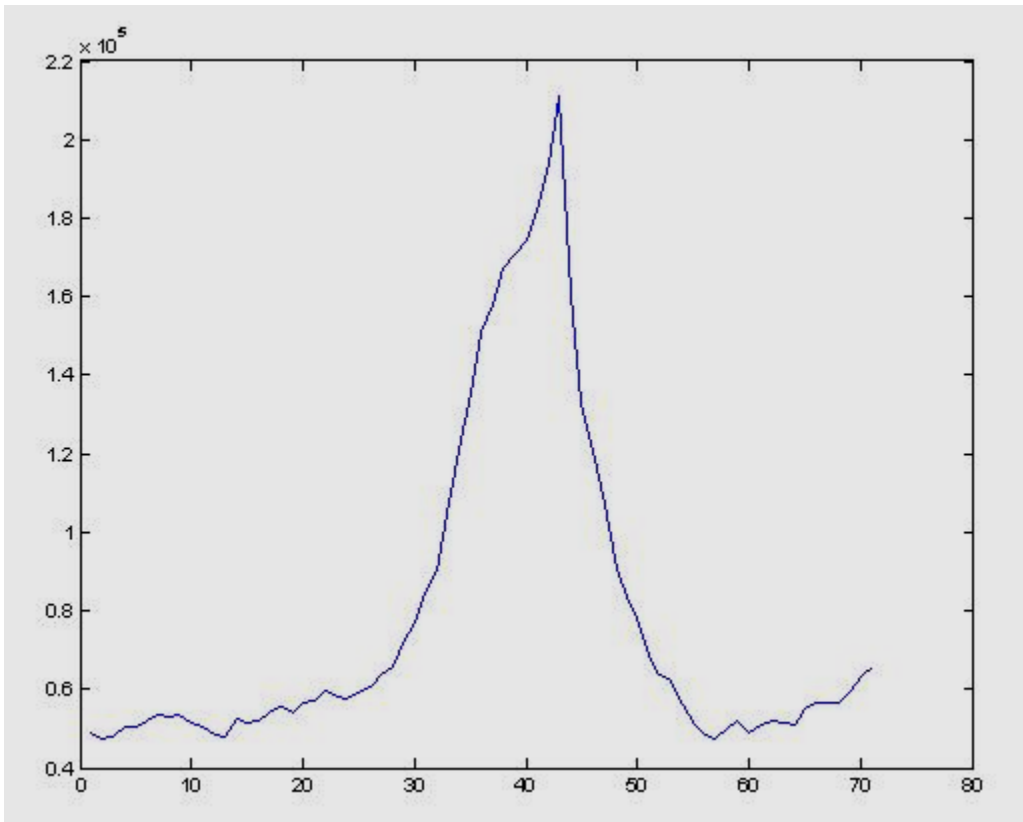


Figure 10: Vertical profile of the atomic density distribution, determined by integrating the signal of figure 8 in the horizontal direction. The anomalous peak corresponds to the higher density of atoms at the location of the FORT beam. The vertical position is decreasing in height as we move from left to right in this graph.

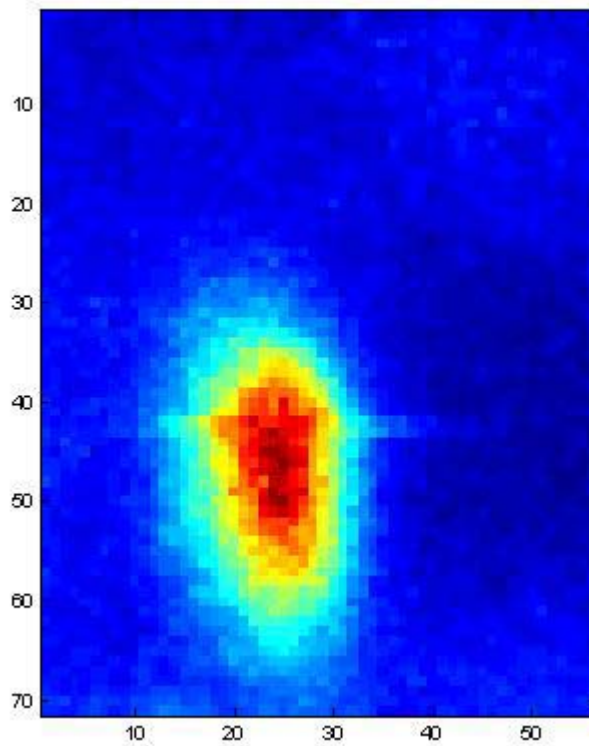


Figure 11: The density distribution of the signal shown in figure 8, captured another 10 msec later (i.e., altogether 20 msec after the MOT is turned off). Careful comparison of the vertical axes of this picture and the picture in figure 8 shows that the line of atoms caught in the FORT has remained virtually unchanged in its vertical position (around 43 on the arbitrary-unit scale). At the same time, the MOT atoms have dropped vertically under gravity, while expanding due to the residual velocity spread.

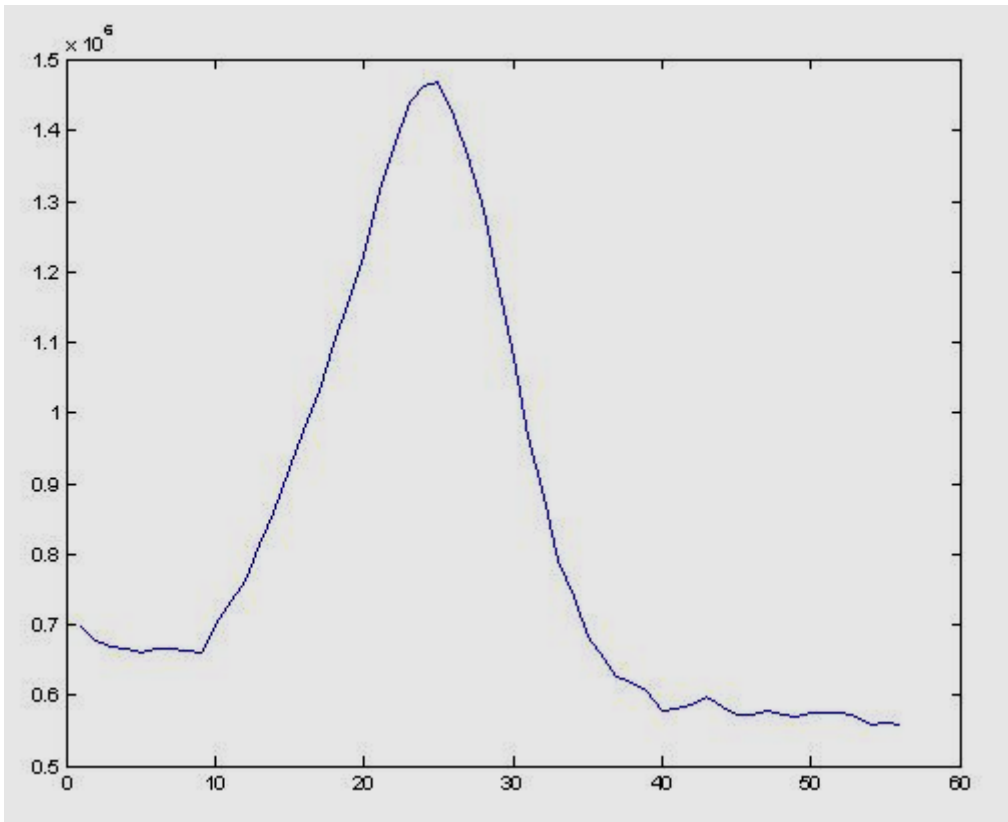


Figure 12: Horizontal profile of the atomic density distribution, determined by integrating the signal of figure 11 in the vertical direction. Note that the broader pedestal pedestal of the type seen in figure 9 has virtually disappeared here, due to the fact that the MOT cloud is expanding faster (given that the MOT is turned off now) than the atoms in the FORT.

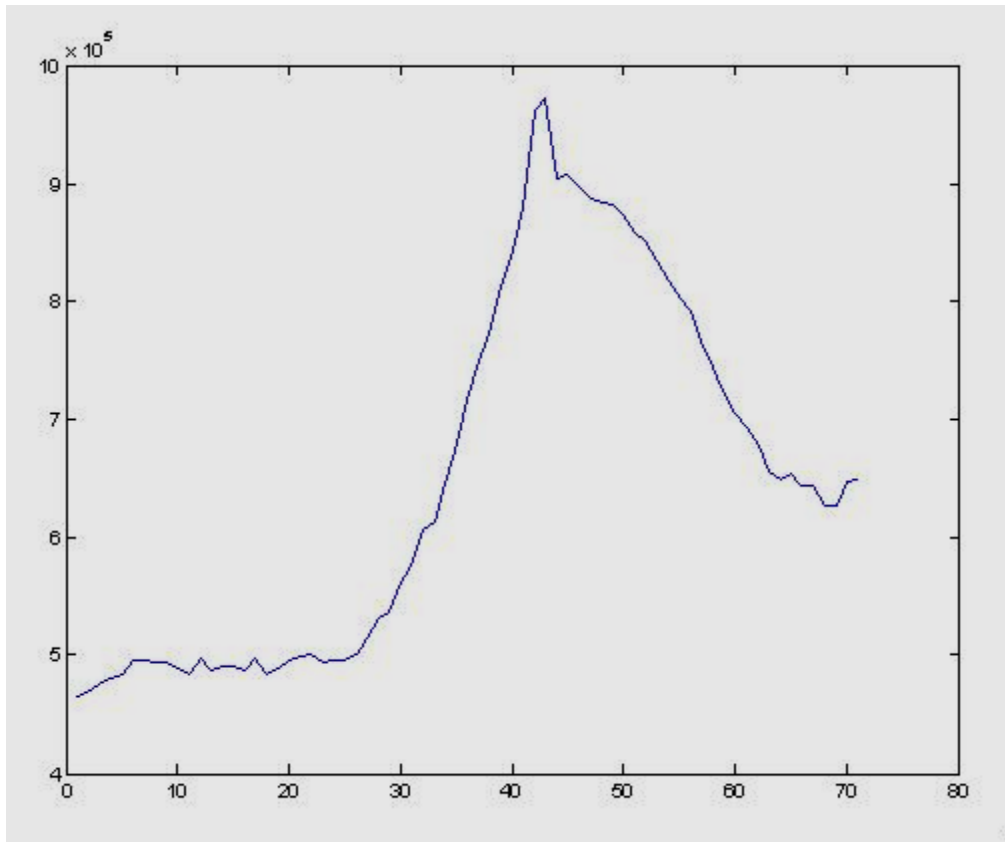


Figure 13: Vertical profile of the atomic density distribution, determined by integrating the signal of figure 11 in the horizontal direction. Again, the anomalous peak corresponds to the higher density of atoms at the location of the FORT beam. The vertical position is decreasing in height as we move from left to right in this graph.

Comparison with figure 9 again shows clearly that the atoms in the FORT are staying unchanged in the vertical position, while the MOT atoms are dropping under gravity.

6. Slowing and Stopping of Light Pulses in a Solid

We have reported ultraslow group velocities of light in an optically dense crystal of Pr doped Y₂SiO₅. Light speeds as slow as 45 m/s were observed, corresponding to a group delay of 66 ms. Deceleration and “stopping” or trapping of the light pulse was also observed. These reductions of the group velocity are accomplished by using a sharp spectral feature in absorption and dispersion that is produced by resonance Raman excitation of a ground-state spin coherence.

This work has been published in the Physical Review Letters. For details, see:

“Observation of Ultraslow and Stored Light Pulses in a Solid,” A. V. Turukhin, V.S. Sudarshanam, M.S. Shahriar, J.A. Musser, B.S. Ham, and P.R. Hemmer, *Phys. Rev. Lett.* **88**, 023602 (2002).

7. Reference-Locked Frequency Chirping of a Diode Laser for Slowing Atoms

Cooling and trapping of atoms [1] is of considerable current interest. In laser cooling experiments atoms scatter resonant photons from a laser beam directed against the velocity of the atomic beam. The transfer of photon momentum to the atom eventually brings the atom to rest. The primary experimental difficulty in such atom-slowing techniques is the varying Doppler shift experienced by the atom as it slows down. The change in the Doppler shift takes the atom out of resonance with the laser field. Therefore, to keep the atom in resonance with the applied field as it slows down, either the atomic or the laser frequency needs to be smoothly and accurately varied. The technique based on varying the atomic frequency is called Zeeman cooling [2], while the corresponding technique based on varying the laser frequency is called chirp cooling [3-6]. In the both techniques the laser is tuned below the zero-velocity resonance frequency of the moving atom. As the atom slows, the Doppler shifts decrease, and therefore, to keep the atom in resonance, the laser frequency must increase. This is achieved by sweeping (or chirping) the laser frequency as a function of time at a rate equal to the ratio of the Doppler shift at the most probable velocity of the incoming atom to the total stopping time for the atom. To chirp cool the atoms, diode lasers are preferred, not only because of their compactness and low cost [7-9], but also because chirp is easier to achieve with diode lasers. Diode lasers, however, suffer from the frequency drift caused by changes in the junction temperature, by current noise and by the perturbation of the external cavity length. This drift will cause drifting of the chirp, which results in inefficient cooling. Furthermore, it will cause drifting of the end points of the chirp, leading to fluctuations in the final velocity profile of the atomic beam.

This problem can be overcome by using, for example, an acousto-optic modulator (AOM). Briefly, the diode laser frequency is shifted by the AOM, and then locked to an atomic transition using standard methods [10-13]. The AOM driving frequency is then scanned in order to produce the required chirping. One drawback of this approach is that the direction of the output of an AOM is correlated with the driving frequency, so that the scan is accompanied by undesired angular variations. One can overcome this problem by using a compensating, scanning mirror. However, in order for this process to work well, the scan range should be a small fraction of the base frequency. Given that the scan range is typically a few hundred MHz, this implies that the AOM to be used should have a base frequency in the GHz range. An AOM at such a high frequency is generally expensive, and not very efficient. As such, only a small fraction of the total diode laser power is available for chirp cooling. Here, we demonstrate an alternative method that

does not require an AOM, and makes most of the diode laser power available for cooling. It is simple, robust, and requires only inexpensive electronics.

In our experimental setup shown in Fig. 1 the atomic beam consists of rubidium atoms which effuse from a small hole in an oven operating at $\approx 250^\circ\text{C}$. This atomic beam is collimated and is finally directed into a vacuum chamber evacuated to about 10^{-10} Torr. The most probable velocity of the ^{85}Rb atoms in the atomic beam is ≈ 320 m/sec which corresponds to the Doppler shift of ≈ 680 MHz. To chirp cool the atoms in this atomic beam we use a commercially adopted version (Tui Optics: DL 100) of the extended-cavity diode laser described earlier by Hansch and co-workers [8]. This system uses a solitary Hitachi laser diode (HL 7857 G) which operates near 780 nm. When free running, this laser operates in multimode with broad bandwidth. In this laser system, external feedback to the laser diode provided by a grating in the Littrow configuration forces the laser to operate in single mode with a linewidth of about 1 MHz [9]. The coarse tuning of the laser output wavelength is achieved by changing the junction temperature and the injection current of the laser diode, while the fine tuning is achieved by changing the tilt angle of the diffraction grating with a piezo actuator. This diode laser beam is overlapped with a second repump laser beam. The two superimposed beams are circularly polarized and focused inside the vacuum chamber, where they overlap and propagate counter to the atomic beam. Inside the vacuum chamber there is about 10 mW of diode laser power with a beam diameter of 5 mm, and about 75 mW of repump laser power with a beam diameter of 1 cm.

As shown in Fig. 2, the diode laser is tuned to the $5S_{1/2}(F=3) \rightarrow 5P_{3/2}(F'=4)$ transition of the ^{85}Rb atom. The diode laser beam decelerates the ^{85}Rb atoms, which are finally brought to rest. The total stopping distance in our experiment is about one meter. The function of the repump beam is to prevent the optical pumping of the atoms into the lower hyperfine level $5S_{1/2}(F=2)$ of the ground state (Fig. 2) [4,14].

A block diagram of the locking circuit is shown in Fig. 3. The diode laser frequency is swept by a voltage ramp from the laser controller, which is also applied to the grating drive mechanism of the diode laser. The sweeps are short so that the sweep time (≈ 1 ms) is smaller than the frequency drift time. The absorption spectrum was monitored with a photodiode through a cell containing rubidium atoms. This spectrum was recorded at room temperature at which the Doppler width for rubidium atom is *****. The signal from the photodiode is differentiated electronically. The differentiated signal is then multiplied by the output of the pulse generator, which generates TTL pulses with adjustable time delay. The output of the multiplier is fed to an integrator. The integrated output is the feedback signal, which is added to the ramp voltage that drives the grating to sweep the laser frequency.

To lock the sweeping laser frequency, the time delay of the pulse from the pulse generator is adjusted so that the pulse coincides with the zero-crossing point of the differentiated signal (Fig. 4). Under this condition the error signal is zero. Any drift in the laser output frequency results in an offset between the pulse from the pulse generator and the zero-crossing point of the differentiated signal. This results in a nonzero value of the error signal, whose magnitude and sign are determined by that of the offset. Fig. 5 shows the schematic of the actual circuit. The complete circuit consists of four essential parts viz. (1) differentiator (2) timer (3) integrator (4) adder.

Fig. 6 shows a typical signal as experimentally observed through the absorption cell containing ^{85}Rb atoms. This signal was observed using the ramp voltage shown in Fig. 6 (a). Fig. 6(c) shows the output of the differentiator when the signal shown in Fig. 6(a) was supplied to its input. In Fig. 6 the peak position of the signal and the zero-crossing point of the differentiated signal are coincident with the pulse from the pulse generator shown in Fig 6(d). Some kinks in Fig. 6(b) and (c) are due to the presence of the neighboring hyperfine transitions shown in Fig. 2, which lies within the Doppler envelope and complicates the interpretation of the observed spectrums.

In a real experiment chirp cooled atoms are loaded into the magneto-optical trap (MOT), where three pairs of counterpropagating laser beams subsequently trap them. In our experiment, with the feedback loop shown in Fig. 3 closed, we typically achieve a stable trap with approximately ten million atoms. As the feedback loop is opened, the trap get weaker and finally disappears, illustrating the potential importance of using laser stabilization during chirp cooling.

In conclusion, we have presented a technique and its implementation to stabilize the chirping frequency of a diode laser. The technique is simple and robust, requiring only simple electronics. Further, this technique allows stabilizing the chirp for several continuous hours. This stabilization process eliminates long term fluctuations and drifts in the number of atoms caught in a magneto-optic trap, for example.

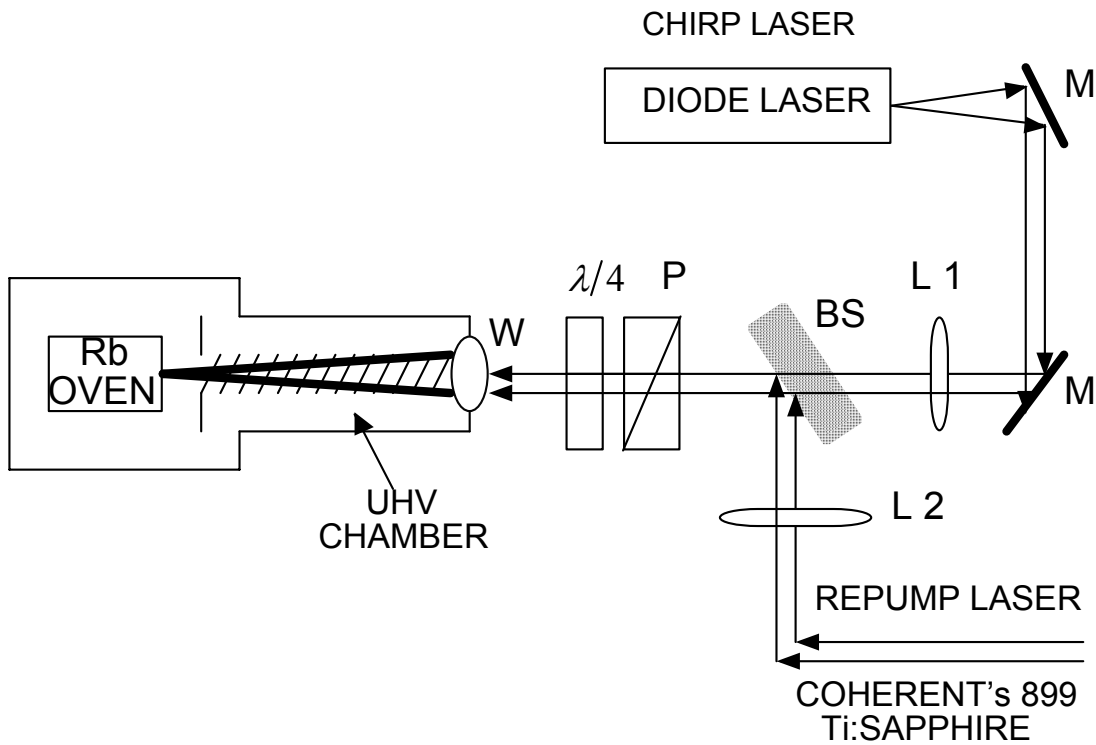


Fig. 1: Shows the experimental apparatus employed for the chirp cooling. UHV: Ultra high vacuum, $\lambda/4$: Quarter wave plate, P: Polarizer, BS: Beam splitter, L1, L2 Lenses, M: turning mirror.

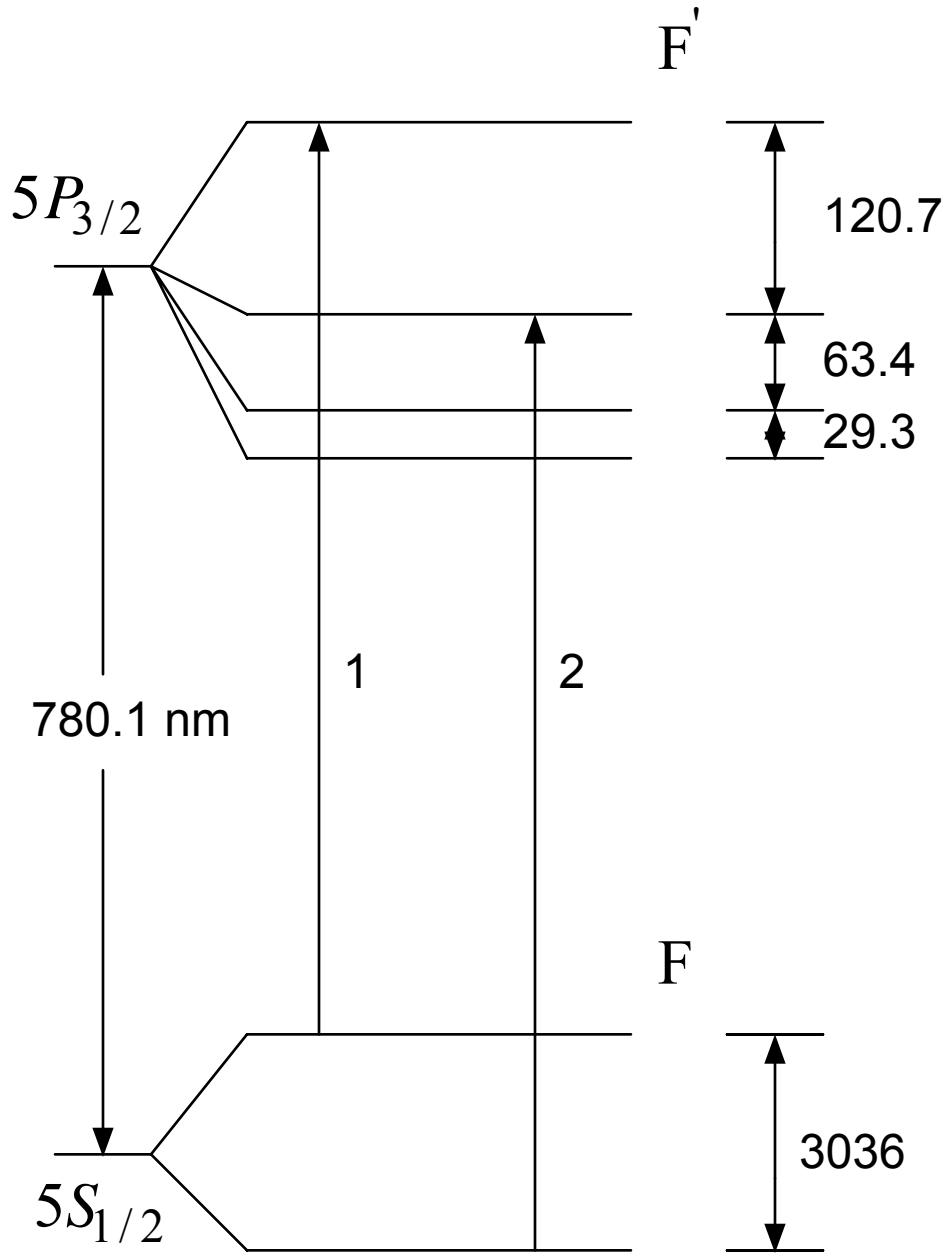


Fig. 2: Energy level splitting of Rb^{85} . Chirp and repump lasers are tuned to the transitions with label 1 and 2 respectively.

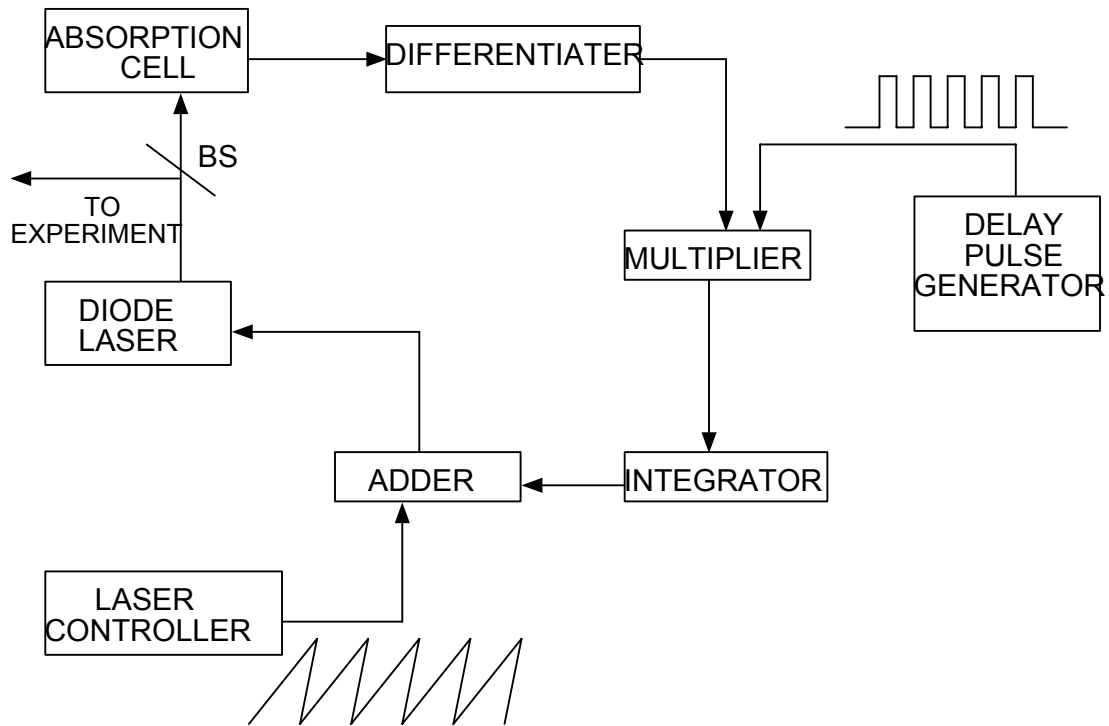


Fig. 3: Block diagram of the electronic circuit used to stabilize the chirp laser.

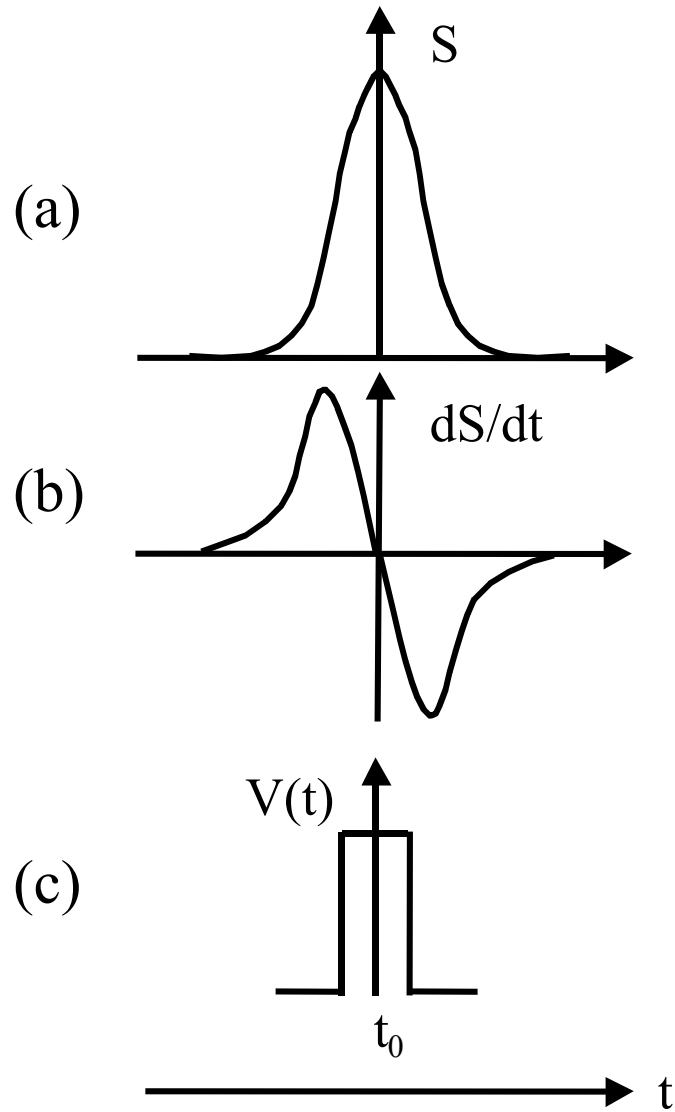


Fig. 4: (a) Absorption signal (b) differentiated signal (c) pulse from pulse generator. In this figure t_0 is the zero crossing point of the differentiated signal.

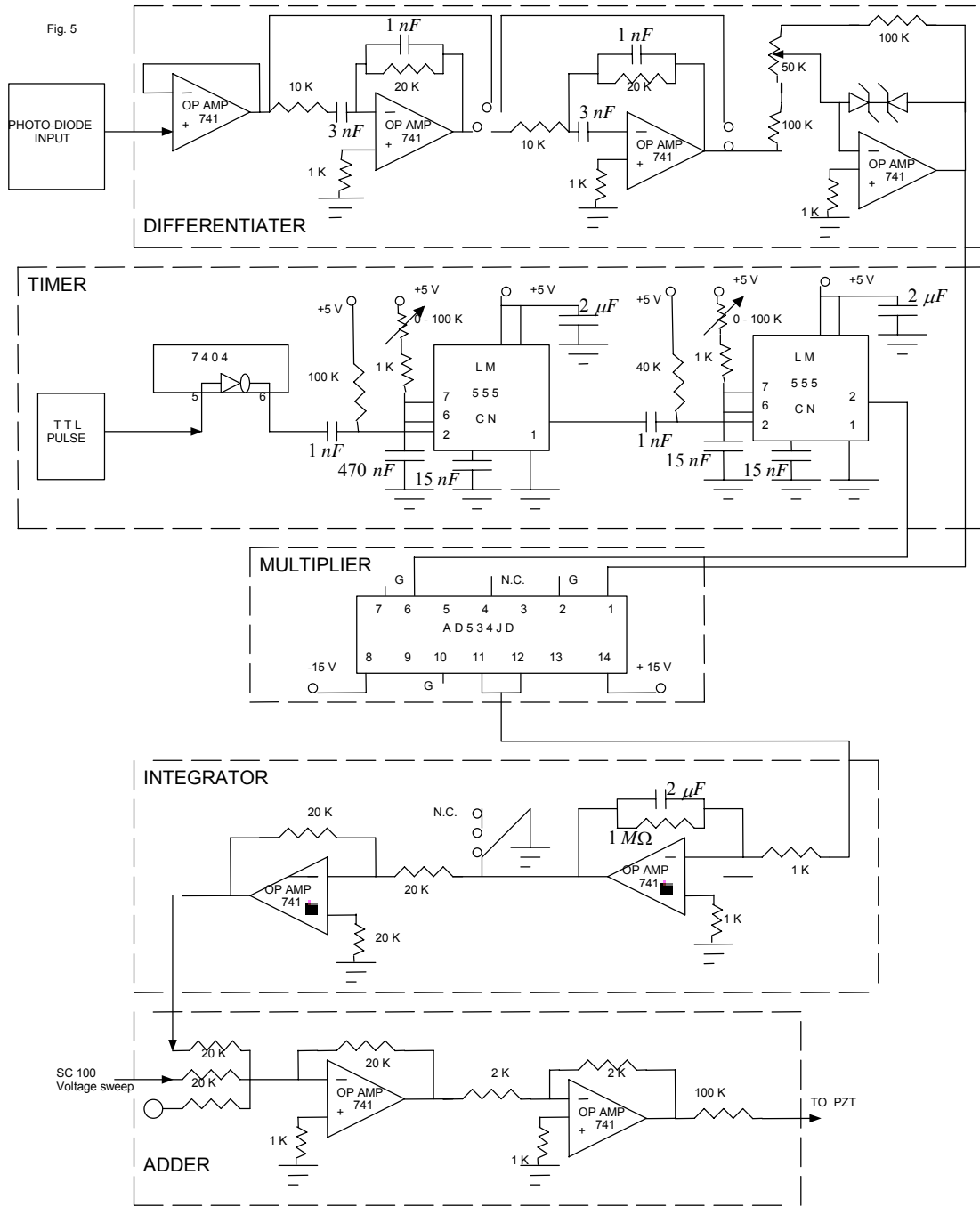


Fig. 5: Schematic of the electronic circuit.

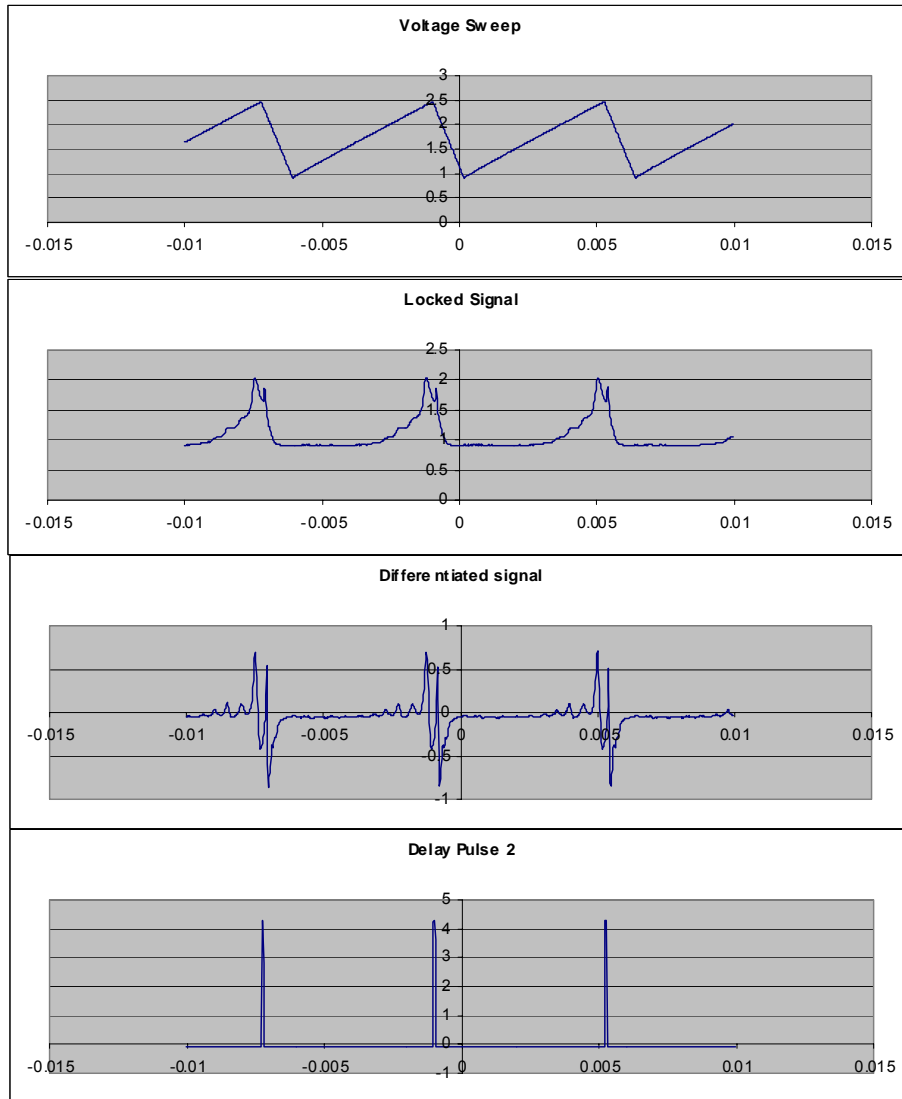


Fig. 6: (a) Voltage sweep (b) absorption signal (c) differentiated signal (d) pulse from pulse generator.

References:

- [1] Harold J. Metcalf, Peter van der Straten, "Laser Cooling and Trapping", Springer, 1999.
- [2] J. Prodan, A. Migdall, W. D. Phillips, I. So, H. Metcalf, and J. Dalibard, "Stopping atoms with laser light", *Phys. Rev. Letts.* **54** 992 (1985).
- [3] W. Ertmer, R. Blatt, J. L. Hall, and M. Zhu, "Laser manipulation of atomic beam velocities", *Phys. Rev. Lett.* **54**, 996 (1985).
- [4] R. N. Watts, C. E. Wieman, "Manipulating atomic velocities using diode lasers", *Opt. Letts.* **11** 291 (1986).
- [5] C. C. Bradley, J. G. Story, J. J. Tollett, J. Chen, N. W. M. Ritchie, and R. G. Hulet, "Laser cooling of lithium using relay chirp cooling", *Opt. Lett.* **17**, 349 (1992).
- [6] V. I. Balykin, V. S. Letokhov, and V. I. Mushin, *JETP Lett.* **29**. 560 (1979).
- [7] C. E. Wieman, L. Hollberg, "Using diode lasers for atomic physics", *Rev. Sci. Instrum.* **62** (1991) 1- 20.
- [8] L. Ricci, M. Weidemuller, T. Esslinger, A. Hemmerich, C. Zimmermann, V. vuletic, W. Konig, T.W. Hansch, "A compact grating-stabilized diode laser system for atomic physics", *Opt. Commun.* **117** (1995) 541-549.
- [9] Parminder S. Bhatia, George R. Welch, and M. O. Scully, "A single mode semiconductor diode laser operating in strong feedback regime and tunable within the D_1 line of Cs atom", *Opt. Commu.* **189** (2001) 321-336.
- [10] M. de Labachellerie and P. Cerez, "Frequency locking of a 850 nm external-cavity semiconductor laser on a Doppler free Cs-D2 line, " *Proc. SPIE* **701**, 182-184 (1986).
- [11] T.P. Dinneen, C.D. Wallace and P.L. Gould, "Narrow linewidth, highly stable, tunable diode laser system", *Opt. Commun.* **92** (1992) 277-282.
- [12] M. de Labachellerie, C. Latrasse, K. Diomande, P. Kemssu, and P. Cerez, "A $1.5 \mu m$ absolutely stabilized external cavity semiconductor laser", *IEEE Trans. Instr. Meas.* **40**, 185-190(1991).
- [13] Y. Millerioux, D. Touahi, L. Hilico, A. Clairon, R. Felder, F. Biraben, and B. de Beauvoir, "Towards an accurate frequency standard at 780 nm using a laser diode stabilized on a hyperfine component of Doppler free two photon transition in Rubidium", *Opt. Commun.* **108**, 91-96 (1994).
- [14] C. D. Wallace, "Measurement of trap loss rate coefficients and trap characteristics of Rubidium magneto-optical trap", Ph. D. thesis, (University of Connecticut 1994).

8. Super-Parallel Holographic Optical Correlator for $N^{1/2}$ Speed-Up Data-Base Search Classically: Experimental Demonstration:

In many situations, it is necessary to identify a target rapidly. For DOD scenarios, a target is typically detected using a synthetic aperture radar. This image is then compared with images stored in a data base, in order to ascertain the identity of the object in question. There are many techniques for performing this task. One technique employs digital signal processing (DSP), wherein a fast digital, a DSP chip, or a dedicated electronic circuit is used to compare the images bit-by-bit serially, thereby identifying the image with the highest degree of correlation to the target image.

An important alternative to this approach is a holographic optical correlator (HOC), which takes advantage of the inherent parallelism of optics. Specifically, the images comprising the data base are stored in a hologram, via angular multiplexing. Using a spatial light modulator, the target image is transferred to an optical beam, which in turn illuminates the hologram, while scanning its angle of incidence. If a match is found, a bright plane wave beam is produced in a pre-specified direction, thereby identifying the target. HOC's are employed for many optical signal processing applications, including pattern and character recognition, implementation of optical interconnections in hybrid optoelectronic parallel computers, in computer/robotic vision, and in artificial neural network technologies.

HOC's can perform correlations nearly 3 orders of magnitude faster than typical DSP-based correlators. This speed-up results from the fact that in the HOC the bits are compared simultaneously (in parallel). However, the HOC is limited in terms of the number of images that can be queried at one time. Specifically, the maximum number of images that can be stored in a single spot via angular multiplexing is typically limited to a few thousands. In principle, this problem can be overcome by spatial multiplexing, whereby different sets of images are stored in different spatial locations. Using a large holographic substrate, it may be possible to employ more than one thousand different spatial locations. The disadvantage of this approach is that the substrate has to be moved around in order to provide access to the different location, thereby slowing down the effective speed of correlation significantly.

Here, we show a novel architecture that overcomes this problem. Specifically, we employ a design wherein the input image is first split into many components, each corresponding to one of the spatial locations of the holographic memory unit (HMU). This is achieved by using a high efficiency holographic demultiplexer (which we have already demonstrated, producing a 5X4 array of identical images). The correlation thus takes place simultaneously at each spatial location. A series of special optical elements are then used to decipher the resulting diffraction patterns. The net result is that the images in all the locations are queried, and a potential image match is achieved in the same amount of time it takes for the conventional HOC to query the images at one location. This super-parallel holographic optical correlator (SPHOC) exhibits a parallelism above and beyond the conventional parallelism of optics. In a typical implementation, the SPHOC outperforms an HOC by more than three orders of magnitude. As such, the SPHOC has an effective speed that is more than a million times faster than a DSP based correlator. *Note that this process can search through an unsorted data base of N items in $N^{1/2}$ steps, without using quantum effects.*

In order to take advantage of this potential speed of the SPHOC, it is necessary to have a holographic memory unit (HMU) that can store many spatial locations, with a large number of images at each location, and each image having a high bit density. The number of spatial locations is determined by the area of the substrate, the number of images that can be stored in a single location is determined by its thickness and the depth of index modulation, and the bit density per image is limited by the array size of

the SLM. The highest bit density achievable using state-of-the-art SLM technology is 1024X1024. The number of spatial locations achievable is typically of the order of 10^3 . The limitation of the conventional materials used for holographic memory is in the number of images that can be stored at a single location, due to a combination of two factors. First, due to potential shrinkage during post-exposure development, the thickness is typically limited to a few hundred μm . Second, the depth of index modulation is generally low. More quantitatively, this depth is characterized by the so-called $M_{\#}$, which corresponds to the maximum number of 100% efficiency hologram that can be written in a single location. The efficiency of each of N weak holograms written in a single location is then given by $(M_{\#}/N)^2$. Typical materials have an $M_{\#}$ of the order of unity. Given that a certain minimum diffraction efficiency (e.g. 10^{-6}) is required for a given signal-to-noise ratio threshold for detection, the value of N is limited to about 10^3 . The total amount of information that can potentially be stored in a conventional holographic disc is thus about 100 Gbyte.

We use a new material, Memplex™, to develop a holographic memory unit with a storage capacity of 1 Terabyte. Developed by the Laser Photonics Technology, Inc., of Amherst, NY, this material is made available to one of our team members, the Hybrid Technologies, LLC, of Amherst, NY. When the SPHOC is implemented with this HMU, in a realistic configuration, the system will be capable of searching through 1 Terabyte of image data in 1 msec. With each image encoded in 1024X1024 bits, this will correspond to searching through ten million high-resolution images in one millisecond, a feat unthinkable using any existing technology.

In a battle zone, it is crucial to be able to identify enemy vehicles, such as tanks, planes, and helicopters, very rapidly. This is often done by using optical or electronic correlators, as mentioned above. However, the correlators are generally not rotation nor scale invariant, making the identification difficult. This problem can be alleviated by storing multiple pictures of the same vehicle, covering many orientations and sizes. The large number of images accessible at a high speed using our proposed approach will make this goal a reality.

Of course, in recent years, mathematical tools have been developed to perform orientation invariant target recognition using (a) the so-called object to image mapping, (b) an invariant representation of the map, and (c) correlating the map with a relatively smaller data base of these maps. Note that the architecture proposed here can be used to speed up enormously this technique as well. Specifically, one would store in the holograms the maps instead of the images, and identify the matching map very fast (10 million in a millisecond). Such a speedup would make the task of tracking a missile a much easier one. In the law enforcement and homeland defense arena, this technique can be used to speed up the identification of potential law-breakers and terrorists, by augmenting the successful but relatively slow technique developed by Visionics, Inc. In this approach, a picture of a person is taken, from which a small set of features are extracted --- corresponding to the mapping data mentioned above. Typically, it takes about a minute to search through the corresponding data bank of features for any potential match (i.e., correlation). This searching step would speed up by at least three orders of magnitude if one employs the SPHOC technique proposed here.

The specific device to be developed is a super-parallel holographic optical correlator, which will, in its full-fledged version, search in 1 msec through ten million images, each with a resolution of 1024X1024 bits, employing a holographic memory disc with a storage capacity of 1 Terabyte. We anticipate to commercialize this technology for automatic target recognition systems critical to the DOD mission, to homeland defense, as well as for civilian application such as robotic vision.

SUMMARY OF THE PROPOSED ARCHITECTURE:

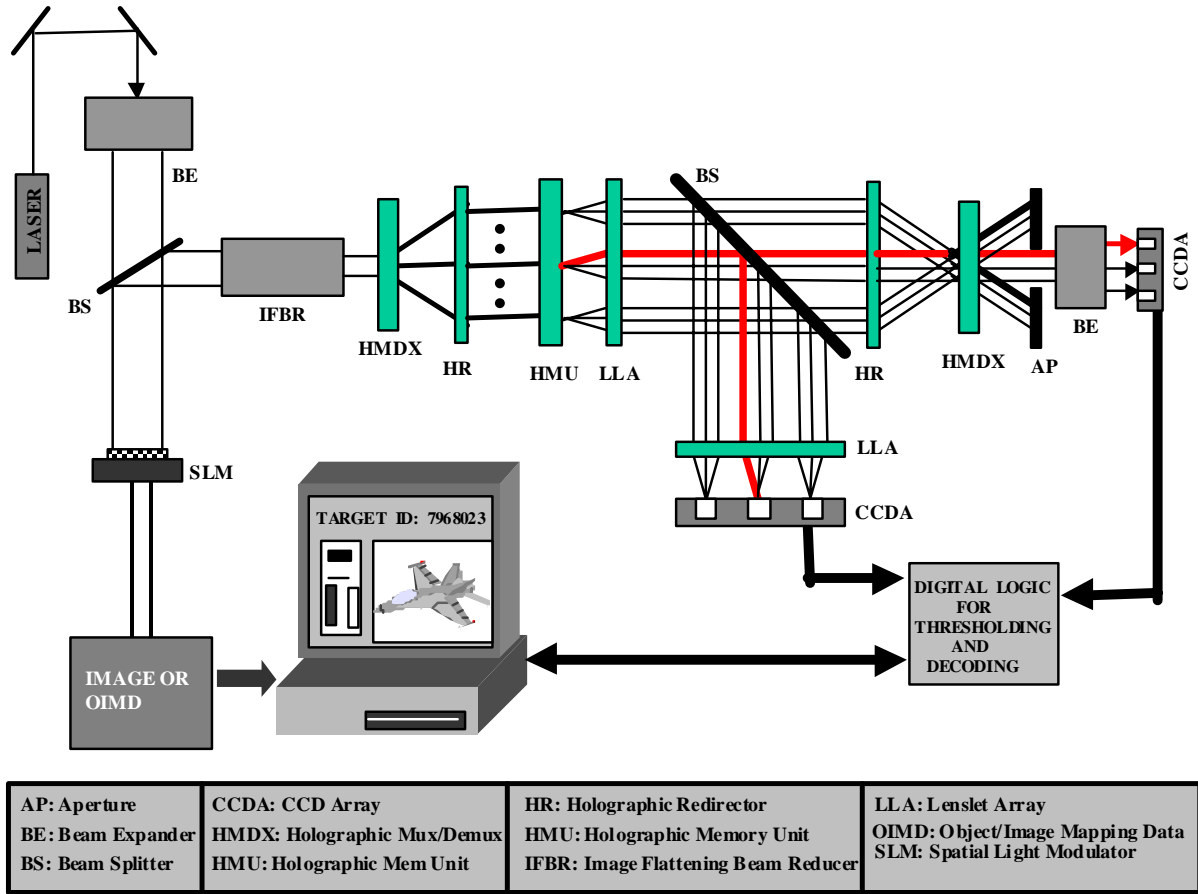


Figure 1: Schematic illustration of the Super Parallel Holographic Optical Correlator, SPHOC, which realizes a single-query process for searching through all the images stored in all the spatially distinct locations simultaneously. The abbreviations are defined on the bottom of the diagram. While the diagram is one dimensional, the process is two-dimensional. For practical numbers, one can use this architecture to search through a million images, each with a 1024 bit X 1024 bit resolution, in less than a msec. The details of the architecture are discussed in the text.

The SPHOC architecture is shown schematically in figure 1. Here, $r \times s$ number of images are stored in each spot of the HMU via two-dimensional angular multiplexing. The process starts by expanding the collimated beam from a 20 mW solid-state green laser, for example, in order to match the size of the SLM. The target image is gathered, for example, by a camera or an SAR (synthetic aperture radar) in a battle theatre. (Alternatively, the target could represent an object-to-image data map, which requires a much smaller amount of information to represent the image, in a rotation invariant way). A copy of the image is sent to the control computer for recording, and another copy is sent directly to the SLM via a high-speed data bus. The beam reflected from the face of the SLM carries this image. This reflected beam is now passed through the IFBR (Image Flattening Beam Reducer), which is simply a set of two lenses. It reduces the image size by the ratio of the focal lengths of the two lenses, and projects a very slowly diverging version of the SLM image at the face of the next element: the HMDX (Holographic Demultiplexer/Multiplexer). The HMDX is a device that produces $n \times m$ copies (which is the number of spatial locations on the

HMU) of the input image, in as many angular directions. Such a device can be constructed simply by writing $n \times m$ plain wave holograms over the entire volume.

The output beams from the HDMX are now passed through an element termed the HR: the Holographic Redirector. This role of this device is to redirect the output beam from the HDMX into $n \times m$ images propagating parallel to the axis. The $n \times m$ identical copies of flattened images now impinge on the HMU, one at each spatial location. If the image matches one in one of these locations, a correlation diffracted beam will emanate from that location in a particular angle. Here, we show all such diffraction beams (in one dimension, for simplicity of drawing), keeping in mind that only one of these beams (shown by the red/bold line) will be produced for a given image. The goal of the rest of the architecture is to identify (a) which spatial location the beam belongs to, and (b) within that location, what angle does the beam correspond to. These two pieces of information will identify uniquely which image we have matched.

The beams coming out of the HMU is now sent through the LLA (Lenslet Array). The task of this array is to collimate the direction of all the spots to be parallel to the axis. Such a lens array can be made by writing holograms where the object beam is a plane wave, and the reference beam is a converging wave, at each of the $n \times m$ separate spatial locations. Alternatively, one can use a commercial lenslet array for this purpose.

The beams are now split into two components by a beam splitter. One component goes through another LLA, thus getting refocused, onto an $n \times m$ array of CCD elements (CCDA). Identifying the detector that sees the highest signal yield the information about which spatial location the matching-image is in. The other part of the beam goes through another HR (Holographic Redirector). The HR simply redirects all the incident beams to a central point, without focusing the beams coming from the same spot with respect to one another, as shown.

These beams are now passed through another HDMX, which is identical to the one used at the input, but now operating in reverse. However, the reverse operation has the potential problem (as illustrated later) that additional beam patterns (weaker than the one generated along the axis) will also be produced. A simple aperture can be used to eliminate these unwanted spots. After the filter, we use a beam expander to match the size of the second CCD array, which contains $r \times s$ number of elements, corresponding to the number of angles used in the two-dimensional angular multiplexing during the writing stage. The element of the CCD that sees the brightest signal yields the information about the angle of the matched image. Data gathered from the detector array and the CCD array, properly thresholded, can be sent through a digital logic circuit to yield the absolute identity of the image we have matched. For practical parameters mentioned above, the whole process will take less than a msec.

DETAILS OF THE ELEMENTS EMPLOYED IN THE ARCHITECTURE:

The Beam Expander (BE) is illustrated in figure 2. It is simply a pair of lenses set up as a telescope.

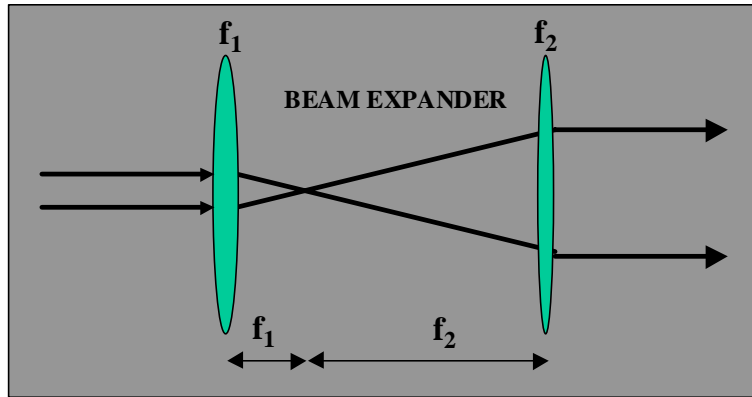


Figure 2: Schematic illustration of the beam expander, which is simply a telescope.

The Image Flattening Beam Reducer (IFBR) is again a simple combination lenses, arranged in a way so that the image at the input (which would be the SLM) would be reproduced in a reduced size at the output (which should be the location of the HMU), ensuring that this size matches the active area of each of the HMU subunits. The IFBR is illustrated in figure 3.

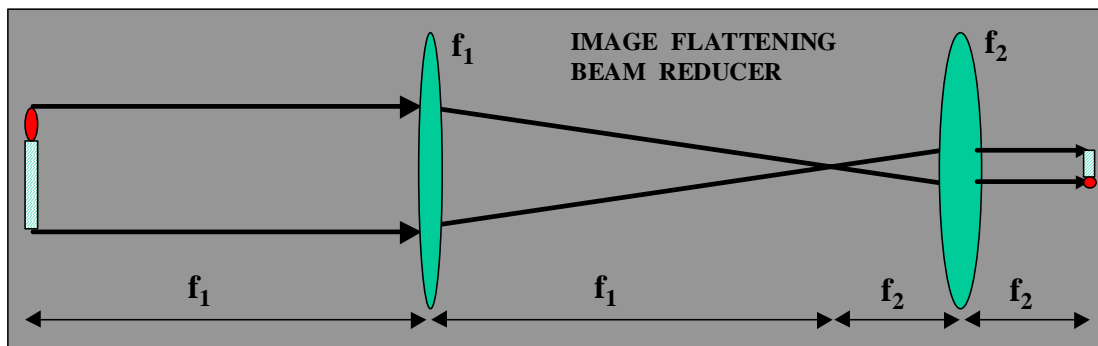


Figure 3: Schematic illustration of the image flattening beam reducer.

The Holographic Multiplexer/Demultiplexer (HMDX) is a cornerstone of this architecture. It is produced by writing angle multiplexed gratings in a thick hologram. The basic features of the HMDX is illustrated in figure 4.

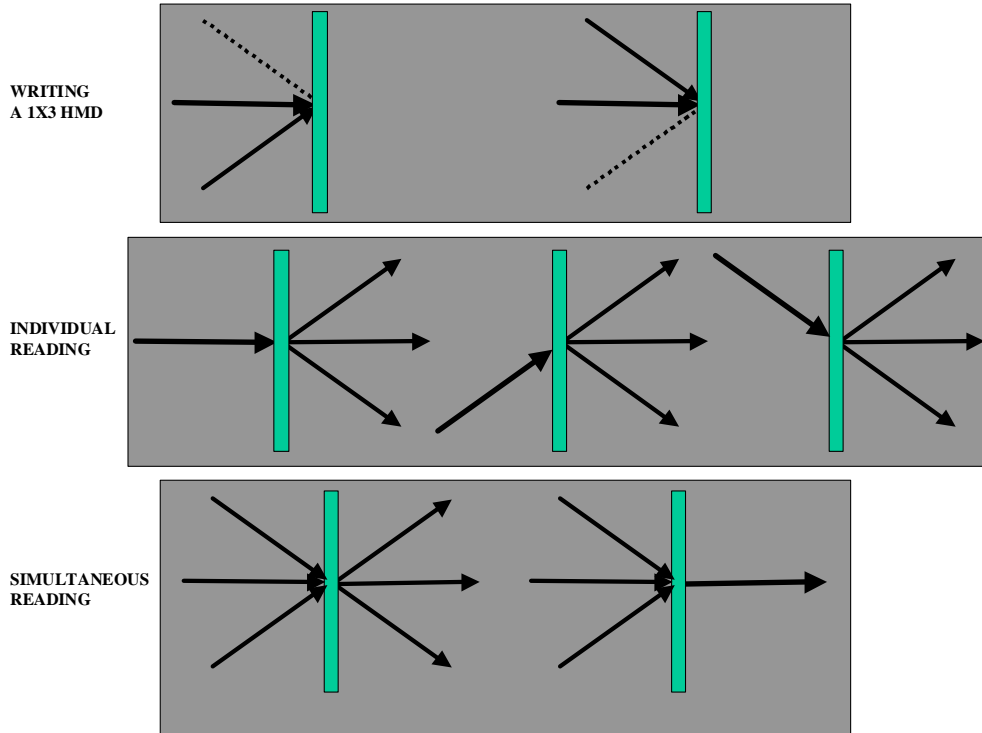


Figure 3: Schematic illustration of the HMDX. Top: the writing process starts by using an object beam and a reference beam. The object beam is kept unchanged and a new direction for the reference beam is chosen, to write the second grating. The process is repeated $(K-1)$ times for a $1XK$ HMDX ($K=3$ here). Note that the transmission is also as useful as any of the diffraction beams, provided the diffraction efficiencies are each equalized to the undiffracted beam. Middle: When readout by individual input beams, K output beams are produced. Bottom: when the HMDX is readout by K beams simultaneously, K output beams generally result. Only when the phase of the input beams are locked actively, and the ratios are balanced a single output beam would be produced. The front end of the SPHOC (fig.1) uses the middle-left functionality, while the back end of the SPHOC uses the bottom-left functionality.

The Holographic Redirector (HR) is a device that has a single, slanted grating at each of rXs locations, when used after an HMDX that produces sXs output beams. At each location, a single hologram is written, with the object beam parallel to the axis, and the reference beam angle chosen to match the angle of the beam that would impinge on that spot during its use in the SPHOC architecture. Figure 5 shows the writing process and the readout geometry for the HR.

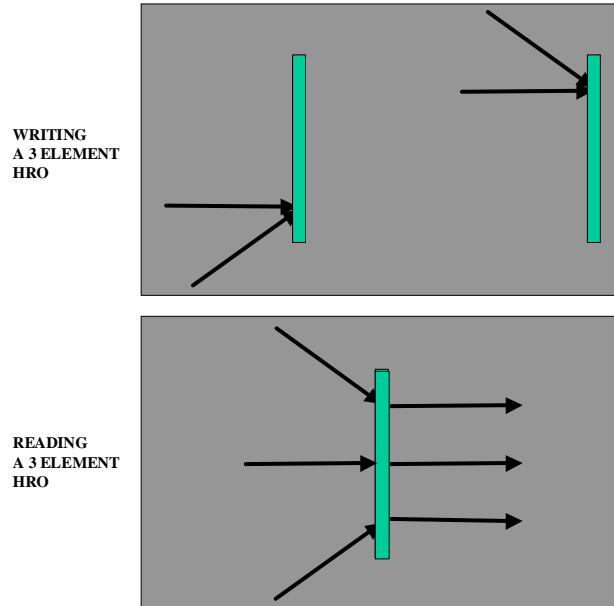


Figure 5. Schematic illustration of the writing (top) and readout of the holographic redirector, HR.

The Holographic Memory Unit (HMU) is the image storage device. The basic HMU structure is illustrated in figure 6. Briefly, rxs sub-areas on this substrate are each used as a local storage unit, inside which $n \times m$ image pages are stored via angular multiplexing. Figure 7 illustrates the angular multiplexing geometry to be employed.

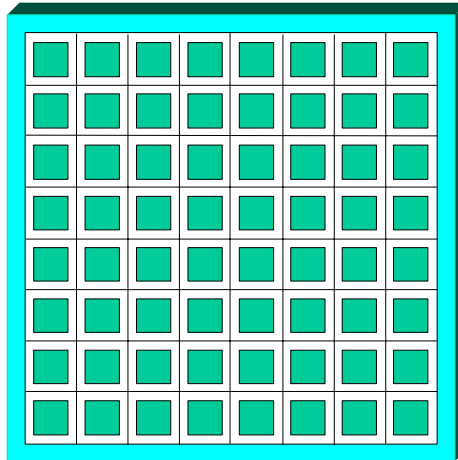


Figure 6: Schematic illustration of the Holographic Memory Unit, with a dimension of 124mm X 124mm X 2mm. The number of sub-units is 1600, although only 64 are shown for clarity. Each sub-unit has a dimension of 2mm X 2mm, and separated from one another by a 1 mm wide guard strip in all directions.

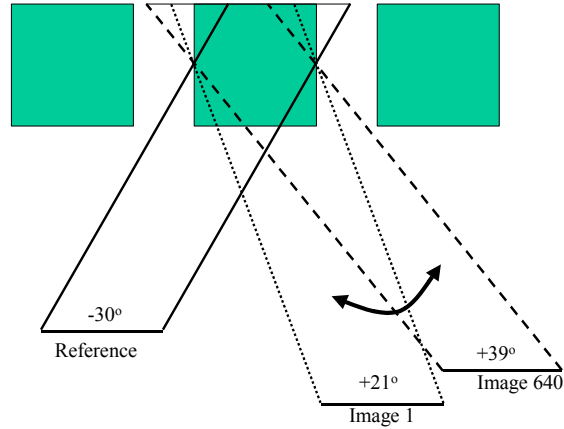


Figure 7: Schematic illustration of the angular multiplexing geometry, drawn to scale. The reference and image beams are incident on the HMU from the front. The reference beam is held fixed at -30° , while the image beam is scanned from $+21^\circ$ to $+39^\circ$, in increments of 0.5 mrad. Note that the 1 mm wide guard band is wide enough to eliminate potential cross-talks between neighboring sub-units.

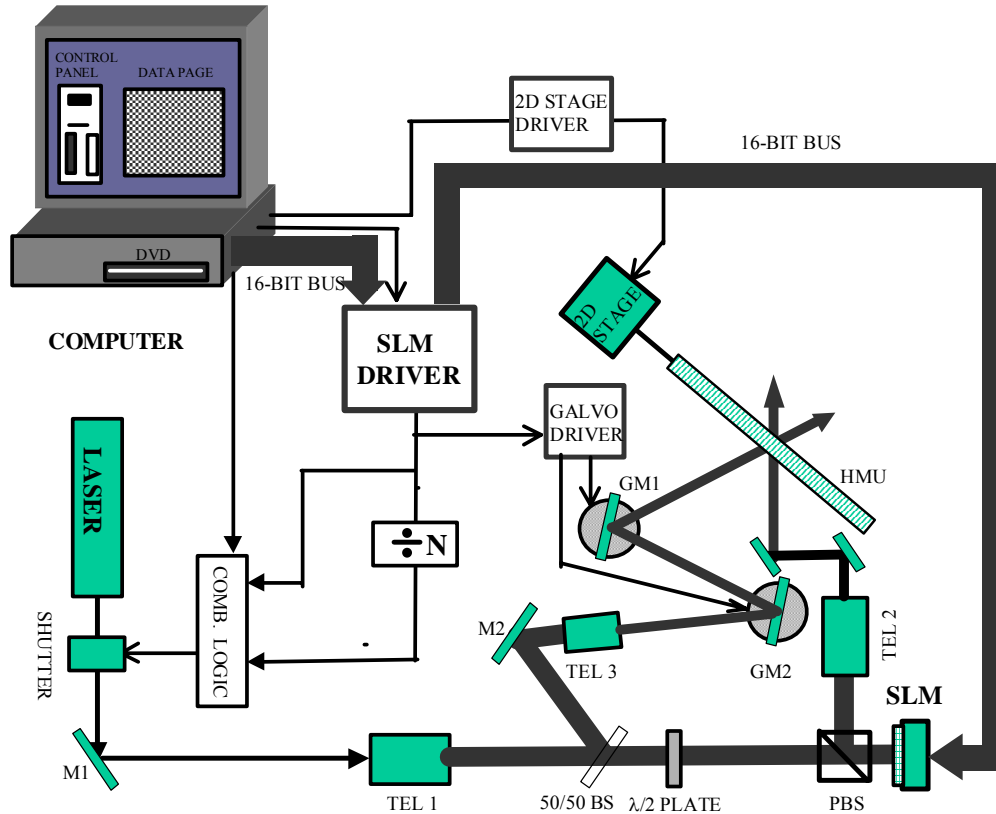


Figure 8. Schematic illustration of the writing set up. See text for details.

In order take advantage of this potential speed of the SPHOC, it is necessary to have a holographic memory unit (HMU) that can store many spatial locations, with a large number of images at each location, and each image having a high bit density. The number of spatial location is determined by the area of the substrate, the number of images that can be stored in a single location is determined by its thickness and the depth of index modulation, and the bit density per image is limited by the array size of the SLM. The highest bit density achievable using state-of-

the-art SLM technology is 1024X1024. The number of spatial locations achievable is typically of the order of 10^3 . The limitation of the conventional materials used for holographic memory is in the number of images that can be stored at a single location, due to a combination of two factors. First, due to potential shrinkage during post-exposure development, the thickness is typically limited to a few hundred μm . Second, the depth of index modulation is generally low. More quantitatively, this depth is characterized by the so-called $M_{\#}$, which corresponds to the maximum number of 100% efficiency hologram that can be written in a single location. The efficiency of each of N weak holograms written in a single location is then given by $(M_{\#}/N)^2$. Typical materials have an $M_{\#}$ of the order of unity. Given that a certain minimum diffraction efficiency (e.g. 10^{-6}) is required for a given signal-to-noise ratio threshold for detection, the value of N is limited to about 10^3 . The total amount of information that can potentially be stored in a conventional holographic disc is thus about 100 Gbyte.

Our eventual goal, realizable with the Memplex™ material, is to achieve 40X40 spatial locations, and 1000X8 images (at as many angles) at each location, with 1024X1024 bits in each image. However, given that the primary focus here is to demonstrate the feasibility of the SPHOC architecture, we limit ourselves to 5X5 spatial locations and 128X4 images (at as many angles), with 256X256 bits in each image. A bank of synthetic aperture radar (SAR) images of DOD-relevant objects, such as planes and tanks at varying distances and orientations, will be used as the source. The images are available on the web. However, we have to remap the images to the low resolution of 256X256 bits, using a commercially available software (we have already done such remapping previously). The remapped images will be stored in a computer, and then loaded into a 256X256 bit SLM. The object beam will be produced by reflecting a plane wave from a single mode Argon-ion laser. The reference beam will simply be a plane wave. The object and reference beams will intersect at one of the spatial locations in a 2mm thick Memplex™ substrate, thus storing the image. Galvo-mounted mirrors, scanned synchronously with the SLM image loading, will be used to perform angular multiplexing. An X-Y stage will be used to move to a different spatial location on the SLM, in order to perform spatial multiplexing. Each spatial location will use an area of 3mmX3mm, with a gap of 1 mm on all sides. The substrate dimension will thus be 2cmX2cmX2mm.

The optical set-up is relatively simple, as shown in figure 8. A beam from the Ar laser at 532 nm (doubled YAG) is first sent through a spatial filter (not shown), collimated, and expanded (TEL1) to a 2 cm diameter. The beam then passes through a 50/50 beam splitter, producing the object and reference beams. The object beam is passed through a $\lambda/2$ waveplate in order to rotate its polarization by 90° . It then goes through a polarizing beam-splitter (PBS), and reflects off the face of the SLM, which is covered by a $\lambda/4$ waveplate. For the "ON=1" elements, the polarization is rotated by 90° degrees upon reflection, while for the "OFF=0" elements, the polarization is unchanged. As such, the beam reflected by the PBS corresponds to the checkerboard-type pattern sent to the SLM. The resulting image is then transferred to the HMU through a two-lens, 4f imaging system (TEL3). Since the dimensions of the SLM are about twice as large as the HMU memory sub, TEL3 is designed to reduce the image size correspondingly. Note that no aperture is necessary, since the SLM surface area in effect acts as the aperture.

The reference beam is first masked by a mask matching the exact dimensions of the SLM surface, reduced in size, and 4f-imaged on to the HMU unit (TEL2). On its way to the HMU, the reference beam is reflected off two galvo-mounted thin mirrors. The relative positions of the galvo mirrors and the HMU are chosen carefully in order to eliminate any spatial shift resulting from angular scanning. Briefly, the galvo stages are rotated such that when GM1 is turned by $-\theta$, GM2 is turned by 2θ , producing a net reference angle rotation of θ . Furthermore, GM2 is equidistant from GM1 and the HMU. Under this condition, the positional shift is eliminated to first order; any residual shift is minimized by making the sides of the triangle as small as possible. Our experience from using this approach previously shows that the remaining effect is inconsequential.

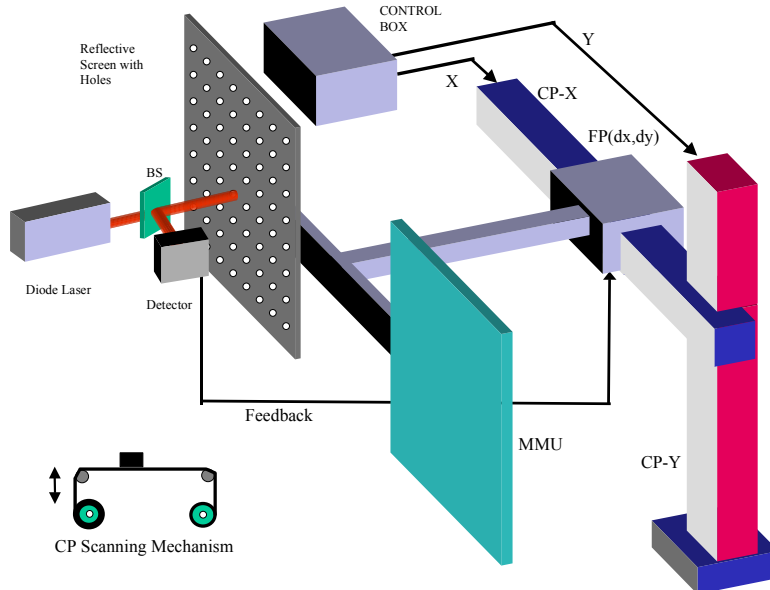


Figure 9. Schematic Illustration of the 2D scanning mechanism. See text for details.

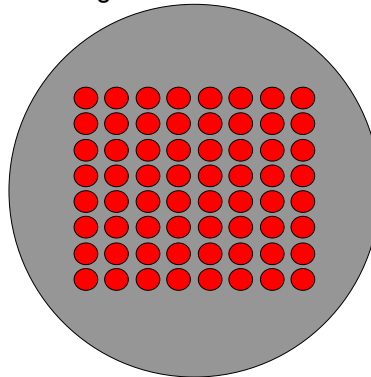


Figure 10. Schematic Illustration of an 8x8 lenslet array, housed in a circular substrate.

The 2D scanning stage is in figure 9. The assembly will consist of two different positioners. The HMU would be secured to the fine positioner (FP), and the FP would be secured to a coarse positioner (CP). Assume first that the CP has moved the sample to within 0.5 mm in both X and Y directions. The FP is then used to position the HMU precisely. This is accomplished by using a feedback system. A diode laser is mounted at a position that remains fixed with respect to the writing apparatus. A screen, fastened to the FP, and parallel to the HMU, moves around in front of the diode laser as the FP moves the HMU. The surface of this screen (e.g. metal coated plastic) reflects the light back, which in turn is redirected to a photo-detector. This surface has a number of holes, equaling the number of HMU sub-units, and separated from each other by the same distance as the HMU sub-units. The hole diameter is about 0.5 mm, while the laser beam diameter is about 1 mm. As such, the laser beam is aligned perfectly with the hole when the detector signal is minimized. A simple servo is used to guide the FP, first in the X direction, and then in the Y direction until this position is reached. Note that the HMU and the reference screen are mounted on a single bar, which in turn is connected to the FP. After the data has been stored, the HMU and the reference screen has to stay fastened to this bar at all times; otherwise, a painstaking (but not impossible) procedure has to followed to re-establish the one to one correspondence between the HMU sub-units and the holes in the reference screen.

The Lenslet Array (LLA) is a commercially available device that houses many small diameter lenses in a two-dimensional array. A typical LLA is illustrated in figure 10.

EXPERIMENTAL DEMONSTRATION OF THE BASIC FUNCTIONS:

We have recently demonstrated some of the key components and functionalities of the SPHOC architecture shown in figure 1. To start with, figure 11 shows two different HMDX. The top-left one is a 1X20 HMDX, which produces a one dimensional array of 20 output beams when put in front of a single input beam. The bottom-left figure shows a 5X5 HMDX, which produces a two-dimensional array of 25 output beams when put in front of a single input beam. In the data shown here, the input beam actually contains an image after passing through an Air Force resolution chart. When the output is re-imaged at the flat point, the image is clearly reproduced in multiple copies (inset). This is the key functionality that makes the SPHOC feasible. The right side shows the actual device (a plastic type square substrate made from the Memplex material) that produces the 5x5 array.

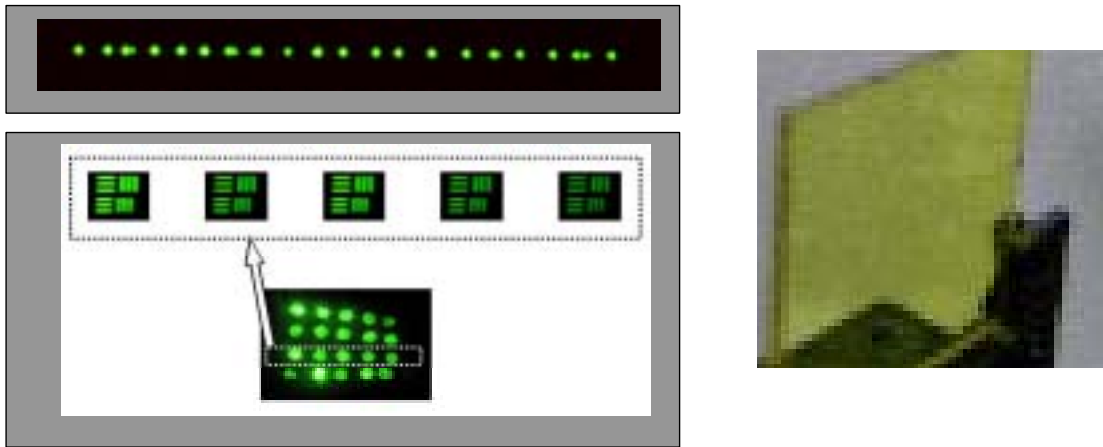


Figure 11. Demonstration of HMDX using the Memplex material. See text above for details.

Given this evidence, we proceeded to demonstrate a rudimentary version of the SPHOC shown in figure 1. To keep things simple, while not compromising on the basic issues, we used a one-dimensional angular multiplexing as well as a one dimensional spatial mutiplexing. Specifically, three spatial positions displaced from each other horizontally were used on an HMDX, each containing 8 images each, multiplexed in the horizontal angle. A simplified version of the writing set-up of figure 8 was used to do the recording. A set of these images, raed out from one of the three locations, and imaged onto a card, and then photographed with a camera, is shown in figure 12. The relatively poor quality of the images is due to (a) the low SLM resolution (256X256 bits) and imperfections in the optics. However, such a quality is generally good enough for image identification purposes. Next, we made a 1X3 one dimensional HMDX, which performed similar to the ones shown in figure 11, along with an HR with three locations. We also purchased an off-the-shelf LLA from MEMS Optical Inc., of Huntsville. Part of a sample image of the LLA is shown in figure 12 (note that the actual arrangement of the lenses is slightly different from the one shown schematically in figure 10.)

Given the small number of images involved, it was not necessary to use the beamsplitter, the HR and the HMDX in the back part of the SPHOC. In addition, instead of using two CCD arrays, we simply used a single video camera (again, this is possible simply because the number of images are so small.

During the correlation operation, we loaded one of the images from the set of 24, and the system was able to identify very easily which one it was, producing a bright and distinct correlation spot at the correct angle and the correct position. When all the images were loaded sequentially into

the SLM, the correlation spots simply moved at the same rate. Figure 13 shows a time-lapse photograph of eight of these correlation spots, corresponding eight images stored at one of the three locations. While this demonstration has been limited in scope, it is certainly very encouraging for the SPHOC.

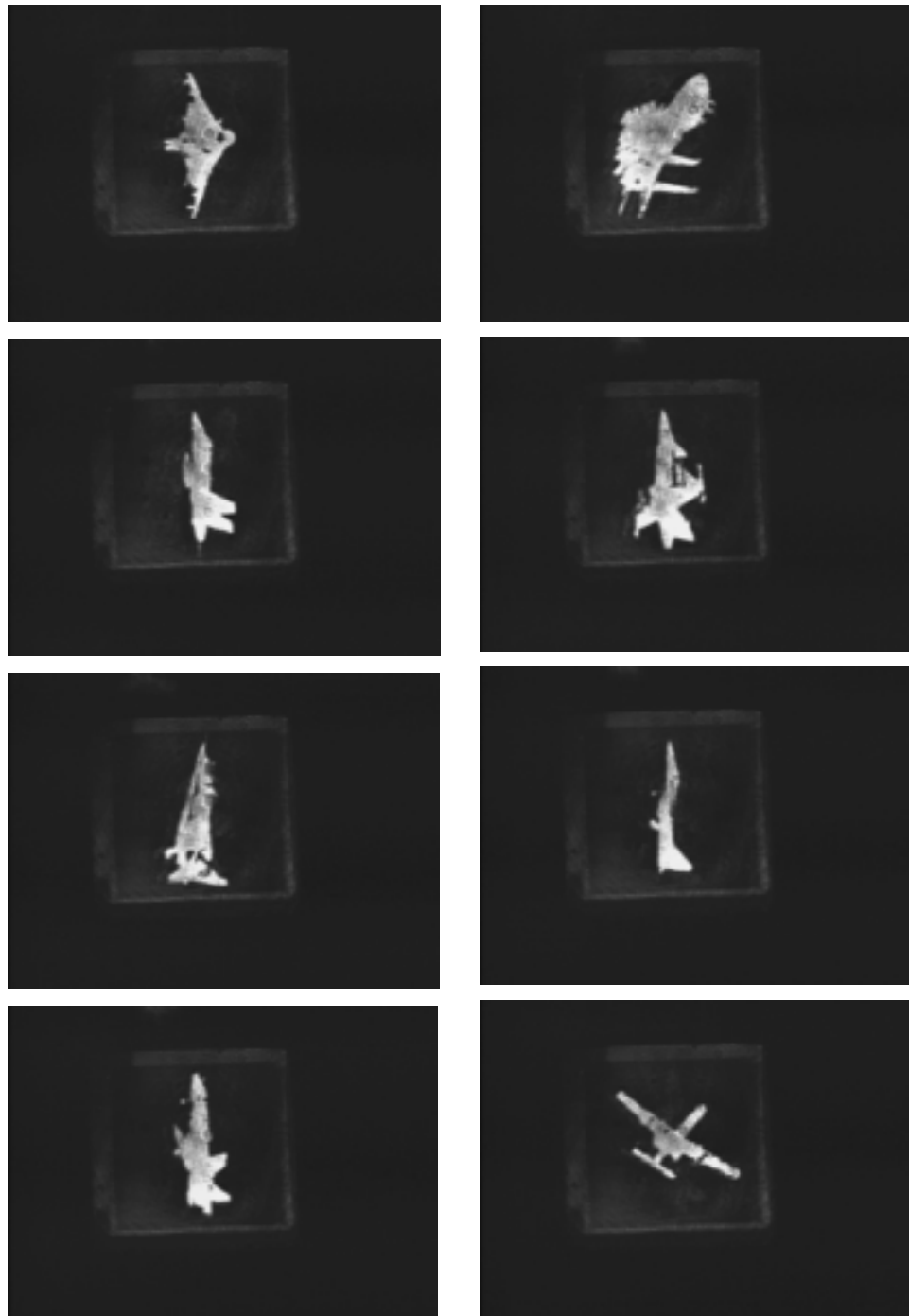


Figure 12. Optically read-out and photographed copies of the eight images of planes in single location of the HMU. See text for details.

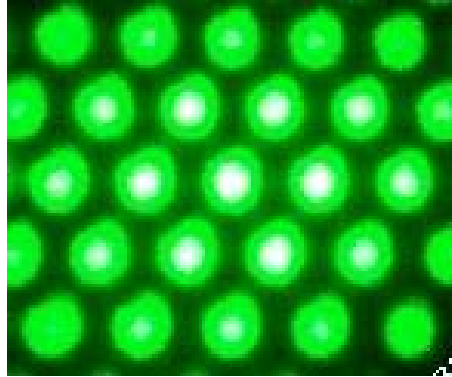


Figure 13. Section of the image formed when a plane wave is passed through the lenslet array we used.



Figure 14. Time-lapsed picture of the sequentially forming eight correlation spots corresponding to eight of the 24 images stored in one of the three locations in the HMU we used. See text for details.

References:

- [1] Harold J. Metcalf, Peter van der Straten, "Laser Cooling and Trapping", Springer, 1999.
- [2] J. Prodan, A. Migdall, W. D. Phillips, I. So, H. Metcalf, and J. Dalibard, "Stopping atoms with laser light", *Phys. Rev. Letts.* **54** 992 (1985).
- [3] W. Ertmer, R. Blatt, J. L. Hall, and M. Zhu, "Laser manipulation of atomic beam velocities", *Phys. Rev. Lett.* **54**, 996 (1985).
- [4] R. N. Watts, C. E. Wieman, "Manipulating atomic velocities using diode lasers", *Opt. Letts.* **11** 291 (1986).
- [5] C. C. Bradley, J. G. Story, J. J. Tollett, J. Chen, N. W. M. Ritchie, and R. G. Hulet, "Laser cooling of lithium using relay chirp cooling", *Opt. Lett.* **17**, 349 (1992).
- [6] V. I. Balykin, V. S. Letokhov, and V. I. Mushin, *JETP Lett.* **29**. 560 (1979).

- [7] C. E. Wieman, L. Hollberg, "Using diode lasers for atomic physics", *Rev. Sci. Instrum.* **62** (1991) 1- 20.
- [8] L. Ricci, M. Weidemuller, T. Esslinger, A. Hemmerich, C. Zimmermann, V. Vuletic, W. Konig, T.W. Hansch, "A compact grating-stabilized diode laser system for atomic physics", *Opt. Commun.* **117** (1995) 541-549.
- [9] Parminder S. Bhatia, George R. Welch, and M. O. Scully, "A single mode semiconductor diode laser operating in strong feedback regime and tunable within the D_1 line of Cs atom", *Opt. Commun.* **189** (2001) 321-336.
- [10] M. de Labachellerie and P. Cerez, "Frequency locking of a 850 nm external-cavity semiconductor laser on a Doppler free Cs-D2 line," *Proc. SPIE* **701**, 182-184 (1986).
- [11] T.P. Dinneen, C.D. Wallace and P.L. Gould, "Narrow linewidth, highly stable, tunable diode laser system", *Opt. Commun.* **92** (1992) 277-282.
- [12] M. de Labachellerie, C. Latrasse, K. Diomande, P. Kemssu, and P. Cerez, "A 1.5 μm absolutely stabilized external cavity semiconductor laser", *IEEE Trans. Instr. Meas.* **40**, 185-190(1991).
- [13] Y. Millerioux, D. Touahi, L. Hilico, A. Clairon, R. Felder, F. Biraben, and B. de Beauvoir, "Towards an accurate frequency standard at 780 nm using a laser diode stabilized on a hyperfine component of Doppler free two photon transition in Rubidium", *Opt. Commun.* **108**, 91-96 (1994).
- [14] C. D. Wallace, "Measurement of trap loss rate coefficients and trap characteristics of Rubidium magneto-optical trap", Ph. D. thesis, (University of Connecticut 1994).